Alma Mater Studiorum · University of Bologna

School of Science
Department of Physics and Astronomy
Master Degree in Physics

The FAMU experiment: characterization of innovative detectors for high precision spectroscopy

Supervisor:
Prof. Giuseppe Baldazzi

Submitted by:
Alessandro Colavecchia

Academic Year 2021/2022

Abstract

The incompatibility between the proton radius values measured in recent years has given rise to what is now called the proton radius puzzle. This discrepancy is nowadays without explanation.

In order to find a solution to the proton radius puzzle a new experiment has been proposed. The aim of this experiment, called FAMU, is to obtain a new and more precise measure of the Zemach radius of the proton, ie the quantity that has the highest uncertainty in high precision spectroscopy.

If this measurement confirmed the results obtained before 2010, the starting date of the puzzle, then the discrepancy would be caused by procedural errors or ignored corrections. Otherwise, the new value would indicate the presence of new physics still unknown.

Introduction

In recent years there has been a series of discrepancies in the measured values of the proton radius. This discrepancy originated from a new measurement methodology that employed muonic hydrogen.

The classic procedure used to measure this quantity was electron-proton scattering: from the cross section describing this process in fact it's possible to extract both the mean squared proton charge radius and its magnetic radius.

This procedure was used predominantly until 2010, and the recommended value for the proton charge radius up to that year was [69]

$$r_p = 0.8775(51)\ fm \tag{1}$$

In 2010 a new procedure was devised in order to measure the proton radius: instead of focusing on electron-proton scattering, this new method proposed to extract the proton radius from the Lamb shift. Since in ordinary hydrogen the contribution of the proton radius is not dominant, it was decided to employ muonic hydrogen instead.

This procedure was used by Pohl *et al.* [75], and the proton charge radius thus obtained was

$$r_p = 0.84184(36)(56)\ fm \tag{2}$$

a value that wass 10 times more precise and 5σ smaller than the world average up until that year. Furthermore, the new value obtained by Pohl *et al.* was also 26 times more precise but 3.1σ smaller than the hydrogen-independent value extracted from the electron-proton scattering data available at the time.

This experiment was repeated during the following years in order to verify this unexpected result, and further studies confirmed the incompatible value reported in Equation 2. This fact gave rise to the so-called proton radius puzzle, which up to this day still doesn't have a solution.

The importance of this discrepancy lies in the fact that it's not predicted by the Standard Model: the proton radius was thought to be a constant, and if this is not the case investigating the matter may lead to new important scientific discoveries.

The aim of the FAMU experiment (**F**isica degli **A**tomi **M**uonici, meaning Physics of Muonic Atoms) is exactly solving once and for all the proton radius puzzle. More precisely, the experiment will focus on the Zemach radius of the proton, a quantity affected by the highest uncertainty in high precision spectroscopy.

If the value measured during the experiment were similar to those obtained before the proton radius puzzle, then the cause of the discrepancy in the proton radius value would consist into procedural errors or neglected high order corrections. Otherwise, it would be proof that this incompatibility indicates a new phenomenon yet to be studied.

The first chapters of this thesis will cover the history of the proton radius puzzle and the theory of ordinary hydrogen and common hydrogen energy levels. The FAMU

experiment, its methodology and its apparatus will be described in Chapter 4 and 5. Lastly, Chapter 6 will describe an innovative detector system devised and built by the Bologna Division of INFN and by the Physics Department of the University of Bologna specifically for this experiment.

Contents

Chapter 1

Determination of the proton radius through elastic scattering

The proton has always been considered one of the most important particles in physics. Discovered by Rutherford in 1920, it is one of the fundamental constituents of matter along with the neutron and the electron. This particle has been studied worldwide under every aspect, from its interactions with the other atom constituents to its internal structure.

It was thought therefore that every characteristic of the proton was known, until a study by Pohl *et al.* [75] published by *Nature* in 2010 cast some doubts on one of them: the charge radius.

Previously, the method commonly used to investigate the properties of atomic constituents, including protons, was electron-proton elastic scattering. Pohl *et al.* decided instead to extract the proton radius through spectroscopic measurements of the Lamb shift in muonic hydrogen. The measured radius was $r_p = 0.84184(67)$ fm, which differed from the 2006 recommended CODATA value of 0.8768(69) fm [68] by as many as five standard deviations.

This result gave birth to the so called "proton radius puzzle" and opened a still ongoing debate aimed at understanding whether this discrepancy is due to methodological problems or due to effects not contemplated by the Standard Model.

Since this debate mainly involves the two methodologies mentioned above, this chapter will focus on how to extract the charge radius of the proton from elastic scattering processes. The new procedures devised to extract the proton charge radius will be described in the following chapters.

1.1 Theory of electron-proton elastic scattering

An elastic scattering process happens when an incoming particle transfers its kinetic energy and momentum to a target particle without exciting any internal state. This kind of process is widely used to investigate the different properties of the atom and its components, and in the scope of the FAMU experiment the results of an electron-proton elastic scattering allow to derive the charge radius of the proton itself.

Let therefore the four-momenta of the incoming and outgoing electrons be $k_i = (\epsilon_i, \boldsymbol{k_i})$ and $k_f = (\epsilon_f, \boldsymbol{k_f})$ respectively, and let the initial and final four-momenta of the hadronic target be $P_i = (E_i, \boldsymbol{P}_i)$ and $P_f = (E_f, \boldsymbol{P}_f)$.

Since the scattering of charged particles is a form of electromagnetic interaction, its strength is essentially governed by the fine structure constant $\alpha = e^2(4\pi)^{-1}$, therefore it's possible to use the one photon exchange approximation [44].

Under this approximation the electron interacts with the hadronic currents at a well defined four-momentum and causes the production of a single virtual photon, which will then interact with the target particle. This in turn implies that the exchanged virtual photon has a four-momentum $q = (\omega, \boldsymbol{q}) = k_i - k_f$ depending only on the initial and final momentum of the electron.

The units used in the calculations are such that $\hbar = 1$ and $c = 1$, while the coordinates of the system are chosen according to

$$\hat{\mathbf{e}}_x = \hat{\mathbf{e}}_y \times \hat{\mathbf{e}}_z \qquad \hat{\mathbf{e}}_y = \frac{\hat{\mathbf{k}}_i \times \hat{\mathbf{k}}_f}{\sin\Theta} \qquad \hat{\mathbf{e}}_z = \hat{\mathbf{q}} \tag{1.1}$$

where $\Theta = \cos^{-1}(\hat{\mathbf{k}}_i \cdot \hat{\mathbf{k}}_f)$ is the scattering angle. The kinematics for a typical coincidence experiment are shown in Figure 1.1.

A generic scattering process may also lead to the production of one or more particles; this will not happen in the specific case of an elastic electron-proton scattering, but for the sake of clarity and completion let $p = (\epsilon_p, \mathbf{p})$ be the four momentum of a particle emitted as a result of the scattering.

Since the photon produced during the scattering is a virtual photon, its squared four momentum is negative; for this reason in the calculations it's easier to use the positive quantity $Q = -q^2$ instead.

The parameter Q^2 is particularly important because it's essentially the only free variable present in an elastic scattering process: momentum conservation laws guarantee that q, P_i and p are the only three independent momenta, and since the target and the produced particle are on-shell, it follows that $P_i^2 = M^2$, $p^2 = m_p^2$ and that only four independent scalars remain. A possible choice of these scalars is given by the momentum transfer and by the three Mandelstam variables

$$Q^2 \qquad s = (P_i + q)^2 \qquad t = (q - p)^2 \qquad u = (P_i - p)^2 \tag{1.2}$$

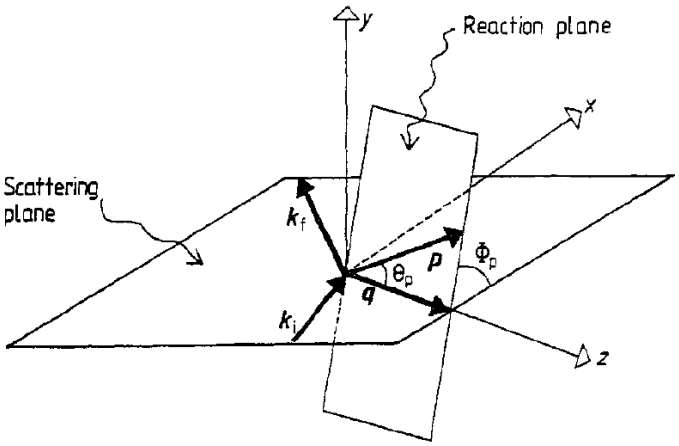

Figure 1.1: Kinematics for a typical coincidence experiment [44]. It can be seen that the process leads to an out-of-plane production of a particle with momentum equal to $\mathbf{p} = (|\mathbf{p}|, \Theta_p, \Phi_p)$.

In the specific case of an electron proton elastic scattering, however, $p \to 0$ and so $s = u = M^2$ and $t = -Q^2$; in other words, as stated above, Q^2 remains then the only free variable present.

Going back to the general case, under these hypotheses the differential cross section of a scattering process can be written as [44]

$$d\sigma = \frac{\epsilon_i}{k_i} \frac{d^3k_f}{(2\pi)^3} \frac{d^3p}{(2\pi)^3} \frac{d^3P_f}{(2\pi)^3} (2\pi)^4 \delta^{(4)}(P_i + q - p - P_f) |\langle P_f, p|J^\mu|P_i\rangle \frac{e^2}{q^2} \langle k_f|j_\mu|k_i\rangle|^2 \quad (1.3)$$

where ej_μ is the electron current and eJ_μ is the hadronic current; weak neutral currents caused by the exchange of Z^0 have been neglected.

In order to derive the cross section for an elastic scattering process it's necessary to evaluate each term of the equation according to more restrictive assumptions. First of all it's assumed that the hadronic state is unpolarized in its initial state, and that the incoming electron has longitudinal polarization $P_e = \pm 1$ for helicity eigenstates with $h = \sigma \cdot \hat{\mathbf{k}}_i = \pm 1$. This allows to sum and average the cross section in the final state over the degrees of freedom related to spin, while neglecting possible effects due to recoil polarization.

The elements of the squared transition matrix present in Equation (1.3) can be written as the product of two Lorentz tensors of rank two [42], the leptonic tensor $\eta_{\mu\nu}$ and the hadronic tensor $\widetilde{W}_{\mu\nu}$.

The leptonic tensor $\eta_{\mu\nu}$ can be expressed as

$$\eta_{\mu\nu} = \sum_{s_f} (\overline{u}(k_f, s_f)\gamma_\mu u(k_i, s_i))(\overline{u}(k_f, s_f)\gamma_\nu u(k_i, s_i))^* =$$

$$\frac{1}{2m_e^2}\left(2K_\mu K_\nu + \frac{1}{2}q^2 g_{\mu\nu} - \frac{1}{2}q_\mu q_\nu + ih\epsilon_{\mu\nu\alpha\beta}q^\alpha K^\beta\right) \quad (1.4)$$

where m_e is the electron mass, $K = \frac{1}{2}(k_i + k_f)$ is the average electronic four-momentum, h is the helicity of the incident electron as defined above, $g_{\mu\nu}$ is the symmetric metric tensor and $\epsilon_{\mu\nu\alpha\beta}$ is a completely antisymmetric tensor [44].

Equation (1.4) satisfies gauge invariance since

$$q^\mu \eta_{\mu\nu} = \eta_{\mu\nu} q^\nu = 0 \quad (1.5)$$

The hadronic tensor can be defined as follows:

$$\widetilde{W}_{\mu\nu} = \frac{1}{(2\pi)^3}\frac{1}{2J_i+1}\sum\!\!\!\!\!\!\int \sum_{M_i M_f s_p} \delta(E_i + \omega - \epsilon_p - E_f)$$

$$\times \langle P_f J_f M_f, p s_p | J_\mu | P_i J_i M_i \rangle * \langle P_f J_f M_f, p s_p | J_\nu | P_i J_i M_i \rangle = \epsilon_p W_{\mu\nu} \quad (1.6)$$

where the symbol $\sum\!\!\!\!\!\!\int$ in the formula denotes a sum over the accessible states of the residual nucleus, with energy E_f, angular momentum J_f, and any other internal quantum number.

The evaluation of the hadronic tensor is more complex than the one for the leptonic tensor, and effectively requires the implementation of a nuclear model. However, by using Equation (1.5), it's possible to simplify the task by replacing all time-like elements of $W_{\mu\nu}$ with space-like ones, whose direction is given by $\hat{\mathbf{e}}_z = \hat{\mathbf{q}}$.

The space directions that appear in the hadronic tensor are related to the absorption of polarized virtual photons. In this case the photon has polarization equal to [29, 44]

$$\epsilon = \left(1 + 2\frac{\mathbf{q}^2}{Q^2}\tan^2\frac{\Theta}{2}\right)^{-1} \quad (1.7)$$

with $\mathbf{q}$ and Θ evaluated in the lab frame.

The degree of freedom relative to the transverse polarization is then

$$\epsilon_L = \frac{\epsilon Q^2}{\omega^2} \quad (1.8)$$

By applying gauge invariance it can also be proved that the explicit calculation of $W_{\mu\nu}$ contains at most nine independent elements, six for the symmetric part and three for the antisymmetric one.

Under these assumptions and formulas, Equation (1.3) can be rewritten as

$$\frac{d\sigma}{d\Omega_f\, d\epsilon_f\, d^3p} = \Gamma \frac{d\sigma_v}{d\Omega_f} \tag{1.9}$$

where the right hand side is the product between the flux of the virtual photon field Γ and the differential cross section of the virtual photon itself. They can be expressed as follows:

$$\Gamma = \frac{\alpha}{2\pi^2} \frac{\epsilon_f}{\epsilon_i} \frac{k_\gamma}{Q^2} \frac{1}{1-\epsilon} \tag{1.10}$$

$$\frac{d\sigma_v}{d\Omega_f} = \frac{4\pi^2\alpha}{k_\gamma} \left(\frac{W_{xx}+W_{yy}}{2} + \epsilon_L W_{zz} - \sqrt{2\epsilon_L(1+\epsilon)}\,\mathrm{Re}(W_{zx}) + \epsilon \frac{W_{xx}-W_{yy}}{2} \right.$$
$$\left. - P_e \sqrt{2\epsilon_L(1-\epsilon)}\,\mathrm{Im}(W_{yz}) \right) \tag{1.11}$$

where $k_\gamma = (W^2 - m_i^2)/2m_i$ is the photon equivalent energy.

The five terms composing Equation (1.11) contain one structure function $W_{ik} = W_{ik}(Q^2, \omega, \epsilon_p, \Theta_p)$ each that depends on four independent variables only. Furthermore, not all five terms depend on the azimuthal angle Φ_p.

In order to better show the dependencies of each term, Equation (1.11) can be also written as

$$\frac{d\sigma_v}{d\Omega} = \frac{d\sigma_T}{d\Omega} + \epsilon_L \frac{d\sigma_L}{d\Omega} + \sqrt{2\epsilon_L(1+\epsilon)} \frac{d\sigma_{LT}}{d\Omega} \cos\Phi_p + \epsilon \frac{d\sigma_{TT}}{d\Omega} \cos 2\Phi_p$$
$$+ P_e \sqrt{2\epsilon_L(1-\epsilon)} \frac{d\sigma'_{LT}}{d\Omega} \sin\Phi_p \tag{1.12}$$

The first and the second terms are the transverse and longitudinal structure functions respectively. They can be decomposed into a series of $\cos\Theta_p$, and as such they do not depend on the azimuthal angle Φ_p. The third and fifth term contain the description of the longitudinal-transverse interferences; due to their dependence on the angle Φ_p they must have in their definition an explicit factor $\sin\Theta_p$, which makes them go to zero along the axis of momentum transfer. The same can be said for the fourth term, ie the transverse-transverse interference term, which contains a factor $\sin^2\Theta_p$.

Equations (1.11) and (1.12) can be written as a function of the Mott cross section by introducing five response functions, one for each term [31, 42]:

$$W_T = W_{xx} + W_{yy} \tag{1.13}$$

$$W_L = \frac{\mathbf{q}^2}{\omega^2} W_{zz} = W_{00} \tag{1.14}$$

$$\cos\Phi_p \, W_{TL} = 2\sqrt{2}\frac{|\mathbf{q}|}{\omega} \operatorname{Re} W_{xz} = 2\sqrt{2} \operatorname{Re} W_{x0} \tag{1.15}$$

$$\cos 2\Phi_p \, W_{TT} = W_{yy} - W_{xx} \tag{1.16}$$

$$\sin\Phi_p \, W'_{TL} = 2\sqrt{2}\frac{|\mathbf{q}|}{\omega} \operatorname{Im} W_{yz} = 2\sqrt{2} \operatorname{Im} W_{y0} \tag{1.17}$$

Using these response functions, the cross section becomes

$$\frac{d\sigma}{d\Omega_f \, d\epsilon_f \, d^3p} = \left(\frac{d\sigma}{d\Omega}\right)_{Mott} \big(V_L W_L + V_T W_T + V_{TL} W_{TL} \cos\Phi_p + V_{TT} W_{TT} \cos 2\Phi_p + P_e V'_{TL} W'_{TL} \sin\Phi_p\big) \tag{1.18}$$

where $(\frac{d\sigma}{d\Omega})_{Mott}$ is the Mott cross section and the factors V_{ik} are kinematic factors. If the rest mass of the electron is neglected, they can expressed as

$$\left(\frac{d\sigma}{d\Omega}\right)_{Mott} = \left(\frac{\alpha \cos\frac{\Theta}{2}}{2\epsilon_i \sin^2\frac{\Theta}{2}}\right)^2 \tag{1.19}$$

and

$$V_L = \left(\frac{Q^2}{\mathbf{q}^2}\right)^2 \tag{1.20}$$

$$V_T = \frac{Q^2}{2\mathbf{q}^2} + \tan^2\frac{\Theta}{2} \tag{1.21}$$

$$V_{TL} = -\frac{Q^2}{\sqrt{2}\mathbf{q}^2}\left(\frac{Q^2}{\mathbf{q}^2} + \tan^2\frac{\Theta}{2}\right)^{\frac{1}{2}} \tag{1.22}$$

$$V_{TT} = -\frac{Q^2}{2\mathbf{q}^2} \tag{1.23}$$

$$V'_{TL} = -\frac{Q^2}{\sqrt{2}\mathbf{q}^2}\tan\frac{\Theta}{2} \tag{1.24}$$

In order to find the cross section for the inclusive process, ie a process where only the scattered lepton is considered and detected, Equation (1.18) has to be integrated over the momenta of the emitted particle $\mathbf{p} = \mathbf{p}_c$. The result must then be summed over all

open channels c. Since the last three terms in Equation (1.18) depend explicitly on the azimuthal angle Θ_p, they all get eliminated during the procedure, therefore only the first two structure functions remain.

By defining the remaining inclusive response functions, ie the transversal and longitudinal functions, as

$$R_{L/T}\left(\omega, Q^2\right) = \sum_c \int d^3p_c W^{(c)}_{L/T}\left(\omega, Q^2, \epsilon_p, \Theta_p\right) \tag{1.25}$$

the cross section of the inclusive process becomes

$$\frac{d\sigma}{d\Omega_f\, d\epsilon_f} = \left(\frac{d\sigma}{d\Omega}\right)_{Mott} \left(V_L R_L(\omega, Q^2) + V_T R_T(\omega, Q^2)\right) \tag{1.26}$$

It's important to notice that the decomposition of the cross section into a set of independent structure functions is valid as long as the single photon approximation itself is valid.

For the electron-proton scattering this approximation has been tested by measuring the ratio of the positron to electron cross section [48, 77, 87]. The value of the ratio was found to be consistent with unit, and the fluctuations measured were of the order of 1%. This result was confirmed also in case muons are substituted to the electrons.

Given these general premises, in the specific case of elastic electron-proton scattering the hadronic target system is a proton, that is a particle with spin equal to $\frac{1}{2}$. This implies that the calculations have to consider not only the degrees of freedom relative to the momenta, but also those related to the spin.

The spin's degrees of freedom are described by the transition current of the target proton, which can be written in its most general form as [29, 42]

$$\hat{\mathbf{J}}_\mu = \tilde{\gamma}_\mu F_1\left(Q^2, m_i, m_f\right) + \frac{i\sigma_{\mu\nu}q^\nu\kappa}{2\overline{m}} F_2\left(Q^2, m_i, m_f\right) \tag{1.27}$$

where $\tilde{\gamma}_\mu$ is a gauge invariant Lorentz vector and $\overline{m} = \frac{1}{2}(m_i + m_f)$; the parameter κ is the anomalous magnetic moment defined as $\kappa = \mu_p - 1$, where μ_p is the magnetic moment of the target proton.

Since during an elastic scattering process the mass of the target doesn't change, ie $m_i = m_f = M$, it follows that the two form factors F_1 and F_2 depend only on the transferred momentum $Q^2 = -q^2$. By using the normalization $F_i(0, M, M) = F_i(0) = 1$ for protons, the two form factors F_1 and F_2 become Dirac and Pauli form factors.

Although these form factors can be used as they are for evaluating the hadronic tensor and the cross section, it's easier to translate the Pauli and Dirac form factors into the electric and magnetic Sachs form factors, and use the latters instead. The translation can be performed through the relationships

$$G_E = F_1 - \tau\kappa F_2 \qquad\qquad G_M = F_1 + \kappa F_2 \tag{1.28}$$

with $\tau = Q^2/4M^2$ and normalization given by $G_E(0) = F_1(0) = 1$, $G_M(0) = \mu_p$.

By using the Sachs form factors and by introducing the gauge invariant vector $P_\mu = \tilde{\mu} - \frac{P\cdot q}{q^2} q_\mu$ it's possible to rewrite Equation (1.27) into

$$\langle f|\hat{\mathbf{J}}_\mu(q)|i\rangle = \sqrt{\frac{M^2}{E_i E_f}}\overline{u}_f \left(\frac{\tilde{P}_\mu}{m}\frac{G_E^2 + \tau G_M^2}{1+\tau} + \frac{i\sigma_{\mu\nu}q^\nu}{2M} G_M \right) u_i \tag{1.29}$$

This new form allows in turn to evaluate the hadronic Lorentz tensor defined through Equation (1.6) for the elastic electron-proton scattering:

$$\tilde{W}_{\mu\nu}^{(el)} = \delta\left(\omega - \frac{Q^2}{2M}\right)\left(\frac{G_E^2 + \tau G_M^2}{1+\tau}\frac{\tilde{P}_\mu \tilde{P}_\nu}{M^2} - \tau G_M^2 \tilde{g}_{\mu\nu} \right) \tag{1.30}$$

with $\tilde{g}_{\mu\nu} = g_{\mu\nu} - q_\mu q_\nu / q^2$.

The cross section for the elastic electron-proton scattering can be derived from Equations (1.18)-(1.24), (1.26) and (1.30) by integrating over ϵ_f [44]. The result is the so called Rosenbluth cross section

$$\left(\frac{d\sigma}{d\Omega}\right)_{Ros} = \frac{4\alpha^2\epsilon_f^2 \cos^2\frac{\Theta}{2}}{Q^4}\frac{1}{1 + 2\frac{\epsilon_i}{M}\sin^2\frac{\Theta}{2}}\left(\frac{G_E^2 + \tau G_M^2}{1+\tau} + 2\tau G_M^2 \tan^2\frac{\Theta}{2} \right) \tag{1.31}$$

The multiplicative factor in Equation(1.31) can be interpreted as the Mott cross section corrected to take into account the recoil

$$\left(\frac{d\sigma}{d\Omega}\right)_{Mott*} = \frac{4\alpha^2\epsilon_f^2 \cos^2\frac{\Theta}{2}}{Q^4}\frac{1}{1 + 2\frac{\epsilon_i}{M}\sin^2\frac{\Theta}{2}} \tag{1.32}$$

Note that some sources may prefer to approximate $\cos^2\frac{\Theta}{2}$ to $(1 - \beta^2\sin^2\frac{\Theta}{2})$ due to the fact that, depending on the energy scales of the process, β may be close to unity. For the sake of completeness here the full formula has been proposed.

Using the Mott cross section the structure of the Rosenbluth formula can be simplified into [29, 44]

$$\left(\frac{d\sigma}{d\Omega}\right)_{Ros} = \left(\frac{d\sigma}{d\Omega}\right)_{Mott*}\frac{1}{1+\tau}\left(G_E^2(Q^2) + \frac{\tau}{\epsilon}G_M^2 \right) \tag{1.33}$$

where the photon polarization defined in Equation (1.7) has been rewritten as

$$\epsilon = \left(1 + 2(1+\tau)\tan^2\frac{\theta}{2}\right)^{-1} \tag{1.34}$$

From the Rosenbluth cross section it is then possible to extrapolate the mean squared charge and magnetic radii of the proton through

$$\langle r_E^2 \rangle = -\frac{6}{G_E(0)} \left.\frac{dG_E(Q^2)}{dQ^2}\right|_{Q^2=0} \tag{1.35}$$

$$\langle r_M^2 \rangle = -\frac{6}{G_M(0)} \left.\frac{dG_M(Q^2)}{dQ^2}\right|_{Q^2=0} \tag{1.36}$$

It follows that the radii of the proton can be derived from the slope of the form factors at $Q^2 = 0$.

1.2 Measurements of the proton radius through the form factors

Many experiments and analysis were performed in the last few decades in order to measure the proton radius through G_E and G_M. Between them, the ones that CODATA considered most between 2010 and 2021 in their proposals of the optimal proton radius value [67, 69, 82] were the experiment conducted by Bernauer *et al.* in 2010 [28, 29] and the data review performed by Arrington and Sick in 2015 [23].

The experiment of Bernauer *et al.* employed the three high resolution spectrometers of the A1 collaboration in order to measure about 1400 elastic electron proton scattering cross sections; the energy of the electron beam produced by the Mainz linear electron accelerator MAMI ranged from 180 to 855 MeV, covering the four momentum squared Q^2 from 0.004 to 1 $(\mathrm{GeV/c})^2$. The statistical precision on the measure of the cross section was better than 0.2% and this allowed to extract the electric and magnetic form factors up to $Q^2 = 0.6$ $(\mathrm{GeV/c})^2$.

The floorplan of the accelerator and of the MAMI facility is shown in Figure 1.2: the accelerator apparatus is composed by three race track microtrons, abbreviated RTMs, and by an harmonic double sided microtron, or HDSM. The hall in the lower right of the image is the one containing the target and the three high resolution spectrometers, whose arrangement can be seen in Figure 1.3.

The magnetic system of spectrometer A and C consists of a quadrupole, a sextupole and two dipoles; this system allows high resolution measurements of particle momentum and angle inside a rather large angular acceptance of maximum 28 msr. Spectrometer B is instead equipped with a single dipole magnet in a clamshell configuration; this results in a slimmer design, with higher spatial resolution and a smaller acceptance of 5.6 smr.

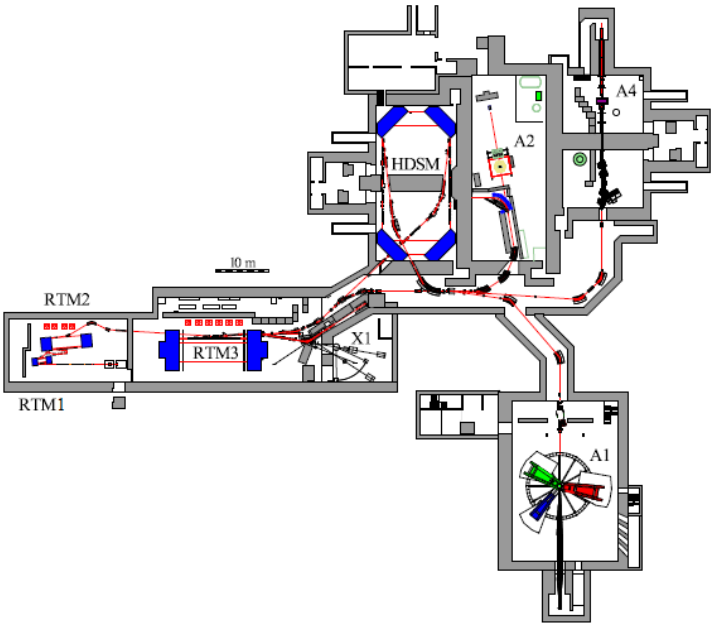

Figure 1.2: Schematic floor plan of the MAMI accelerator [29]. The hall with the three spectrometers and the target is the one located in the lower right.

As for the momentum, all three of them were proved to have resolution of 10^{-4}. Figure 1.4 shows the optical scheme of the spectrometers described above.

Each spectrometer is equipped on top with the the detector system reported in Figure 1.5. This system consists of two vertical drift chamber layers (VDC), two scintillator planes and a gas-Cherenkov detector.

The two scintillator planes provide the triggering and the time reference. The different thickness of the two layers, 3 mm and 1 cm respectively, allow to classify minimum ionizing particles (or MIPs for short) from heavier ones through their different energy deposition.

The vertical drift chambers are used to reconstruct the trajectory of the particles. Along the dispersive direction the spatial resolution is better than 200 μm, while along the non dispersive one it's 400 μm.

The last component, the Cherenkov detector, is used to distinguish between electrons and heavier particles.

During the experiment of Bernauer *et al.*, the form factors were obtained with two different procedures. The first is the so called "Rosenbluth separation" method, which considers G_E and G_M as linear fit parameters for the cross section as a function of ϵ. Equation 1.33 can in fact be rewritten and used to define the reduced cross section [29]

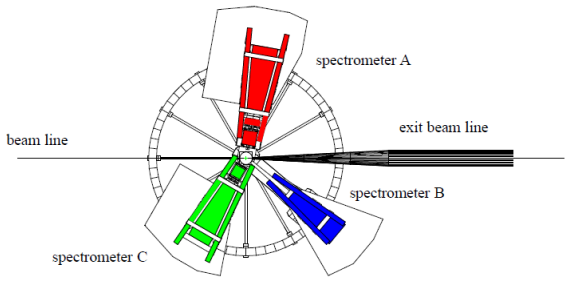

Figure 1.3: Arrangement of the three spectrometers at MAMI [29].

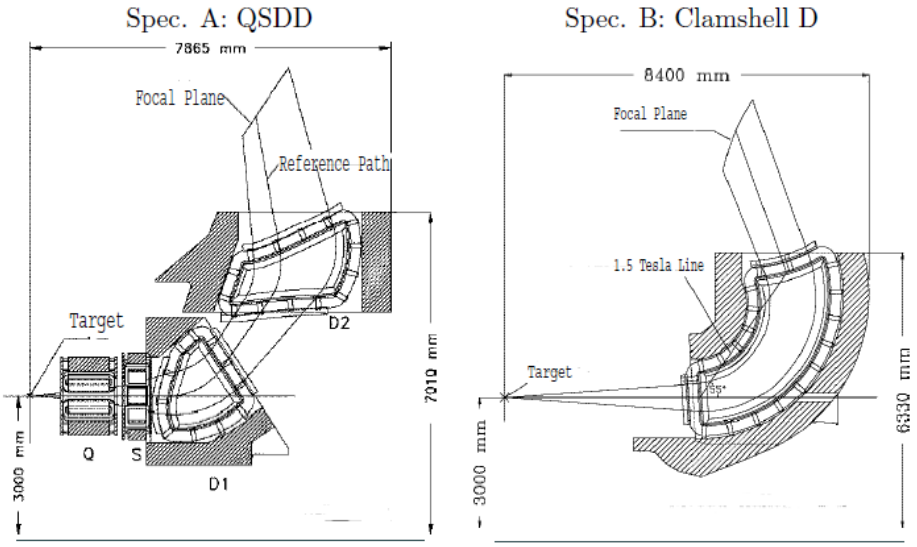

Figure 1.4: Scheme of spectrometers A and B. The scheme of spectrometer C is a scaled down version of the one for spectrometer A [29].

$$\sigma_{red} = \frac{\left(\frac{d\sigma}{d\Omega}\right)_{Ros}}{\left(\frac{d\sigma}{d\Omega}\right)_{Mott*}} (1+\tau)\frac{\epsilon}{\tau} = G_M^2 + \frac{\epsilon}{\tau}G_E^2 \tag{1.37}$$

from which the two form factors can be extrapolated as fit parameters when Q^2 is fixed. The parameterization chosen to describe G_E and G_M was the standard dipole parameterization

$$G_{std.dip.} = G_E = \frac{G_M}{\mu_p} = \left(1 + \frac{Q^2}{0.718\,(GeV/c^2)}\right)^{-2} \tag{1.38}$$

where μ_p is the proton's magnetic dipole moment divided by the nuclear magneton.

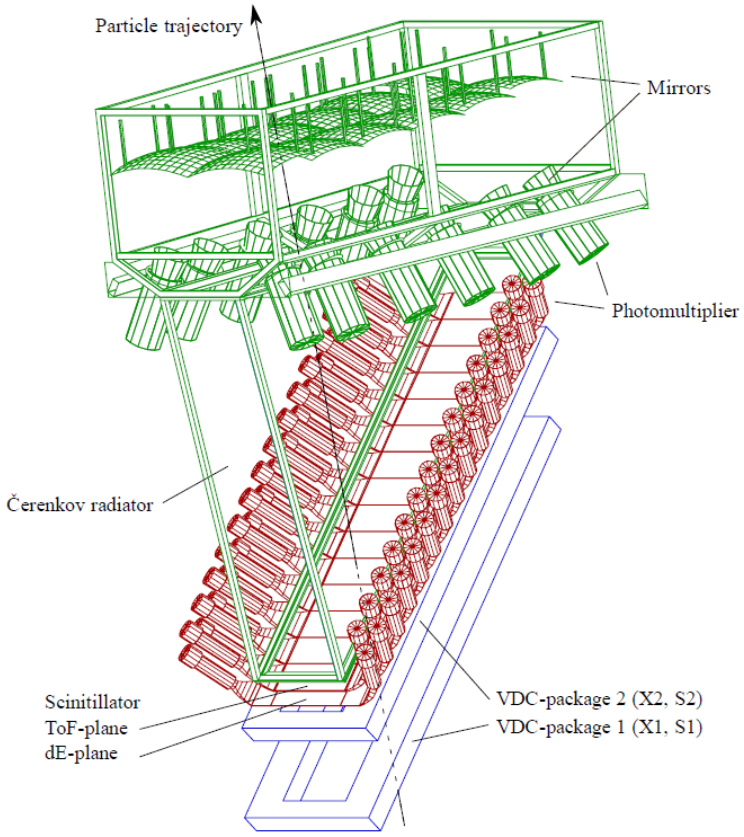

Figure 1.5: Representation of the detector system at the end of each spectrometer [29].

The problem with this method is that the data have to be taken for a wide range of ϵ at constant Q^2, and given the limitations on the energy and angular ranges covered by the spectrometers, the kinematical range that is possible to cover is restricted.

The second procedure is aimed at providing a solution to this: it involves a direct least-squares fit of the models for the form factors to the measured cross sections for every Q^2 and θ. In order to limit as much as possible model dependence, a wide range of different models were employed, including, but not limited to, single-dipole, sum-of-dipoles, polynomials, spline-based models and a variation of the Gari-Krümpelmann model.

The results of the direct fit were generally compatible with those coming from the Rosenbluth separation where such comparison was possible. In general however the Rosenbluth approach was found to be more sensitive to systematic deviations and was considered therefore a worse estimator for G_E and G_M.

Figure 1.6 shows the form factors obtained from the Rosenbluth separation, while Figure 1.7 and Figure 1.8 show respectively the electric and magnetic form factors

obtained from the direct fits.

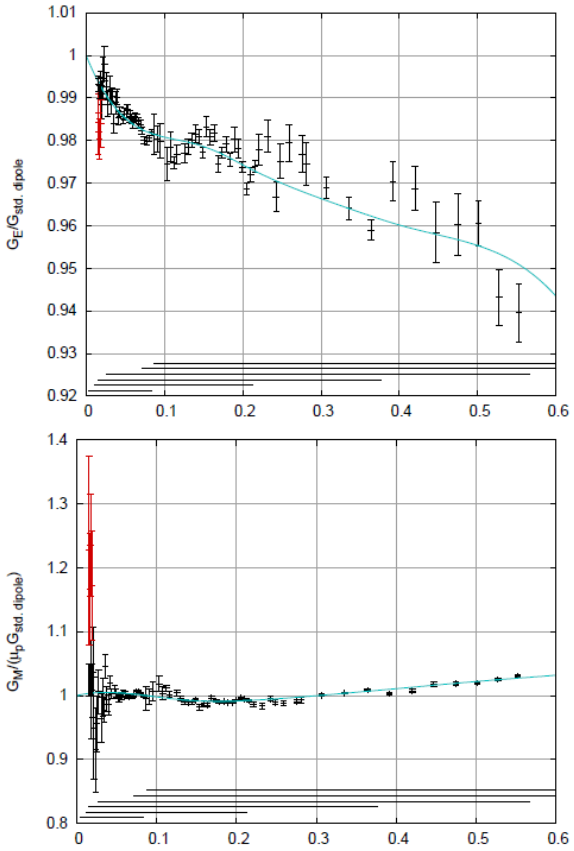

Figure 1.6: Electric and magnetic form factors obtained from the Rosenbluth separation (black line) and normalized to the standard dipole (see Equation 1.38) compared to the spline fit (cyan curve). The results of an unrestrained fit are shown in red [29].

The value of the proton charge radius obtained by Beranuer *et al.* using these data on the form factors was [28, 29]

$$\langle r_E^2 \rangle^{\frac{1}{2}} = 0.879(5)_{stat.}(4)_{syst.}(2)_{model}(4)_{group}\ fm \tag{1.39}$$

The additional uncertainty term "group" is caused by a slight difference in the values extracted from the spline group and the polynomial group.

It's important to notice that Bernauer *et al.* in their experiments decided to not consider corrections for the exchange of two hard photons, abbreviated TPE, due to the fact that at the time no unique description existed yet. This decision, along with the choices made on the uncertainties of the data, raised several problems related to how to combine the results obtained at MAMI with the remaining available data. Several analyses were conducted in order to find the best estimate of the proton radius from all

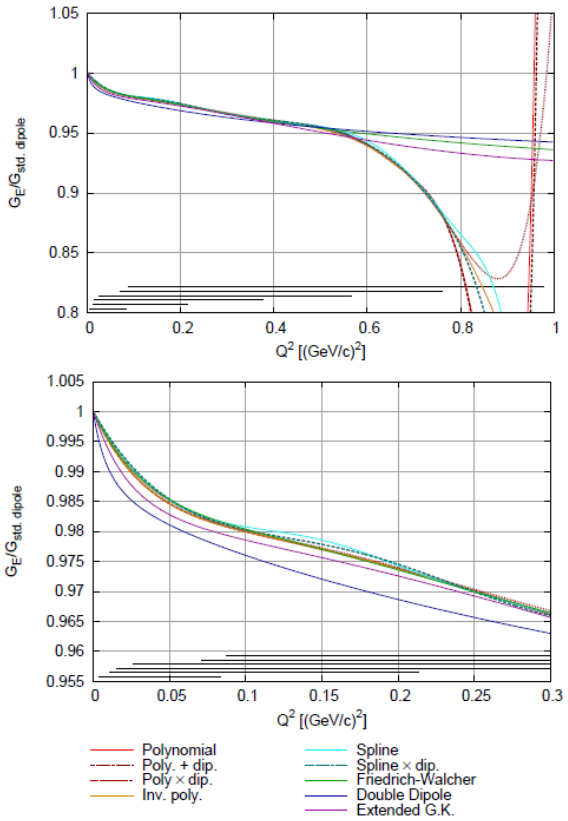

Figure 1.7: Electric form factor normalized to the standard dipole (see Equation 1.38) as a function of Q^2 for different fits [29].

available data, and between them, according to CODATA [67, 82], the analysis performed by Arrington and Sick [23] was particularly accurate.

In their work, Arrington and Sick considered only fits with the explicit aim of extracting the proton radius from the electric and magnetic form factors at low Q^2. Single parameter fits were also excluded due to the fact that the Q^2 range needed to reach a useful limit for the radius exceeds the range in which the fit is precise enough to represent the data.

Arrington and Sick focused their attention also on the corrections applied by Beranuer *et al.* in their experiment [28, 29], and found that they're valid only for scattering from a point nucleus. In the limit $Q^2 \to 0$ this approximation is valid, but at nonzero Q^2 values the Coulomb distortion correction and the TPE correction gain a Q^2 dependence that influences the slope of $G_E(Q^2)$ as $Q^2 \to 0$.

Using the researches available at the time they examined the dependence of TPE corrections on Q^2, and concluded that TPE calculation considered valid at low Q^2 are in very good agreement below the value $Q^2 = 0.2\ GeV^2$. Arrington and Sick decided therefore to consider extractions of the electric and magnetic radii from the MAMI

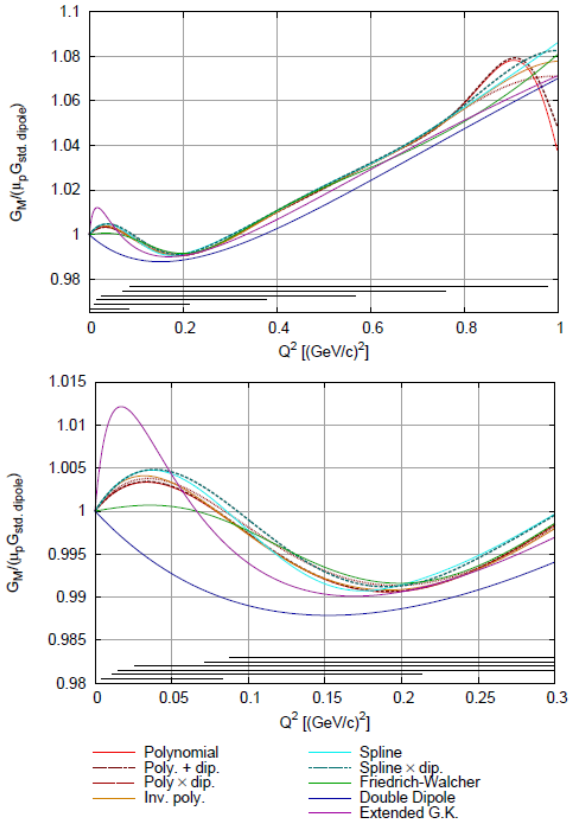

Figure 1.8: Magnetic form factor normalized to the standard dipole (see Equation 1.38) as a function of Q^2 for different fits [29].

data that included both the hadronic TPE corrections and the estimate for the model dependence of such corrections.

Under these premises, the values extracted from the MAMI data were $r_E = 0.875(15)$ fm and $r_M = 0.799(28)$ fm, while those extracted from the remaining worldwide data were $r_E = 0.881(11)$ fm and $r_M = 0.867(20)$ fm. Just combining them was deemed impossible, and since there was no clear way on how to treat the uncertainty on the combined results, the authors made what they called a "relatively arbitrary decision": they chose to consider primarily the discrepancy in r_M due its higher sensitivity on corrections and fit functions, and to use it in order to estimate possible systematic errors in r_E.

The recommended value proposed by Arrington and Sick for the proton root mean square charge radius at the end of their analysis was $r_E = 0.879 \pm 0.011$ fm [23].

Of course, although the works of Bernauer *et al.* and of Arrington and Sick can be considered an important contribution on the study of the proton radius, the debate is still ongoing. In particular numerous studies are being carried on in order to improve the knowledge about the corrections to the calculation, to reach higher accuracy in the

extraction of the radius and to investigate the reason behind the discrepancies between the radius values.

Chapter 2

Theory of hydrogen and muonic hydrogen energy levels

Spectroscopy has been a fundamental tool in studying the properties of the atom since Rutherford's time and is still widely used in quantum mechanics. The study of the hydrogen atom and its energy levels has been particularly important since it allowed to verify the effects predicted by Shroedinger and Dirac's equations, as well as those determined by QED.

This chapter will cover the theoretical calculations behind the hydrogen's and the muonic hydrogen's energy levels.

2.1 Dirac energy levels

Assuming in first approximation a nonrelativistic system composed by a pointike proton with infinite mass and an electron in a central Coulomb potential, the energy levels of the atom are described by the solutions of the Schroedinger equation [47]

$$\begin{aligned} &\left(-\frac{\Delta}{2m}-\frac{Z\alpha}{r}\right)\Psi(\boldsymbol{r})=E_n\,\Psi(\boldsymbol{r}) \\ &\Psi(\boldsymbol{r})=R_{nl}(r)\,Y_{lm}\left(\frac{\boldsymbol{r}}{r}\right) \\ &E_n=-\frac{m_e\,(Z\alpha)^2}{2n^2},\quad n=1,2,3,\ldots \end{aligned} \tag{2.1}$$

where Z is the atomic number of the nucleus. The value of c has been put equal to 1. Each state is described by three quantum numbers: the main quantum number n, the orbital angular momentum $l=0,1,\ldots,n-1$ and its projection $m=0,\pm1,\ldots,\pm l$.

Finiteness of the nucleus mass can be included by introducing the reduced mass $m_r=(m_eM)/(m_e+M)$, that for hydrogen assumes approximately the value $0.9995\,m_e$.

In the nonrelativistic case the introduction of the reduced mass allows to fully describe the two-body system.

It's important to note, however, that in this first nonrelativistic approximation l and m do not contribute to Equation 2.1, therefore all states with same principal quantum number are degenerate. This degeneracy can be partially lifted by introducing relativistic corrections, represented by expansions over even powers of $Z\alpha$. The contribution of the electron spin is also necessary for a complete treatment of the energy levels since it produces a change in the coefficients of the $Z\alpha$ expansions describing the relativistic corrections [47].

The corrected energy levels can then be obtained from the Dirac equation for a static Coulomb source [19, 47]:

$$E_{nj} = m_e f(n, j) \tag{2.2}$$

$$\begin{aligned} f(n,j) &= \left[1 + \frac{(Z\alpha)^2}{\left(\sqrt{\left(j+\frac{1}{2}\right)^2 - (Z\alpha)^2} + n - j - \frac{1}{2} \right)^2} \right]^{-\frac{1}{2}} \\ &\approx 1 - \frac{(Z\alpha)^2}{2n^2} - \frac{(Z\alpha)^4}{2n^3}\left(\frac{1}{j+\frac{1}{2}} - \frac{3}{4n}\right) \\ &\quad - \frac{(Z\alpha)^6}{8n^3}\left[\frac{1}{\left(j+\frac{1}{2}\right)^3} + \frac{3}{n\left(j+\frac{1}{2}\right)^2} + \frac{5}{2n^3} - \frac{6}{n^2\left(j+\frac{1}{2}\right)}\right] + \cdots \end{aligned} \tag{2.3}$$

where $j = 1/2, 3/2, \ldots, n - 1/2$ is the sum of the orbital angular momentum l and the spin angular momentum s of the electron.

Energy levels with same n but different j are divided by Equation 2.3 into n components of the fine structure, while those with same n and j but different $l = j \pm \frac{1}{2}$ remain doubly degenerate. In order to split them, new corrections connected to the finite size of the proton, to recoil contributions and to dominating QED loop contributions need to be considered. The energy corrections that lift the $l = j \pm \frac{1}{2}$ double degeneracy are collectively called Lamb shifts [19, 47].

There is one last level of degeneracy, which is related to the interaction between the nuclear magnetic dipole moments of the proton and of the electron. The new energy levels obtained when this last level of degeneracy is lifted from the hyperfine structure, and the difference between these energy levels is called hyperfine splitting [51].

By considering each and every correction, the total energy of the electron located in the level described by the set of quantum numbers (n, j, l, F), with F being the total angular momentum of the proton-electron system, is [19, 47]

$$E^{tot}_{njlF} = (m_e + M) + [f(n,j) - 1]\, m_r - [f(n,j) - 1]^2 \frac{m_r^2}{2(m_e + M)} + L_{njl} + E^{hfs}_{njlF} \tag{2.4}$$

Figure 2.1 shows the energy levels for ordinary hydrogen.

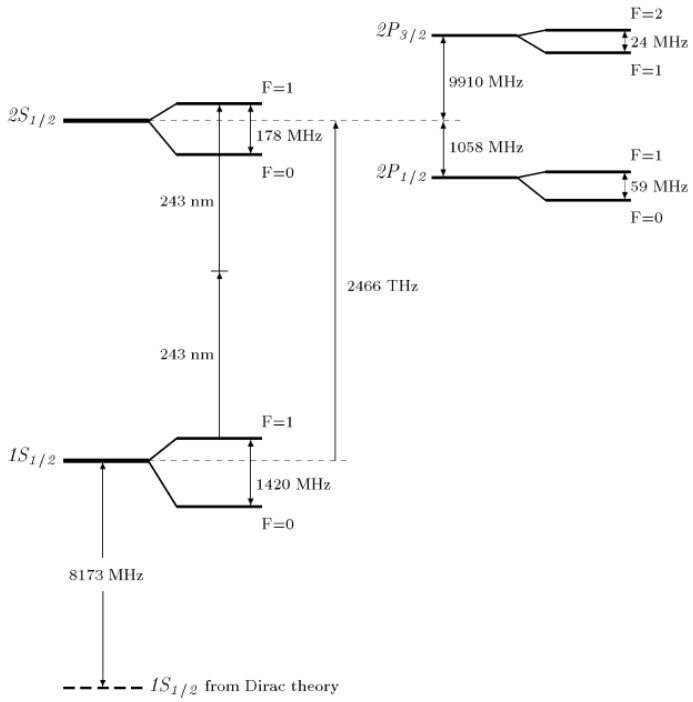

Figure 2.1: S and P energy levels for ordinary hydrogen [47].

2.2 Classification of corrections

Dirac's equation alone is not enough to describe accurately the energy levels of hydrogen-like atoms: corrections are needed in order to reach an optimal understanding of the bound states, and they require not only a quantum mechanical treatment but also methods of field theory.

All electrodynamic corrections to the energy levels can be written as series expansions over the three small dimensionless parameters α, $Z\alpha$ and m_e/M, which effectively define the properties of the bound state. Additional non electromagnetic corrections caused by strong and weak interactions may introduce other parameters, like the ratio of the

nuclear radius and the Bohr radius. Furthermore, the coefficients of the aforementioned power series might themselves be varying functions, more precisely logarithms, of such parameters.

Corrections are generally classified in groups according to the factors on which they depend [47]. In general, low order corrections related to a specific group can be calculated independently from the ones of other groups, but higher order terms may contain mixed contributions.

The main groups and their characteristics are listed below.

Relativistic corrections : also called *binding corrections*, they consider deviations of the theory from the nonrelativistic limit and take the form of a series expansion depending only on the parameter $Z\alpha$. For this reason $Z\alpha$ is often called the *binding parameter*. All these contribution are part of the spectrum of the effective Dirac equation in an external Coulomb field.

Radiative corrections : contributions of this specific category depend on both α and $Z\alpha$. These corrections derive from quantum field theory and take into account quantum electrodynamics loops, like the electron self-energy and the vacuum polarization shown in Figure 2.2. Since they do not depend on the factor m_e/M it's possible to calculate them in the QED framework for a bound electron in an external field. The two-particle nature of the bound state and all the problems related to the description of bound states in relativistic quantum field theory may be neglected in the calculations of this type of contribution [47].

Recoil corrections : they describe those contributions to the energy levels that escape the scope of the introduction of the reduced mass m_r. In other words these corrections arise when the one-body approximation fails and a true two-body theoretical treatment is needed. They depend on $Z\alpha$ and on the so called *recoil parameter* m_e/M.

Radiative-recoil corrections : they have a mixed nature and depend simultaneously on the paramters α, $Z\alpha$ and m_e/M. Their calculation considers both the purely radiative loops and the relativistic two-body nature of the bound states.

Nuclear structure corrections : they describe the effects of the finite size of the nucleus and the nucleus polarization. An example of these effects is the reduced attraction perceived by the electron compared to that perceived in the case of a point-like nucleus. These corrections represent a serious problem in high-precision spectroscopy since their uncertainties are the highest [15, 19, 47] (for comparison, see Table 2.1, 2.2, 2.4 and 2.5).

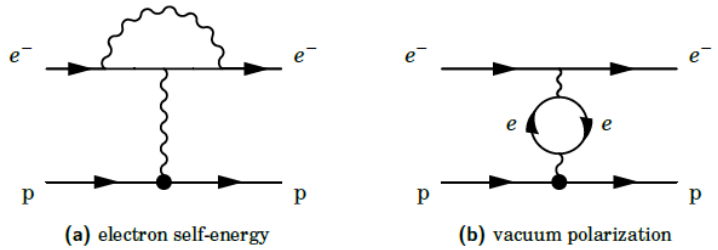

Figure 2.2: Feynman diagrams describing the leading contributions to the electron self-energy (a) and to the vacuum polarization (b) [52].

Non electromagnetic corrections : they consider the effects of weak and strong interactions. The contribution of this category with the highest value is related to the finite size of the nucleus.

2.3 The Lamb shift

The Lamb shift is a shift of the energy levels that is not predicted by the Dirac equation. First measured by Lamb and Retherford in 1947 [60], it can be considered one of the cornerstones of modern quantum electrodynamics. Its importance is such that Lamb himself won the Nobel Prize in Physics in 1955 thanks to its discovery. The Lamb shift may be defined as the sum of all the contributions to the energy levels of the bound states that lift the degeneracy in the Dirac-Coulomb spectrum with respect to $l = j \pm 1/2$.

The leading corrections to the Lamb shift from most to least relevant corresponds to radiative, recoil, radiative-recoil and nuclear structure corrections, as shown in Table 2.1.

Contribution	$1S$ state $[kHz]$	Uncertainty $[kHz]$	$2S$ state $[kHz]$	Uncertainty $[kHz]$
Radiative (one-loop)	8 181 285.5	0.2	1 046 061.43	4×10^{-2}
Radiative (two-loop)	721	24	90.2	3×10^{-1}
Recoil	2 402.118	0.002	340.3646	3×10^{-4}
Radiative-recoil	−12 777.97	0.04	−1 635.437	5×10^{-3}
Finite nuclear size	1 167	32	145.8	4
Sum	8 172 798	(32)(24)	1 045 002.4	(4.0)(0.3)

Table 2.1: Theoretical expectation of the Lamb shift for the $1S$ and $2S$ bound states [19]. The first uncertainty of the sum of the contributions refers to the pure theoretical uncertainty, while the second refers to the uncertainty of the proton radius extracted from scattering experiments.

The main contribution to both the radiative corrections and the Lamb shift itself is the electron self-energy, which consists in the emission and the re-absorption of one or multiple

virtual photons by the electron (see Figure 2.2 (a)). The leading term in the self-energy calculation is given by the one-loop self-energy, but high precision measurements require also the higher order correction terms describing additional loops. For more details about one-loop and two-loop self-energy calculations and their mass renormalization, as well as recoil and radiative-recoil corrections, see [19, 47].

The last contribution to the Lamb shift is given by finite nuclear size corrections and is caused by the spreading of the electron's charge: the constant emission and absorption of virtual photons, in fact, makes the electron appear as if its charge were distributed over a finite volume instead of being point-like. The finite radius of the electron produces a deviation from the Coulomb potential $V = -Z\alpha/r$ equal to [19, 47, 52]

$$\delta V = \frac{1}{6}\langle r^2 \rangle \Delta V = \frac{2\pi}{3} Z\alpha \langle r^2 \rangle \delta(r) \tag{2.5}$$

The smearing of the electron charge across a finite volume leads therefore to a binding energy that is smaller than the one felt by a point-like electron. Furthermore, since this effect is nonvanishing only at the source of the Coulomb potential itself, it influences in a different way energy levels with different angular momenta. Bound states with same total angular momentum j but different angular momenta l are thus splitted.

The energy shift produced by the variation of the Coulomb potential can then be expressed as [19, 47]

$$\Delta E = \langle \Psi(r) \left| \delta V \right| \Psi(r) \rangle = \left| \Psi_n(0) \right|^2 \frac{2\pi \left(Z\alpha \right)}{3} \langle r^2 \rangle = \frac{2m_r^3 \left(Z\alpha \right)^4}{3n^3} \langle r^2 \rangle \delta_{l0} \tag{2.6}$$

It's possible to see even without explicit calculation that the sign of this energy shift is positive: since the electron charge is spread across a finite volume, the potential is reduced and as a result the binding energy is weaker and the energy of the bound state is higher.

2.4 The hyperfine splitting

The hyperfine splitting represents the last level of degeneracy present in the theory of atomic energy levels. It corresponds to a difference in energy levels caused by the interaction between the magnetic moments of the electron and the nucleus.

The relativistic theory of Dirac states in fact that particles with spin have a magnetic dipole moment caused by the spin itself. In the case of the proton and the electron, these dipole moments can be expressed as [51]

$$\boldsymbol{\mu}_p = \frac{ge}{2m_p} \boldsymbol{s}_p, \quad \boldsymbol{\mu}_e = \frac{e}{m_e} \boldsymbol{s}_e \tag{2.7}$$

where $\boldsymbol{s}$ and g are the particle's spin and g-factor respectively. For the electron's dipole moment, the explicit value $g \approx -2.00$ has been used. Note that $\boldsymbol{\mu}_p$ is much smaller than $\boldsymbol{\mu}_e$ due to the presence of the proton mass in the denominator.

The magnetic dipole caused by the spin generates the magnetic field [51]

$$\boldsymbol{B}(\boldsymbol{r}) = \frac{\mu_0}{4\pi r^3}\left[3\left(\boldsymbol{\mu}\cdot\hat{\boldsymbol{r}}\right)\hat{\boldsymbol{r}} - \boldsymbol{\mu}\right] + \frac{2\mu_0}{3}\boldsymbol{\mu}\delta^3(\boldsymbol{r}) \tag{2.8}$$

In the case of the hydrogen atom, the Hamiltonian describing an electron in the magnetic field defined in Equation 2.8 is

$$H_{HFS} = \frac{\mu_0 g e^2}{8\pi M m_e}\frac{\left[3\left(\boldsymbol{s}_p\cdot\hat{\boldsymbol{r}}\right)\left(\boldsymbol{s}_e\cdot\hat{\boldsymbol{r}}\right) - \boldsymbol{s}_p\cdot\boldsymbol{s}_e\right]}{r^3} + \frac{\mu_0 g e^2}{3 M m_e}\boldsymbol{s}_p\boldsymbol{s}_e\delta^3(\boldsymbol{r}) \tag{2.9}$$

Perturbation theory states that the first order correction to the energy is the expectation value of the perturbative hamiltonian H_{HFS}. In the case of the spherically symmetric ground state, with $n = 1$ and $l = 0$, the first term of Equation 2.9 vanishes [51], leaving only

$$E^{(1)}_{HFS} = \frac{\mu_0 g e^2}{3 M m_e}\langle \boldsymbol{s}_p\cdot\boldsymbol{s}_e\rangle \left|\Psi(0)\right|^2 = \frac{\mu_0 g e^2}{3\pi M m_e \alpha_0^3}\langle \boldsymbol{s}_p\cdot\boldsymbol{s}_e\rangle \tag{2.10}$$

where α_0 represents the Bohr radius calculated using the reduced mass of the proton-electron system.

The scalar product between the spins is equal to

$$\boldsymbol{s}_p\cdot\boldsymbol{s}_e = \frac{1}{2}\left(S^2 - s_p^2 - s_e^2\right) \tag{2.11}$$

where S^2 is the squared total spin operator, with $\boldsymbol{S} = \boldsymbol{s}_e + \boldsymbol{s}_p$. The electron and the proton have both spin $\frac{1}{2}$, therefore their squared eigenvalues are

$$s_e^2 = s_p^2 = \frac{1}{2}\left(1 + \frac{1}{2}\right)\hbar^2 = \frac{3}{4}\hbar^2 \tag{2.12}$$

It can be seen that the spin-spin coupling breaks the degeneracy between the singlet and the triplet states. The singlet state, in fact, is related to anti-parallel spins with a total squared spin $S^2 = 0$. By inserting this value in Equation 2.12 it's possible to verify that for the singlet state $\langle \boldsymbol{s}_p\cdot\boldsymbol{s}_e\rangle = -\frac{3}{4}\hbar^2$. The triplet state instead is formed by parallel spins with $S^2 = 2\hbar^2$, which corresponds to scalar product equal to $\langle \boldsymbol{s}_p\cdot\boldsymbol{s}_e\rangle = \frac{1}{4}\hbar^2$. It follows that the singlet configuration is lowered while the triplet is heightened, as represented by Figure 2.3.

The resulting energy difference in the specific case of the hydrogen ground state, with $c = 1$ and $\hbar = 1$, is

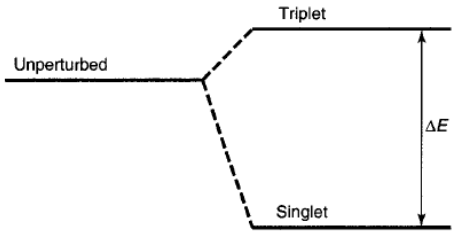

Figure 2.3: Hyperfine splitting between the singlet and triplet state of the hydrogen ground state [51].

$$\Delta E^{(1)}_{HFS} = \frac{g\alpha^4}{3}\frac{m_e^2 M^2}{(m_e + M)^3} \tag{2.13}$$

which corresponds to a frequency of approximately 1418 MHz [51].

Equation 2.13, however, is not accurate enough for high precision measurements and needs to be adjusted through many contributions originating from QED theory. These corrections are once again series expansions depending on the three small dimensionless parameters α, $Z\alpha$ and m_e/M.

A typical factorization of the energy splitting and its corrections is [22, 52, 86]

$$\Delta E_{HFS} = E^F \left(1 + \delta^{Dirac} + \delta^{QED} + \delta^{structure}\right) \tag{2.14}$$

where the uncorrected value E^F, also known as Fermi splitting, is $E^{(1)}_{HFS}$, and the δ terms refer to the different corrections involved. Note that this factorization has only value at a low order of corrections since at higher order the different effects cannot be treated separately.

The first correction δ^{Dirac} denotes the purely relativistic corrections derived directly from the Dirac equation, and consists of a series expansion of even powers of $Z\alpha$ [86]:

$$\delta^{Dirac} = \frac{3}{2}(Z\alpha)^2 + \frac{17}{8}(Z\alpha)^4 + \dots \tag{2.15}$$

The factor δ^{QED} contains the deviations from the hydrogen hyperfine splitting caused by QED effects alone. The main contribution to the factor δ^{QED} is given by the anomalous magnetic moment of the electron a_e that arises from the electron self-energy (see Figure 2.2 (a)). Higher order terms depend instead on the fine structure constant α. Up to terms of the order of α^3, δ^{QED} is equal to [22, 52]

$$\delta^{QED} = a_e + \frac{3}{2}\alpha^2 + \alpha^2\left(\ln 2 - \frac{5}{2}\right) - \frac{8\alpha^3}{3\pi}\ln\alpha\left(\ln\alpha - \ln 4 + \frac{281}{480}\right) + 18.984\cdot\frac{\alpha^3}{\pi} \tag{2.16}$$

The structure corrections term $\delta^{structure}$ is the sum of multiple contributions deriving from QED and from the internal structure of the proton itself. In order to separate the different contributions, the structure corrections are often factorized as [22, 86]

$$\delta^{structure} = \delta^{pol} + \delta^{recoil} + \delta^{hvp} + \delta^{weak} + \delta^{ps} \tag{2.17}$$

The terms in Equation 2.17 refer respectively to contributions caused by proton polarizability, recoil and radiative-recoil, hadronic vacuum polarization, weak interaction and proton finite size. Polarizability, recoil and radiative-recoil corrections have already been introduced in Section 2.2 and 2.3. For more details on the specific case of hyperfine splitting, see [47].

The last factor δ^{ps} is related to the finite size of the proton and takes the form [86]

$$\delta^{ps} = 1.0154\,(2) \cdot \delta^{Z} + 1.4 \cdot 10^{-8} \tag{2.18}$$

where δ^{Z} is the non-relativistic limit of δ^{ps} itself

$$\delta^{Z} = -2Z\alpha m_r r_Z \tag{2.19}$$

The term r_Z in Equation 2.19 is the Zemach radius, ie is the first moment of the convolution of the proton charge and magnetic moment distributions [52, 86]:

$$r_Z = \int d^3\boldsymbol{r} d^3\boldsymbol{r}' \rho_E\left(\boldsymbol{r}\right) \rho_M\left(\boldsymbol{r}'\right) \left|\boldsymbol{r} - \boldsymbol{r}'\right| = -\frac{4}{\pi} \int_0^\infty \frac{dQ}{Q^2} \left[\frac{G_M\left(Q^2\right) G_E\left(Q^2\right)}{\mu_p} - 1\right] \tag{2.20}$$

The value of each correction to the hyperfine splitting, from highest to lowest in magnitude, are reported in Table 2.2. The Fermi splitting and the theoretical and experimental values of the hyperfine splitting itself are also reported.

Term	Value (MHz)
δ^{QED}	0.001 056 210(1)
δ^{Dirac}	0.000 079 88
δ^{ps}	−0.000 040 11(61)
δ^{recoil}	0.000 005 97(6)
δ^{pol}	0.000 001 4(6)
δ^{weak}	0.000 000 06
δ^{hvp}	0.000 000 01
E^F (MHz)	1 418.840 08(2)
$\Delta E^{HFS(th)}$	1 420.405 7(18)
$\Delta E^{HFS(exp)}$	1 420.405 751 767(1)

Table 2.2: Values of the hyperfine splitting and of its corrections ([86] and references therein).

2.5 Lamb shift in muonic hydrogen

Light muonic atoms, and in particular muonic hydrogen, have three special main features compared to their corresponding electronic atoms which are caused by the higher mass of the muon substituting the electron. First of all, the one-loop electron-positron vacuum polarization contribution, eVP for short, is greatly enhanced and becomes the main contribution to the Lamb shift. Second, the leading proton size contribution becomes so relevant that it constitutes the second largest correction to the Lamb shift after the eVP.

The reason behind the enhanced contribution of eVPs may be explained qualitatively by means of the distances at play inside the muonic and electronic hydrogen atoms. The characteristic distance at which the Coulomb potential is distorted by the polarization insertion is determined by the Compton length $r_C = 1/m_e$ [47]. Since the average distance between the atomic electron and the Coulomb source $r_{at} = 1/(m_e Z\alpha)$ is about 137 times greater than r_C, it follows that the electron is well outside the region of strongly distorted Coulomb potential.

The case for muonic hydrogen is completely different: the average radius of the muonic orbit is in fact $r_{at}1/(m_\mu Z\alpha)$, and its ratio with the Compton length is $r_{at}/r_C = m_e/(m_\mu Z\alpha) \sim 0.7$. In other words, in the μp system these two distances are of the same order of magnitude. This means that the muon spends a significant part of its life inside a region where the Coulomb potential is greatly distorted. Qualitatively speaking, one could say that the muons enter directly inside the screening polarization cloud of the Coulomb center and sees a larger unscreened charge compared to its electronic counterpart [47]. As a result the binding energy becomes stronger and the $2S_{1/2}$-level becomes lower than the $2P_{1/2}$-level, an opposite order compared to the one of the electronic hydrogen energy levels. The 2S and 2P levels for the μp atom are shown in Figure 2.4.

The reason behind the higher proton size contribution in muonic hydrogen may also be understood qualitatively: as can be seen in Equation 2.6, the leading correction to the Lamb shift caused by the finiteness of the proton size is proportional to $m_r^3\langle r^2\rangle$, where $m_r \approx 186 \cdot m_e$ is the reduced mass of the μp system. It follows then that the higher mass of the muon produces an increase in the contribution.

Other important contributions to the Lamb shift are given by QED loops [20]: the third highest correction is caused by two-loop eVP diagrams, while the fourth highest one is given by the sum of the muon one-loop self-energy with the one-loop muon-antimuon vacuum polarization, or μVP for short.

The values of the radius-independent corrections are reported in Table 2.3. Table 2.4 contains instead the contributions to the Lamb shift in muonic hydrogen that depend on the proton structure. The dependence on the factor $\langle r_E^2\rangle$ has been explicitly reported. The two-photon exchange contribution corrected for the finite size has been factored in Table 2.4 into its elastic and inelastic part. The elastic part refers to the case where the intermediate virtual photon remains on-shell, while the inelastic part refers to the case where the virtual photon is instead off-shell.

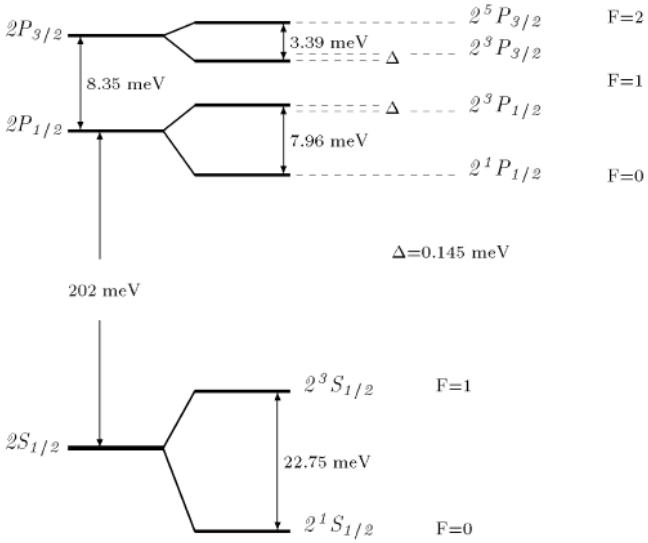

Figure 2.4: Muonic hydrogen energy levels [47].

Corrections	Values [meV]
Relativistic one-loop eVP	205.02821
Two-loop eVP	1.50810
Muon self-energy and μVP	-0.66761
Sum	206.03339(109)

Table 2.3: Radius-independent contributions to the Lamb shift in muonic hydrogen ([20] and references therein). The sum reported here is obtained by considering also higher order corrections.

The total Lamb shift of muonic hydrogen predicted by theory, obtained by summing all terms in Table 2.3 and Table 2.4, is therefore [20]

$$\Delta E_L^{th} = 206.0668(25) - 5.2275(10)\langle r_E^2 \rangle \text{ meV} \tag{2.21}$$

2.6 Hyperfine splitting in muonic hydrogen

The higher mass of the muon compared to that of the electron causes a change also in the Fermi energy and in the leading contributions to the hyperfine splitting.

By applying perturbation theory it's possible to prove that at the lowest level the energy of the hyperfine splitting for the symmetric nS states can be expressed as [20]

Corrections	Values [meV]
One-photon exchange (OPE)	$-5.1994\langle r_E^2\rangle$
Rad. correction to OPE	$-0.0275\langle r_E^2\rangle$
Two-photon exchange (TPE)	0.0332(20)
Rad. correction to elastic part of TPE	$-0.00062\langle r_E^2\rangle$
Rad. correction to inelastic part of TPE	0.00018
Higher order contributions	0.00001(10)

Table 2.4: Main factors contributing to the finite proton size correction to the Lamb shift ([20] and references therein). The proton charge radius $\langle r_E^2\rangle$ is expressed in fm^2.

$$E_{HFS}^{(1)} = \frac{4\left(Z\alpha\right)^4 m_r^3}{3n^3 m_\mu m_p}\left(1+\kappa\right)\left(1+a_\mu\right)\frac{1}{2}\left[F\left(F+1\right)-\frac{3}{2}\right] = E_n^F\frac{1}{2}\left[F\left(F+1\right)-\frac{3}{2}\right] \tag{2.22}$$

where E_n^F is the Fermi energy, F is the total angular momentum and κ and a_μ are the proton and muon anomalous magnetic moments respectively.

Since the structure dependent corrections scale as the reduced mass of the μp system, they become more relevant in muonic hydrogen. The highest term of this type of corrections is caused by finite size effects, and in the non-relativistic limit can be expressed as [20]

$$\Delta E_{fs} = -E_n^F \cdot 2\left(Z\alpha\right) m_r r_Z \tag{2.23}$$

where r_Z is the Zemach radius defined in Equation 2.20.

Similar to the situation for the Lamb shift in muonic hydrogen, in the calculation of the proton polarizability the two-loop contributions cannot be neglected, both in their elastic and inelastic part. This proton polarizability term is the one with the greatest uncertainty [20].

Other relevant factors for the calculation of the hyperfine splitting are radiative corrections and recoil corrections. The former are related to the distortion of the wave functions caused by the potentials at play in the μp system. The latter are determined instead by the two-photon exchange and are of the order of $(Z\alpha)(m/M)E_F^*$, where E_F^* is the Fermi energy calculated without the contribution of the muon anomalous magnetic moment [20].

The last corrections needed for a high precision calculation of the hyperfine splitting in muonic hydrogen are the ones that take into account the effects of eVP in one and two-photon exchange, as well as the effects of the muon self-energy.

Contribution	Values [meV]
Fermi energy	22.807995
Finite size	$-0.16034\ r_Z$
All-order eVP correction	0.07437
Recoil	0.02123
Proton polarizability	0.00801(260)
μVP	0.00091
Hadron VP	0.00060(10)
Weak interaction	0.00027

Table 2.5: Contributions to the 2S hyperfine splitting in muonic hydrogen ([20] and references therein). The values are expressed in meV, the Zemach radius r_Z in fm.

Table 2.5 lists the main contributions to ΔE^{th}_{HFS} in the specific case of the 2S state, whose role will be particularly important in the next chapter.

The sum of all terms in Table 2.5, plus other higher order terms, leads to [20]

$$\Delta E^{th}_{HFS} = 22.9843(30) - 0.1621(10) r_Z \text{ meV} \tag{2.24}$$

Chapter 3

The proton radius puzzle

For a long time all experiments aimed at measuring the radius of the proton produced compatible results independently of the method used in the experiment. In 2010 however a new procedure employed by Pohl *et al.* lead to an unexpected smaller value of the proton radius incompatible with previous results [75]. This new value was in fact both 4.9σ away from the 2006 CODATA proposed value [68] and 4.6 times more precise.

Further experiments confirmed this discrepancy and actually increased the distance from previous results up to 7σ [21], thus marking the beginning of what is now known as the *proton radius puzzle*. The term was chosen to emphasize the fact that this discrepancy is not predicted by the Standard Model.

This incompatibility implies one of two possibilities: either there is a new phenomenon at work that escapes the reach of the known physics, or the discrepancy was caused by unconsidered theoretical and instrumental errors in the experimental procedure.

The FAMU experiment is the proposed solution to the proton radius puzzle: as will be described in greater detail in Chapter 4, its aim is to measure with high precision the Zemach radius in order to either confirm or deny the new proton radius value.

3.1 The beginning of the puzzle: the experiment of 2010

The experiment that started it all introduced a new way of measuring the proton radius: in order to increase the accuracy, instead of employing the proton-electron scattering it was decided to extract the value of the proton radius from a high precision measurement of the Lamb shift in muonic hydrogen [75].

The muonic hydrogen was chosen instead of the ordinary hydrogen due to the fact that the muon is about 200 times heavier than the electron, therefore the Bohr radius is 200 times smaller and the effects of the finite size of the proton on the muonic S states are enhanced.

The shifting of the P states is smaller compared to the one felt by the S energy levels due to the properties of the muon's waveform.

Pohl *et al.* predicted a value of the energy difference between the $2S_{1/2}^{F=1} - 2P_{3/2}^{F=2}$ states equal to [75]

$$\Delta E = 209.9779\,(49) - 5.2262\ r_p^2 + 0.0347\ r_p^3\ \text{meV} \tag{3.1}$$

where $r_p = \sqrt{\langle r_p^2 \rangle}$ is expressed in fm.

The first term of Equation 3.1 is dominated by the vacuum polarization, shown in Figure 2.2 (b). As a consequence, the $2S$ states have a higher binding energy than the $2P$ ones. Its uncertainty of 0.0049 meV is given mainly by the proton polarizability term of 0.015(4) meV.

The second and third term represent finite size corrections: together they amount to $\sim 2\%$ of ΔE, which is two orders of magnitude greater than the corresponding contribution for ordinary hydrogen. This increased relevance of the proton size corrections is what justifies a better determination of the proton radius.

The energy difference between $2S_{1/2}^{F=1} - 2P_{3/2}^{F=2}$ states has been measured through pulsed laser spectroscopy at wavelengths around 6.01 μm. This particular transition was chosen between all six allowed optical $2S - 2P$ transitions as it guaranteed the largest signal [75]. Figure 3.5 shows in detail the 2S and 2P muonic hydrogen energy levels, with the $2\mathrm{S}_{1/2}^{F=1} - 2\mathrm{P}_{3/2}^{F=2}$ transition in green.

The experiment was performed at the $\pi E5$ beam-line of the proton accelerator at the Paul Scherrer Institute (PSI) in Switzerland. The experimental apparatus was composed by a cyclotron trap, a muon extraction channel and a 5 T solenoid.

The cyclotron trap consisted of a magnetic bottle generated by two 4 T ring coils, with $B = 2$ T in the center of the trap. The muons produced inside the trap were decelerated and sent to the muon extraction channel, composed by a toroidal momentum filter with a magnetic field $B = 0.15$T. Said filter favoured muons with an energy of ~ 20 keV and separated them from background radiation.

From the muon extraction channel, the beam reached the bore hole of a 5 T superconducting magnet. This high magnetic field was chosen in order to guarantee a minimal radial size of the beam, thus decreasing the target volume that needed to be illuminated by the laser.

A representation of the solenoid and of the components that it contained is shown in Figure 3.1: the muon beam passed first through two stacks of ultra-thin carbon foils, with an area density $d = 4\ \mu\text{g/cm}^{-2}$ kept at a high electric potential. These stacks acted as muon detectors and further slowed down the muons to about $3 - 6$ keV.

While passing through the stacks the muons released electrons (in red) which were separated from the beam by a $\boldsymbol{E} \times \boldsymbol{B}$ separator field. These electrons were then detected by plastic scintillators coupled with photomultiplier tubes and their signal provided the trigger for the laser and the data acquisition system.

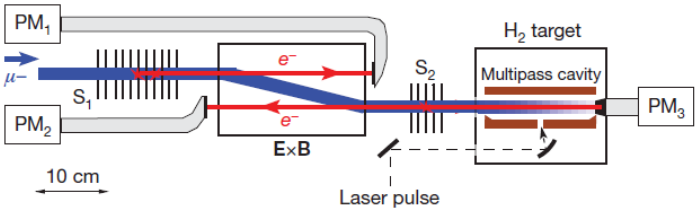

Figure 3.1: Scheme of the components inside the solenoid at the end of the muon beam line [75]. The muon beam is depicted in blue, the released electrons in red. The elements $S_{1,2}$ represent the stacks of carbon foils.

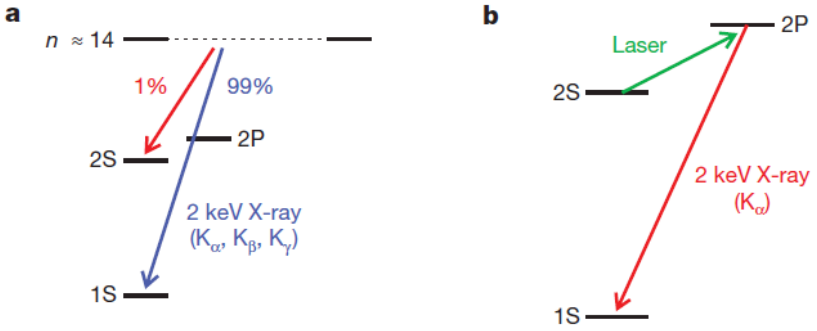

Figure 3.2: 1S, 2S and 2P muonic hydrogen energy levels and X-rays emitted in the transitions between them [75]. (a) About $\sim 99\%$ of the μp atoms de-excite to the 1S ground state with the emission of K-series X-rays, while the remaining 1% go into the metastable 2S state. (b) The μp(2S) atoms are illuminated by a laser pulse. When the laser is on resonance, the atoms reach the 2P state and quickly de-excite to the ground state by emitting 1.9 keV K_α X-rays.

The muon beam reached instead a target with length of 20 cm along the beam axis. Said target contained 1.0 hPa of H_2 gas kept at a temperature of 20 °C. Inside the target, the muons stopped completely and formed highly excited μp atoms.

Typically, muonic atoms that are produced through this procedure start from a highly excited state, which usually consists of the $n \sim 14$ energy level. This particular level is favoured since the optimal overlap of the bound muon and electron wave functions occurs approximately at $n \approx \sqrt{m_r(\mu p)/m_r(ep)} \approx 14$ [59].

The muonic atom produced during the experiment thus underwent a series of transitions, collectively called *muon cascade*, and quickly de-excited to the 1S ground state by emitting prompt K-series X-rays. Of all muonic atoms, only $\sim 1\%$ went to the long-lived 2S state instead [59]. This is shown in Figure 3.2 (a).

A short laser pulse with tunable wavelength $\lambda \in [6.00, 6.03]$ μm entered the mirror cavity surrounding the target about 0.9μs after the muons stopped. 2S$\rightarrow$ 2P transitions were induced on resonance. These transitions were then followed by 2P$\rightarrow$ 1S de-excitation with the emission of a 1.9 keV K_α X-ray, as may be seen in Figure 3.2 (b). The laser had

a fluence of 6 mJ cm^{-2}, which resulted in a 2S-2P transition probability on resonance of $\sim 30\%$.

The K_α X-rays were recorded by two face-to-face rows of 10 large area avalanche photodiodes [62], or LAAPDs for short, located above and below the target. The LAAPDs had an active area of 14×14 mm^2 and provided an effective solid angle coverage of 20% of 4π. Their time and energy resolution for the specific case of 1.9 keV X-rays were respectively 35 ns and 25% FWHM.

The pressure of the gas inside the target, 1 hPa, had been chosen as a tradeoff between three factors: the maximization of the lifetime of the μp $2S$ state τ_{2S}, that was $\approx 1\mu$s in this setup, the minimization of the muon stop volume and the minimization of the laser pulse energy needed to induce the 2S-2P transitions.

The resonance curve of the transitions had been extrapolated by measuring with different laser wavelengths the number of K_α X-rays that occurred in time-coincidence with the laser pulse. The measurement times spanned between 3 and 13 h per laser wavelength.

Figure 3.3 contains the resulting X-ray time spectra. The large prompt peak contains the K_α, K_β and K_γ X-rays produced by the de-excitation of the $\sim 99\%$ muons that didn't go to the long-lived 2S state and didn't form metastable μp atoms. This peak has been used to normalize the data for each laser wavelength to the number of μp atoms formed [75].

The time window $t \in [0.887,\ 0.962]$ μs corresponds to the 75 ns long laser time window in which the K_α X-rays emitted during the 2P$\rightarrow$ 1S de-excitation were expected. More precisely, 75 ns corresponds to the confinement time of the laser light within the multipass mirror cavity that surrounded the target.

A rate of 7 events per hour has been recorded inside this time window when on resonance. The background of ~ 1 event per hour originates mainly from falsely identified muon-decay electrons and other effects related to the delayed transfer of the muon to the target walls [75].

Figure 3.4 shows the measured 2S$\rightarrow$ 2P resonance curve. The curve has been obtained by plotting the number of K_α events recorded inside the 75 ns long laser time window as a function of the laser frequency, and has been normalized to the total number of events inside the prompt peak.

The total number of events measured in the resonance is 550, 155 of which were expected to be background events. The fit to the data is a Lorentzian resonance line on top of a flat background. The four parameters of the fit, that is the Lorentzian amplitude, position, width and the background amplitude, were let to vary freely. The statistics related to each laser wavelength were accounted for through a maximum likelihood fit performed using CERN's ROOT analysis tool. The statistical uncertainties obtained by Pohl *et al.* were 1σ confidence intervals.

The position of the resonance curve centroid obtained with this procedure was 49881.88(70) GHz with a width of 18.0(2.2) GHz, where the given uncertainties are the

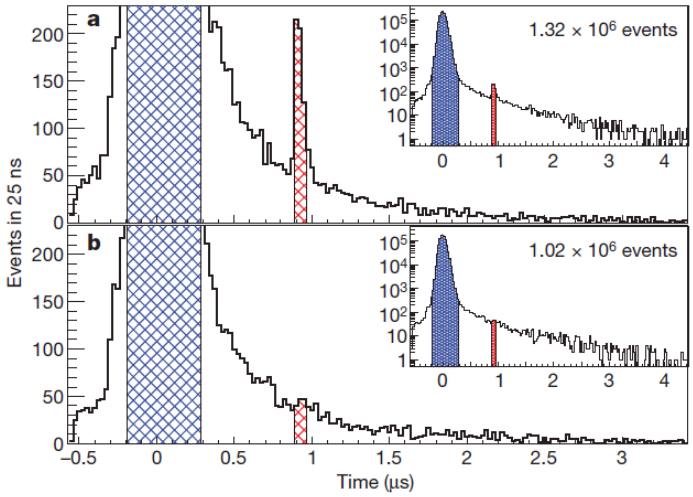

Figure 3.3: Summed X-ray time spectra, with inset plots showing the complete data and the total number of events [75]. The spectra were recorded on resonance (a) and off resonance (b). The prompt X-rays of the K-series are marked in blue, while the time window $t \in [0.887,\ 0.962]$ μs in which the 1.9 keV X-rays were expected is marked in red.

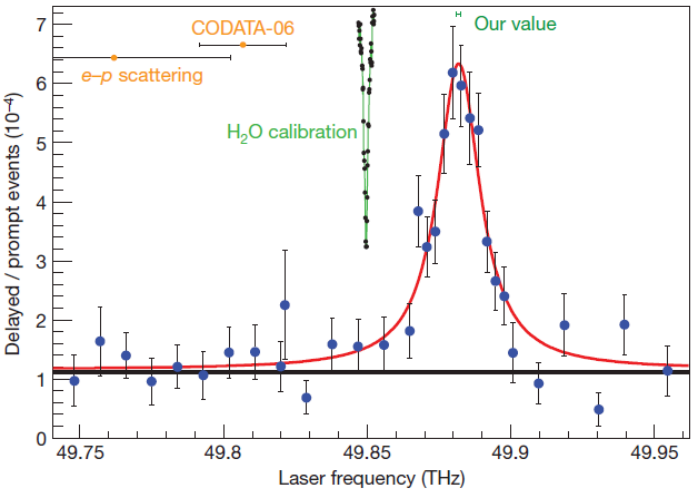

Figure 3.4: Resonance curve obtained by plotting the number of K_α events recorded inside the 75 ns long laser time window as a function of the laser frequency [75]. The curve has been normalized to the total number of events inside the prompt peak. The red fit line is a Lorentzian on top of a flat background, and gives a $\chi^2 = 28.1$ for 28 dofs. The yellow data points on the top left represent the predictions for the line position using the proton radius provided by CODATA [68] and derived from electron scattering. The error bars are the $\pm 1\sigma$ regions. The green line represents the calibration measurements.

1σ statistical uncertainties [75]. The Lorentzian fit performed on the curve resulted in a $\chi^2 = 28.1$ for 28 degrees of freedom. The fit of a flat line assuming no resonance gives $\chi^2 = 283$ for 31 dofs, making this resonance line 16σ significant.

The resulting centroid position of the $2S_{1/2}^{F=1} - 2P_{3/2}^{F=2}$ transition is 49881.88(76) GHz, where the increased statistical error comes from systematic uncertainties related mainly to the calibration procedure [75]. This frequency corresponds to an energy

$$\Delta E = 206.2949(32) \text{ meV} \tag{3.2}$$

which, in combination to Equation 3.1, leads to a value of the proton charge radius of

$$r_E = 0.84184(36)(56) \text{ fm} \tag{3.3}$$

The first uncertainty of r_E comes from the 0.76 GHz of the resonance frequency, while the second one originates from the uncertainty of the first term in Equation 3.1.

The new value obtained by Pohl *et al.* is 10 times more precise and 5σ smaller than the world average up until 2010. It is also 26 times more precise but 3.1σ smaller than the hydrogen-independent value extracted from the electron-proton scattering data available at the time.

The conclusion drawn by Pohl *et al.* was that either the calculations of the QED effects in ordinary or muonic hydrogen were insufficient, thus implying that their new value of the proton radius was incorrect, or their value was indeed correct and the Rydberg constant itself had to be shifted instead to a new value $R_\infty = 10973731.568160(16)$ m^{-1}, a value that was 4.9σ away from the one recommended by CODATA [68] but 4.6 times more precise.

3.2 The consolidation of the proton radius puzzle

This inconsistency in the value of the proton radius was later confirmed by another experiment by Antognini *et al.* in 2013 [21]. The experiment was performed once again at the Paul Scherrer Institute with the same apparatus described in Section 3.1. In order to verify the conclusions of the 2010 article, in addition to the $2S_{1/2}^{F=1} - 2P_{3/2}^{F=2}$ transition frequency, the $2S_{1/2}^{F=0} - 2P_{3/2}^{F=1}$ transition was also measured (see Figure 3.5).

The $2S_{1/2}^{F=0} - 2P_{3/2}^{F=1}$ transition starts from the singlet state, has frequency $\nu_s = \nu\left(2S_{1/2}^{F=0} - 2P_{3/2}^{F=1}\right)$ and wavelength $\lambda_s \cong 5.5$ μm, while the other starts from the triplet state, has frequency $\nu_t = \nu\left(2S_{1/2}^{F=1} - 2P_{3/2}^{F=2}\right)$ and has wavelength $\lambda_t \cong 6.0$ μm.

The two frequencies had been measured by counting the number of K_α X-rays emitted during the de-excitation of the 2P states and by plotting them as a function of the laser frequency [21]. A new data acquisition and analysis procedure had been devised in order to improve the accuracy of the experiment's result.

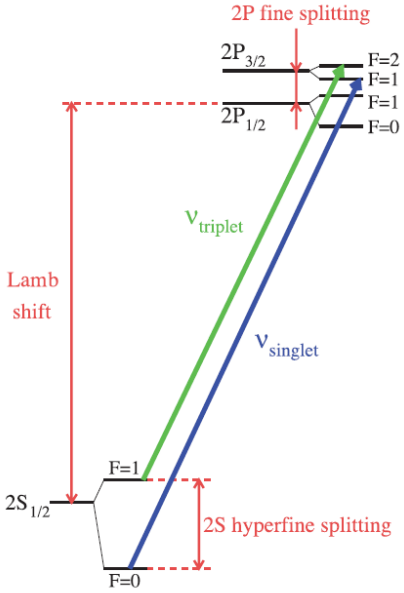

Figure 3.5: 2S and 2P energy levels [21]. The green and blue lines correspond to the $2S_{1/2}^{F=1} - 2P_{3/2}^{F=2}$ and $2S_{1/2}^{F=0} - 2P_{3/2}^{F=1}$ respectively. The Lamb shift, 2S hyperfine splitting, and 2P fine and hyperfine splitting are also present.

On average, $\approx 580\ \mu/s$ were expected to enter the hydrogen target. Of these muons, about $330\ \mu/s$ were detected by two muon entrance detectors. Each muon recorded by both detectors started the data acquisition system and triggered the laser pulse.

For each laser pulse shot, a dead-time of 2 ms was imposed on the laser system to ensure stable laser operation. Because of this dead-time, of the $330\ \mu/s$ muons that affected both detectors only $200\ \mu/s$ managed to produce a laser trigger. The events corresponding to these muons were called "laser-on" events [21]. The remaining $130\ \mu/s$ activated the acquisition system too, but produced no laser triggers. For this reason they were called "laser-off" events.

Each event opened a 12 μs long "event gate" during which the X-rays were recorded by the LAAPDs. The electrons produced by the muon decay were instead recorded by the plastic scintillators. It's important to notice that μ-decay electrons could generate signals also in the LAAPDs.

In order to reduce the background in the X-ray spectra, not all X-rays were considered in the data analysis: the requirement for the acceptance of the events was that a muonic X-ray must be followed by a μ-decay electron within a specific time window, called "delayed electron time window". This condition alone helped reducing the background by about an order of magnitude [21].

Another refinement of the data analysis procedure is related to the decay electrons. These electrons have been used to classify the recorded X-rays into two different class

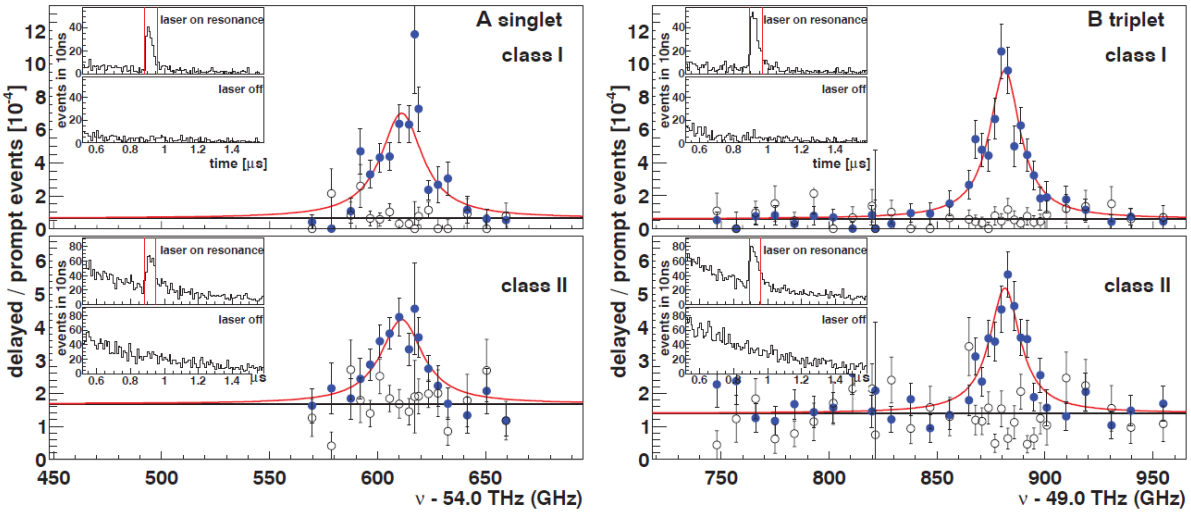

Figure 3.6: Muonic hydrogen resonance curves for singlet and triplet transitions [21]. For each frequency, two resonance curves were produced using data from Class I and II separately. Full dots and blank dots mark laser-on and laser-off events respectively. The error bars indicate the standard error. The insets show the time spectra of the K_α X-rays and the laser time window.

depending on two factors: the number of detectors crossed and the time difference between the X-ray and the electron.

It has been noticed in fact that it was possible for some decay electrons to cross more than one detector, be it plastic scintillator or LAAPD. These multi-hit electrons generated a particularly clean data set with a lower background compared to that of single-hit electrons: spurious detector signals could in fact create the signature of single-hit electrons and could therefore generate a higher background in the spectra. The amount of spurious signals was found to be related to the amount of energy deposited by the decay electron in the LAAPD or plastic scintillator: the larger the energy released and the signal recorded, the cleaner the data set.

The background was also influenced by the time difference between X-ray and electron signal. For this reason, by using the laser-off data set, the delayed electron time window has been optimized individually for each of the various electron-like signals.

These two different factors were what determined the class of an X-ray: "Class I" contained X-rays that were followed by a decay electron that met at least one of the two criteria for a clean electron identification, while "Class II" contained the remaining X-rays of the data set. Class I held the majority of the recorded events, but had a significantly smaller signal to noise ratio [21].

The resonance curve for both singlet and triplet states has been extrapolated from the data considering Class I and II signals separately. Figure 3.6 shows the obtained curves.

The insets report the corresponding time spectra in the region of the laser-induced events. The time of an event was determined by the detection time of the K_α X-ray after

the trigger given by the muon entrance detectors.

The curves were obtained by plotting the number of events recorded within the laser time window, divided by the number of prompt X-rays (see Figure 3.2 (a)), as a function of the laser frequency. For each laser frequency the total recording time spanned between 6 and 13 hours. The background of the resonance curves corresponds to ≈ 1 event per hour, while the peak of the curve corresponds to ≈ 6 events per hour [21]. In order to verify the flatness of the background, the laser-off data set has been plotted too.

The two curves have been fitted simultaneously using six free parameters: the first two were the position and width of the resonance peak, and were shared by both curves. The last four were the signal amplitude and the background amplitude, kept independent for the two spectra. A line shape model based on the equations of the 2S-2P-1S system was used to fit the resonances while taking into account saturations and broadening effects.

In order to avoid systematic shift of the resonance peak, the laser pulse energy of each laser shot was recorded and used in the line shape model. This procedure resulted in corrections of the resonance positions of ≈ 50 MHz.

The resonance positions obtained through this procedure were [21]

$$\nu_s = 54611.16(1.00)^{stat}(30)^{sys} \text{ GHz} \tag{3.4}$$

$$\nu_t = 49881.35(57)^{stat}(30)^{sys} \text{ GHz} \tag{3.5}$$

where "stat" and "sys" denote statistical and systematic uncertainties.

By employing a linear combination of ν_s and ν_t, namely [20]

$$\frac{1}{4}h\nu_s + \frac{3}{4}h\nu_t = \Delta E_L + 8.8123(2) \text{ meV} \tag{3.6}$$

$$h\nu_s - h\nu_t = \Delta E_{HFS} - 3.2480(2) \text{ meV} \tag{3.7}$$

it was possible to obtain a measure of the Lamb shift and of the 2S hyperfine splitting in muonic hydrogen.

The numerical terms in Equation 3.6 and 3.7 include the calculated values of the 2P fine structure, the mixing of the 2P states and the hyperfine splitting of the $2P_{3/2}$ state. Finite size effects are included in ΔE_L and ΔE_{HFS}, but their uncertainties have been neglected due to the fact that the effects of the proton size on the 2P fine and hyperfine structures are smaller than 1×10^{-4} meV.

By using the frequencies ν_s and ν_t in combination with Equation 3.6 and 3.7, Antognini *et al.* obtained the values [20]

$$\Delta E_L^{exp} = 202.3706(23) \text{ meV} \tag{3.8}$$

$$\Delta E_{HFS}^{exp} = 22.8089(51) \text{ meV} \tag{3.9}$$

where the uncertainties are the result of the quadratic sum of the statistical and systematic uncertainties of the transition frequencies.

The comparison between the experimental value of the Lamb shift given in Equation 3.8 and its theoretical expression reported in Equation 2.21 yields [20]

$$r_E = 0.84087(26)^{exp}(29)^{th} \text{ fm} = 0.84087(39) \text{ fm} \tag{3.10}$$

This value is compatible with the results of the 2010 experiment (see Equation 3.3), but 1.7 times more precise and at 7σ variance with the 2010 CODATA value [69]. As stated by Antognini *et al.*, this result has also the advantage of being independent from the theoretical prediction of the 2S hyperfine splitting.

By computing the 1S and 2S Lamb shifts in electronic hydrogen using the value of r_E from the muonic hydrogen, the measured 1S-2S transition frequency gives $R_\infty = 3.2898419602495(10)(25) \times 10^{15}$ Hz/c. The first uncertainty comes from the uncertainty of r_E in Equation 3.10, the second is caused by QED effects. This value of R_∞ deviates by -155 kHz/c, that is 6.6σ, from the 2010 CODATA value [69] and is 6 times more accurate.

Chapter 4

The FAMU experiment and its proposal

With the results obtained from the aforementioned experiments the proton radius puzzle has become a topic of international debate in physics. As of today it's still unclear whether the incompatibility between the different r_E values is connected to new physics not covered by the Standard Model or is caused by uncertainties in the experimental procedures. In order to shed light on the true nature of these discrepancies a new international experiment was proposed: the FAMU experiment.

The aim of the FAMU (**F**isica degli **A**tomi **Mu**onici) experiment is to extract the value of the Zemach radius, defined in Equation 2.20, with a relative precision below 1%. The Zemach radius is in fact the main contribution to the proton structure corrections of the energy levels, as well as the main source of uncertainty in high-precision calculation of the proton charge radius. A confirmation of the value obtained with ordinary hydrogen spectroscopy would support the thesis that the discrepancies are caused by unconsidered methodology uncertainties. A new value of r_Z obtained through muonic hydrogen spectroscopy would justify instead the search for new physics [25].

The procedure that will be used in the experiment is shown in Figure 4.1: negative muons are sent inside a target containing hydrogen and oxygen, where they quickly slow down and form highly excited muonic hydrogen atoms. As was stated in Section 3.1, these atoms are formed at the $n \approx 14$ energy level due to the optimal overlapping of the bound muon and electron wave functions.

The formation of the muonic atoms is followed by a series of transitions collectively called muon cascade that brings $\sim 99\%$ of them to the ground state 1S and the remaining 1% to the 2S metastable state [59].

The FAMU experiment procedure focuses on the atoms in the 1S state. Approximately 75% of these atoms are in the triplet state (F = 1) while the remaining 25% are in the singlet state (F = 0). Collisions between muonic hydrogen atoms and H_2 molecules cause the de-excitation of the $\mu p(1S)^{F=1}$ atoms leaving behind only thermalized atoms in the $(1S)^{F=0}$ singlet state. A laser with tunable frequency is then sent inside the target, inducing a series of transition from the singlet state to the triplet state. Collisions with

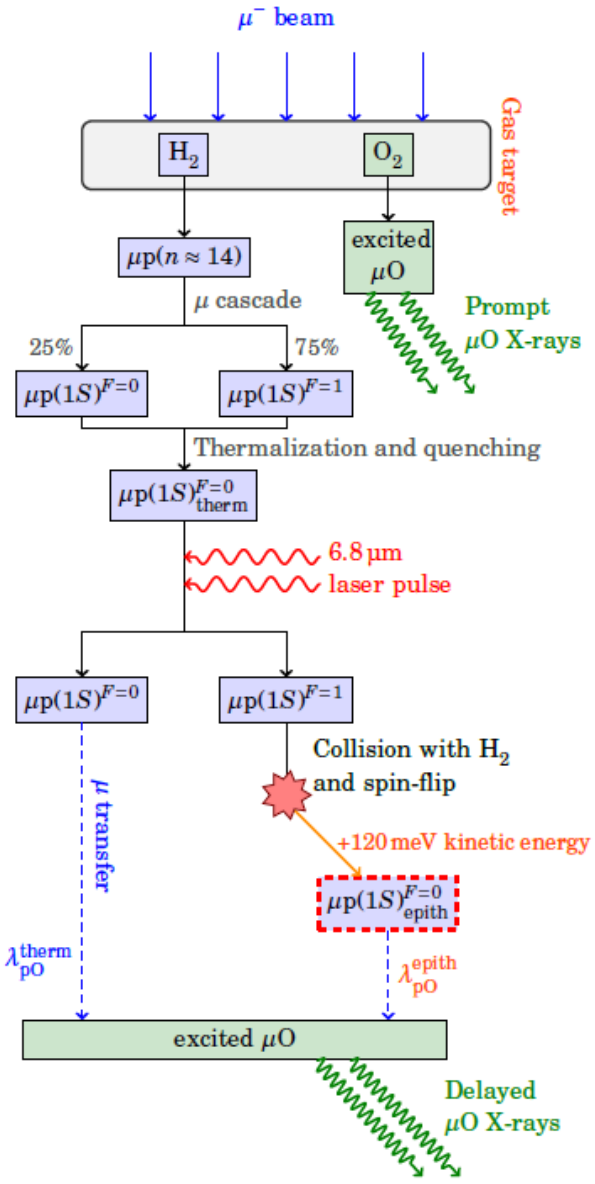

Figure 4.1: Representation of the FAMU experiment procedure [52].

H_2 molecules cause the atoms to once again transition from the triplet state to the singlet state and to convert their transition energy into additional kinetic energy of the μp-H_2 system. At this step the muonic hydrogen atoms gain about 120 meV from the hyperfine transition energy [24, 52].

By performing a scan over the laser frequency near the hyperfine splitting transition frequency and by counting the number of muonic hydrogen atoms with increased kinetic energy it's then possible to obtain a resonance plot and extract from it the value of the 1S hyperfine splitting.

The main obstacle in the development of this methodology consisted precisely into finding a way to count the number of such atoms. The following sections will focus on how this method came to be and on additional details needed to perform the experiment.

4.1 The development of the FAMU experiment methodology

The original idea behind the procedure shown in Figure 4.1 belongs to Bakalov *et al.* [24]. In their article they proposed to put inside the target thin foils of specific heavy materials, like gold, and to observe the transfer of the muons from the μp system to the foils. These atoms would then decay and emit characteristics X-rays. The energy of the 1S hyperfine splitting would thus be measured by observing the temporal distribution of the X-rays as a function of the laser frequency.

This particular approach was deemed inapplicable since it's impossible to embed such a target in a multipass optical cavity capable of amplifying the laser radiation. This requirement is necessary because, as will be shown in Section 4.3, with just the laser alone too few μp $(1S)^{F=0}$ atoms are actually able to jump to the $(1S)^{F=1}$ state and back.

The process proposed in by Bakalov *et al.* was further refined by Adamczak *et al.* [16] into what would later become the FAMU experiment procedure. More precisely, they proposed to measure the number of muon transfer events from muonic hydrogen to another higher-Z gas instead of thin gold foils. In fact, although the theory predicts in general a flat behaviour of the transfer rate at low energies, oxygen is an exception.

Adamczak *et al.* suggested therefore to put inside the target a mixture of H_2+O_2 and to study the time distribution of the $\mu^- p + O \rightarrow \mu^- O + p$ characteristic X-rays. An increase in the number of X-rays would mean an increase of the transfer rate, which could be used as a signature of the laser stimulated transitions between the singlet and triplet states of the muonic hydrogen in the ground state.

Through a Monte Carlo simulation, whose results are shown in Figure 4.2, they showed that the increase of the number of events is statistically significant.

New studies [70, 88] confirmed that the hydrogen to oxygen muon transfer rate exhibits a peak around intermediate energies of about ~ 100 eV. Other researches showed that

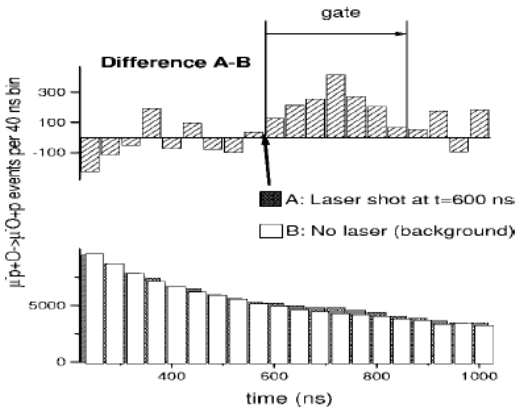

Figure 4.2: Time distribution of the hydrogen to oxygen muon transfer events at 300 K, 8 atm, 0.05% oxygen concentration for 500000 muons [16]. Curve B represents the background case, Curve A describes the effects of a 80 ns laser pulse shot 600 ns after the μp atoms have reached the ground state.

argon and neon could also exhibit a peak in the muon transfer rate at specific energies of the muonic hydrogen atoms [54, 55].

The main point is that adding a small concentration of a specific contaminating gas inside the H_2 target makes it possible to derive the number of accelerated μp atoms from the increasing number of characteristic X-rays emitted by the gas itself.

4.2 Thermalization and depolarization of muonic hydrogen atoms

Part of the energy released during the muon cascade is transformed into kinetic energy of the muonic atoms. As a consequence, the energy distribution of the atoms in the ground 1S state spreads over a broad interval up to the keV range. These muonic atoms with higher kinetic energy have then the task of transferring their muons to the higher-Z gases in the target.

A computational study was performed in 2015 by Bakalov *et al.* [25] in order to study the energy dependence of the muon transfer rate from hydrogen to higher-Z gases and to select the optimal composition and physical parameters of the target.

They first investigated how the muonic atoms de-excite from the $1S^{F=1}$ state, and concluded that thermalization and depolarization are the main processes of de-excitation. These two processes take place respectively through elastic and spin-flip scattering of the μp with H_2 molecules.

A set of Monte Carlo simulations starting from muonic atoms in statistically populated singlet and triplet states showed that thermalization and depolarization depend only on hydrogen concentration and temperature [25]. The dependence on the temperature

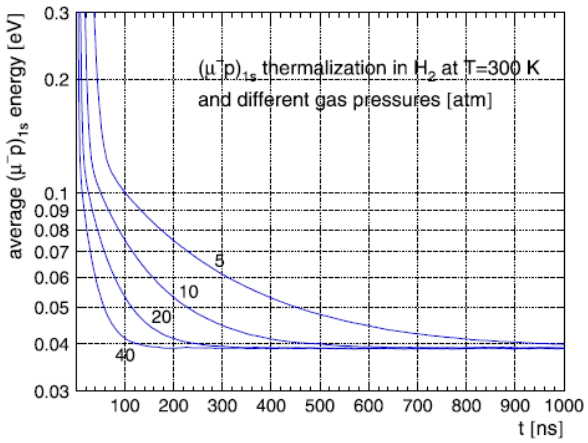

Figure 4.3: Average energy of the muonic hydrogen atoms in the 1S state versus time t at fixed temperature T for pressures $P = 5$, 10, 20 and 40 atm [25].

comes from the fact that the molecular cross sections for the μp+H_2 scattering, which have been calculated in [13, 14], depend on the temperature themselves.

The following graphs, obtained by plotting the average energy of the μp 1S state as a function of time, contain the results of the Monte Carlo simulations.

Figure 4.3 shows the thermalization process in pure hydrogen at fixed temperatures for relevant pressures. In this first step, an increase in pressure meant an increase in density, and vice versa. The same applied to a decrease in value. As can be seen, the time needed for the average energy to reach a state of equilibrium is approximately inversely proportional to the pressure, and therefore to the density. This conclusion is confirmed by Figure 4.4, where the average energy was plotted at constant pressure for a set of temperature values and their corresponding hydrogen density values. The density ϕ is expressed in the units of liquid hydrogen density. As ϕ increases, the time needed to reach equilibrium diminishes.

The dependence of thermalization on the temperature, although present, has a smaller effect on the de-excitation of the atoms: Figure 4.5 in fact shows that for fixed density all atoms thermalize after $t \sim 150$ ns for a wide range of temperatures.

The muonic hydrogen depolarization exhibits a behaviour that is similar to the one discussed above, but much faster. As shown in Figure 4.6, at the same conditions selected in Figure 4.3 the depletion of the triplet states through depolarization is an order of magnitude faster than the thermalization process.

By summarizing the results of these Monte Carlo simulations, it was concluded that with good accuracy the muonic hydrogen atoms are completely thermalized and depolarized after t_0 nanoseconds, where t_0 can be roughly estimated as [25]

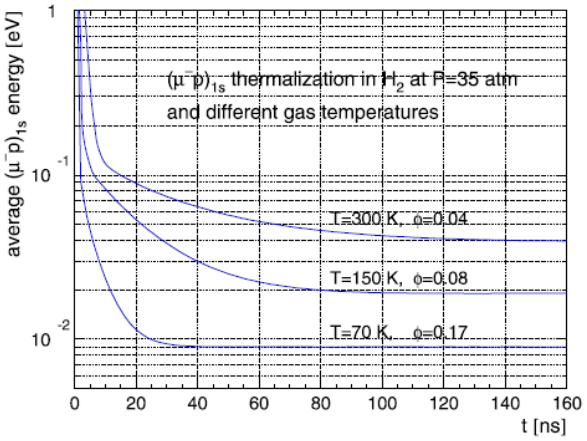

Figure 4.4: Average energy of the muonic hydrogen atoms in the 1S state versus time t at fixed pressure P for a set of temperatures T [25]. The density ϕ of the H_2 gas is expressed in LHD.

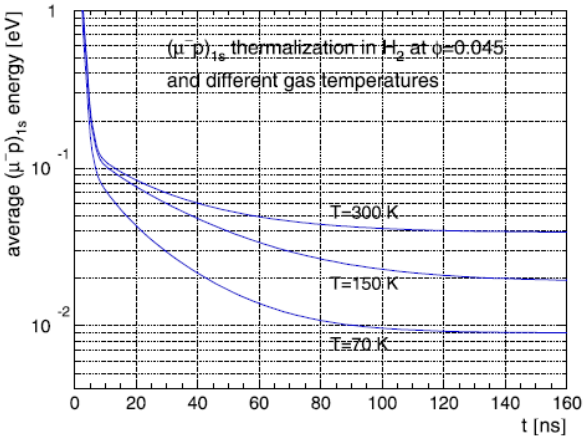

Figure 4.5: Average energy of the muonic hydrogen atoms in the 1S state versus time t at fixed density $\phi = 0.45$ in LHD units for a set of temperatures T [25].

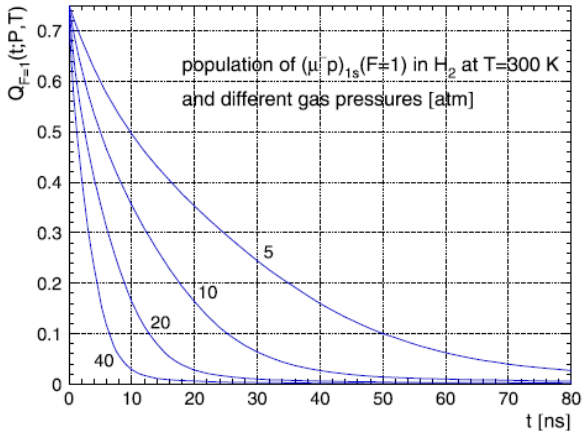

Figure 4.6: Time evolution of the population $Q_{F=1}$ of the μp atoms in the $1S^{F=1}$ at fixed temperature for a set of pressures [25].

$$t_0\,[\text{ns}] \sim 20 \times \frac{T\,[\text{K}]}{P\,[\text{atm}]} \tag{4.1}$$

The last part of the study performed by Bakalov *et al.* consisted of a new set of Monte Carlo simulations that considered the addition of oxygen to the target. As already mentioned above, and as will be explained in detail in Subsection 4.4.1, oxygen plays a fundamental role in the FAMU experiment. For this reason Bakalov *et al.* deemed necessary examine also how the presence of oxygen inside the target affects the thermalization process and the muon transfer rate.

Figure 4.7 represents the number of μp(1S) atoms in a mixture of hydrogen and oxygen at T= 300 K and P= 35 atm. The curve for $c = 0\%$ acts as an upper limit to the number of muonic hydrogen atoms. In case oxygen is added to the target, in fact, this number significantly decreases as the oxygen concentration increases. If $c \geq 1\%$ the μp atoms disappear through either decay or muon capture well before the thermalization process can take place [25]. Further tests showed that the fraction of muon stops inside the target practically doesn't depend on the oxygen concentration if $c \leq 1\%$.

The optimal oxygen concentration is the one that provides, for a specific number of muon stops in H_2, the maximum number of muon transfer events from thermalized μp to oxygen. The last Monte Carlo simulation was performed in order to obtain an estimate of this concentration. The results of analysis of the hydrogen to oxygen muon transfer rate as a function of c are reported in Figure 4.8. As can be seen, at T= 300 K and P= 35 atm the transfer rate exhibits a peak at specific oxygen concentrations. Since the statistical uncertainty of muon transfer rate measurements is proportional to the inverse square root of the number of transfer events, it follows that careful planning of the right oxygen concentration may lead to a drastic decrease of the aforementioned uncertainty.

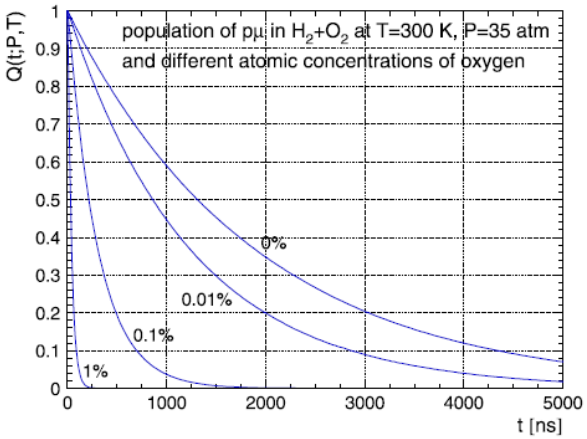

Figure 4.7: Time evolution of the number of μp(1S) atoms in a H_2+O_2 for different oxygen concentration at constant temperature and pressure [25]. The number of μp is normalized to the number of thermalized and depolarized μp at t_0, here for simplicity set at $t_0 = 0$ ns.

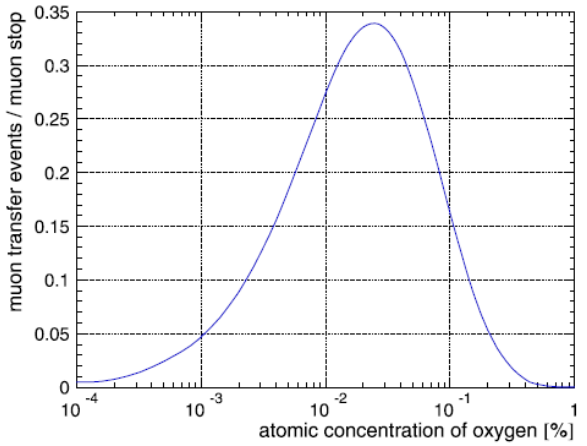

Figure 4.8: Number of muon transfer events from thermalized μp in H_2+O_2 as a function of the oxygen concentration [25]. This number is normalized to the number of thermalized and depolarized muonic hydrogen atoms at $t_0 = 0$. The temperature has been set at $T = 300$ K, while the pressure at $P = 35$ atm.

4.3 Laser power requirements

The laser power requirements were investigated by Adamczak *et al.* in [15]. In order to stimulate transitions from the 1S singlet state to the triplet one, a tunable source of monochromatic radiation in the 6.7 μm wavelength range is needed.

The required power of this source has been estimated by considering the transition matrix that describes the spin-flip transition probability for a muonic hydrogen atom. It's assumed that μp atoms starts in the 1S ground state and are stimulated by an external oscillating magnetic field of frequency ν, $\boldsymbol{B}(t) = \boldsymbol{B}_0 \cos 2\pi\nu t$. If the quantization axis is chosen to be parallel to $\boldsymbol{B}_0$, the transition matrix element can be defined as

$$\begin{aligned}&\left\langle (1S)^{F'=1} \left| -e\hbar \, cos\, 2\pi\nu t \left(\frac{\mu_p}{m_p} \boldsymbol{B}_0 \cdot \boldsymbol{s}_p - \frac{\mu_\mu}{m_\mu} \boldsymbol{B}_0 \cdot \boldsymbol{s}_\mu \right) \right| (1S)^{F=0} \right\rangle \\ &= -\frac{e\hbar}{2} \cos 2\pi\nu t \left(\frac{\mu_p}{m_p} + \frac{\mu_\mu}{m_\mu} \right) |\boldsymbol{B}_0| \end{aligned} \tag{4.2}$$

where m_p, m_μ, $\hbar\boldsymbol{s}_p$ and $\hbar\boldsymbol{s}_\mu$ denote the mass and the spin operator of the proton and the muon [15]. The proton and muon magnetic moments μ_p and μ_μ are in units $e\hbar/(2m_p)$ and $e\hbar/(2m_\mu)$ respectively.

The probability per unit of time dP/dt for the spin-flip transition is then

$$\frac{dP\left(\nu, \nu_0\right)}{dt} = \frac{1}{\hbar^2} \left(\mu_B \left|\boldsymbol{B}_0\right|\right)^2 \left(\frac{m_e}{m_p}\mu_p + \frac{m_e}{m_\mu}\mu_\mu \right)^2 \delta\left(\nu - \nu_0\right) \tag{4.3}$$

where μ_B is the Bohr magneton and ν_0 is the resonance frequency.

The probability distribution ρ_D of ν_0 around the resonance frequency at rest $\bar{\nu}_0 = \Delta E_{HFS}(n=1)/h$ is not a delta function due to the Doppler effect. As a consequence, the probability distribution becomes

$$\rho_D\left(\nu_0\right) = \frac{1}{\sigma_D\sqrt{2\pi}} \exp\left\{ -\frac{\left(\nu_0 - \bar{\nu}_0\right)^2}{2\sigma_D^2} \right\} \quad \text{with} \quad \sigma_D = \bar{\nu}_0 \cdot \sqrt{\frac{kT}{\left(m_p + m_\mu\right) c^2}} \tag{4.4}$$

By taking into account the laser line profile $\rho_L(\nu)$ and its width σ_L, the observable spin-flip probability $d\bar{P}/dt$ can then be expressed as

$$\frac{d\bar{P}}{dt} = \int d\nu_0 \rho_D\left(\nu_0\right) \int d\nu \rho_L\left(\nu\right) \frac{dP\left(\nu, \nu_0\right)}{dt} \tag{4.5}$$

which in the case of interest $\sigma_L \ll \sigma_D$, ie the case where the laser is tuned at resonance, becomes

$$\frac{d\bar{P}}{dt} \approx \sqrt{\frac{(m_p + m_\mu)\, c^2}{2\pi k T \bar{\nu}_0^2}} \left[\frac{\mu_B}{\hbar} \left(\frac{m_e}{m_p}\mu_p + \frac{m_e}{m_\mu}\mu_\mu \right) \right]^2 \boldsymbol{B}_0^2 \tag{4.6}$$

The squared modulus of the oscillating magnetic field $\boldsymbol{B}_0$ is related to the average density of the energy flux $|\bar{\boldsymbol{F}}|$ carried by the electromagnetic wave through the relation $\boldsymbol{B}_0^2 = (2\mu_0/c)|\bar{\boldsymbol{F}}|$, where μ_0 denotes the vacuum magnetic permeability.

By integrating Equation 4.6 over the duration τ of the laser pulse it's possible to obtain the spin-flip probability

$$\bar{P} = \frac{2\mu_0 \mu_B^2}{\hbar^2 c \bar{\nu}_0} \sqrt{\frac{(m_p + m_\mu)\, c^2}{2\pi k T}} \left(\frac{m_e}{m_p}\mu_p + \frac{m_e}{m_\mu}\mu_\mu \right)^2 \tau \left| \bar{\boldsymbol{F}} \right| \tag{4.7}$$

The energy flux density can be expressed in terms of the energy output E, the laser pulse duration τ and the cross section of the laser beam S through the relation $|\bar{\boldsymbol{F}}| = E/(S\tau)$. A direct relation between the spin-flip probability and the physical parameters of the laser and of the target can be obtained by substituting the energy flux density in the Equation 4.7. This relation is

$$\bar{P} \approx 8 \times 10^{-5} \frac{E\,[\mathrm{J}]}{S\,[\mathrm{m}^2]\,\sqrt{T\,[\mathrm{K}]}} \tag{4.8}$$

where T is the temperature of the target.

Equation 4.8 proves that the IR laser developed for the Lamb shift experiment of 2010 has an inadequate energy output for the setup devised by Bakalov *et al.* [15, 16]. As a matter of fact, a laser with pulse energy equal to 0.25 mJ [75] focused on a surface of 1 cm^2, for a target kept at 300 K, produces spin-flip scattering with a probability of only 1.2×10^{-5}, which is too small [16]. This probability may be increased by reducing the target's temperature, but T should be kept above ~ 10 K to avoid the formation of unwanted molecular ppμ ions.

The efficiency of the process may be also raised significantly by reducing the laser's cross section and placing the target within a multipass cavity that provides k reflections. The multipass cavity employed in the 2010 experiment had $k \sim 2 \times 10^3$ [75], which in this setup would increase the spin-flip probability up to 12%, a value much more reasonable for the intended purposes.

4.4 Muon transfer rate to higher-Z gases

The pivotal point of the procedure developed for the FAMU experiment is detecting those muonic atoms that have been excited by the laser and de-excited to intermediate energy levels. One way to do this is to introduce a higher-Z gas in the target: in this way in fact the muonic atoms will transfer their muons to the contaminating gas, thus exciting the

gas atoms and causing the production of characteristic X-rays during their de-excitation. As a result, by detecting the emitted X-rays it will be possible to derive the number of transferred muons.

More precisely, in a mixture of hydrogen and a small amount of contaminating gas, four processes can contribute to the extinction of muonic atoms: the decay of the muon, the formation of ppμ molecules, the transfer of muons to deuterium and the transfer of muons to the contaminating gas. Let λ_0, $\Lambda_{pp\mu}$, Λ_{pd} and Λ_{pG} be the rates related to these four processes respectively. Let also c_p, c_d and c_G be the concentrations of hydrogen, deuterium and contaminating gas. The total extinction rate λ of μp atoms can then be expressed as [73, 76, 88]

$$\lambda = \tau^{-1} = \lambda_0 + \phi \left[c_p \Lambda_{pp\mu} + c_d \Lambda_{pd} + c_G \Lambda_{pG} \right] \tag{4.9}$$

where ϕ is the atomic density of the gas mixture.

Characteristic X-rays are emitted immediately after a muon decay event or after the transfer of a muon from muonic hydrogen atoms. However, by using a properly-timed time window, it's possible to fit the X-ray spectrum and select only transfer events. The time distribution of the number of X-rays is expected behave like [52, 73]

$$N_{\gamma G}(t) \propto \Lambda_{pG} N_{\mu p}(t) \propto \Lambda_{pG} N^0_{\mu p} e^{-\lambda t} \tag{4.10}$$

where $N^0_{\mu p}$ represents the initial number of μp atoms.

In order to detect the presence of muonic atoms with increased kinetic energy the transfer rate Λ_{pG} has to depend on the energy of the muonic hydrogen atoms, so that this dependence will affect the distribution reported in Equation 4.10.

4.4.1 Measurement of the hydrogen to oxygen muon transfer rate

Usually the transfer rate doesn't depend on the energy, but for a particular gas this isn't true: oxygen. The first time this anomalous behaviour was noticed was during an experiment of Mulhauser *et al.* [70]. They investigated the muon transfer characteristic X-rays emitted by a target containing a mixture of hydrogen and sulphur dioxide.

The time spectrum of the delayed muonic sulphur 2P-1S transition, as well as the ones of the other sulphur Lyman and Balmer series transitions, showed no deviations from the theoretical predicted behaviour reported in Equation 4.10. As can be seen in Figure 4.9 (a), the spectrum shape for the sulphur 2P-1S transition is in fact that of a single exponential.

The spectra of the four detected muonic oxygen transitions, from 2P-1S to 5P-1S, presented instead other components which may be reproduced by using a function with three exponentials [70], such as

$$\frac{dN_{\gamma O}(t)}{dt} = A e^{-\lambda t} + \frac{C}{\tau_2 - \tau_r} \left(e^{-\frac{t}{\tau_2}} - e^{-\frac{t}{\tau_r}} \right) \tag{4.11}$$

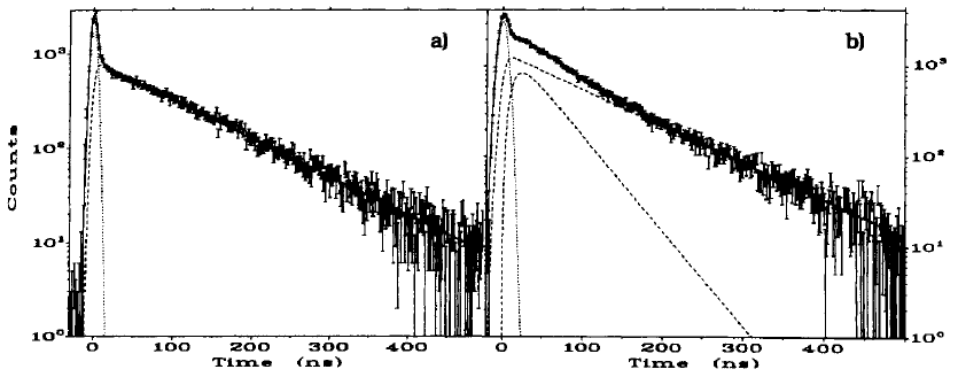

Figure 4.9: Measured time spectra of the sulphur (a) and oxygen (b) 2P-1S transitions in a $H_2 + 0.4\%SO_2$ gas mixture [70]. The gaussian represents the fitted prompt peak. The delayed part in (a) is fitted according to Equation 4.10, while the one in (b) is fitted according to Equation 4.11.

The measured time spectrum of the muonic oxygen 2P-1S transition is reported in Figure 4.9 (b).

Mulhauser *et al.* took measurements of the delayed X-rays for different pressures, from 10 to 15 bar, and for different concentrations of SO_2, from 0.1% to 0.6%. The anomalous behaviour of the muonic X-rays was present in all measurements: the muonic sulphur X-rays always followed a single exponential structure, while the muonic oxygen ones followed a triple exponential structure.

The time constant τ_r corresponds to a rise time, which was used to fit the bump in the spectra. As for τ_1, they concluded that it's the lifetime of the μp atoms in the ground state under their experimental conditions. They also hypothesized that the time constant τ_2, smaller than τ_1 and only present in the oxygen spectrum, is the lifetime of an unexpected μp atom which may transfer its muon only to oxygen [70].

Werthmüller *et al.* performed new experiments to further investigate this anomaly [88, 89]. In these experiments a new model was developed: they supposed that the unexpected μp(1S) atom may decay mainly through two different channels. The first one should depend on the hydrogen concentration c_p, while the other should depend on the oxygen concentration c_O. Due to these characteristics, the first one was deemed to describe the usual muon transfer from hydrogen to oxygen. As for the second channel, Werthmüller *et al.* concluded that it consisted in a process related to thermalization [89].

In order to describe these two transfer modalities, a simplified two-components model was devised [88, 89]. According to this model, the smaller time constant τ_2 represents the mean lifetime of epithermal μp atoms, that is muonic atoms which have a higher energy than the thermal one.

Figure 4.10 shows a schematic representation of the two-components model.

The model describes the muon transfer process starting two initial μp(1S) components: a thermal one and a hot one. Direct muon transfer from hot muonic hydrogen to oxygen is

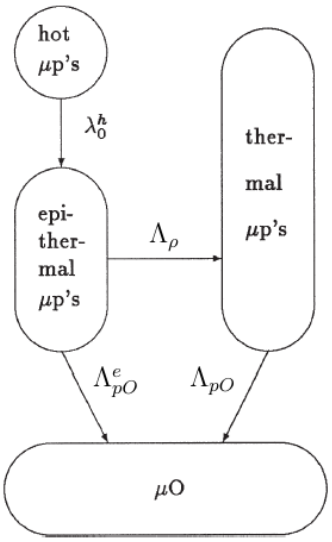

Figure 4.10: Schematic representation of the two-components model for the muon transfer from muonic hydrogen to oxygen [89].

neglected. According to this model, the hot atoms decelerate towards epithermal energies, ie an intermediate range of energies, with a deceleration rate λ_0^h. The epithermal muonic atoms may then either transfer their muon to oxygen atoms with a rate Λ_{pO}^e or de-excite to thermal energies with a rate Λ_ρ. The thermal muonic atoms may also transfer their muon to oxygen with a rate Λ_{pO}.

Since τ_2 has to describe the effect of epithermal atoms, Werthmüller *et al.* decided to define it as [89]

$$\tau_2^{-1} = \lambda_2 = \lambda_0 + \phi \left(c_p \Lambda_\rho + c_O \Lambda_{pO}^e \right) \tag{4.12}$$

Using Equation 4.9 and 4.12 in combination with the data taken in [70, 88, 89] for different pressures, oxygen concentrations and gas mixtures, namely $H_2 + 0.4\%SO_2$ and $H_2 + 0.4\%O_2$, they managed to derive the transition rates involved in these processes. These are $\Lambda_{pO} = 0.85(2) \times 10^{11}$ s^{-1}, $\Lambda_\rho = 8.1(4) \times 10^8$ s^{-1} and $\Lambda_{pO}^e = 2.08(3) \times 10^{11}$ s^{-1}.

These results prove that the hydrogen to oxygen transfer rate does indeed depend on the energy of the muonic atoms, but they are still not enough to gain a complete understanding of the muon transfer process. For this reason several studies are still underway to investigate the behaviour of Λ_{pO} for a wider range of experimental conditions. Between them, the ones performed by Mocchiutti *et al.* in 2016 [65] and by Pizzolotto *et al.* in 2018 [73] are particularly relevant.

These experiments were carried out at the RIKEN-RAL facility in anticipation of the FAMU experiment. The aim of the experiments was to measure the muon transfer rate from muonic hydrogen to oxygen in a wide range of temperatures, from 70 K to 336 K.

The experimental procedure employed is the one discussed through this chapter, the same one that will be used in the FAMU experiment: a muon beam hit a target containing hydrogen and oxygen, thus forming muonic hydrogen atoms. Once thermalized, the atoms were excited through a laser into the triplet state and were let to de-excite to the ground state. These atoms then transferred their muon to the oxygen atoms with the emission of characteristic X-rays.

The cryogenic target employed was composed by an aluminium cylindrical vessel filled with hydrogen and oxygen. The vessel was internally coated with a thin layer of gold and nickel in order to stop outgoing muons, and was surrounded by different types of X-ray detectors.

The pulsed muon beam used had a repetition rate of 50 Hz. Each bunch consisted of of two gaussian-shaped muon spills, with FWHM= 70 ns, separated by $\sim$ 320 ns.

The entire experimental apparatus will be described in greater detail in Chapter 5.

The experiment held in 2016 by Mocchiutti *et al.* [65] used a target filled at room temperature to 41 bar, with an oxygen concentration equal to $c_O = 190$ ppm. These physical parameters were chosen due to the results of Bakalov *et al.* [25], which showed that under these conditions the thermalization of muonic hydrogen atoms requires 150 ns, while the quenching of the $(1S)^{F=1}$ state requires 10 ns (see Figure 4.3 and Figure 4.6). For $c_O = 190$ ppm at this temperature and pressure, the average muon transfer rate from thermalized μp was found to be 0.78×10^6 s^{-1}, which is comparable to the muon decay rate. This choice allowed Mocchiutti *et al.* to observe the muon transfer process from thermalized muonic hydrogen atoms up to several microseconds [65].

Their data analysis considered only steady-state delayed X-ray events produced by thermalized atoms. The transfer rate Λ_{pO} was measured by fitting the time evolution of the oxygen X-rays with Equations 4.9 and 4.10. The transfer rate Λ_{pO} was left as a free parameter.

The values used for the other transitions rates were $\lambda_0 = (4665.01 \pm 0.14) \times 10^2$ s^{-1} and $\Lambda_{pp\mu} = 2.01 \times 10^6$ s^{-1} [18, 65, 81]. The hydrogen to deuterium muon transfer rate Λ_{pd} was found to vary from 8.65×10^9 s^{-1} at 100 K to 8.20×10^9 s^{-1} at 300 K (normalized to 2.125×10^{22} HD molecules/cm^3). As for the gases' density and concentration, the measures performed gave $\phi = (4.869 \pm 0.003) \times 10^{-2}$, $c_d = (1.358 \pm 0.001) \times 10^{-4}$, $c_O = (1.90 \pm 0.04) \times 10^{-4}$, all expressed in LHD units. The hydrogen concentration was simply determined as $c_p = 1 - c_O - c_d$.

The experimental sample used in the experiment of 2016 consisted of about 2.6×10^6 muon triggers, which in turn produced $\approx 7.8 \times 10^7$ X-rays [65]. The time trigger signaling the start of the data acquisition for each X-ray was generated by the beam control system. The time reference frame was devised so that the two muon spills composing a single emission of the pulsed muon beam peaked at $\sim$ 530 ns and $\sim$ 850 ns, with each spill containing $\approx 10^3$ muons.

The X-ray energy spectrum emitted by the target was measured at six different temperatures: 104, 153, 201, 240, 272 and 300 K. Mocchiutti *et al.* reconstructed the X-

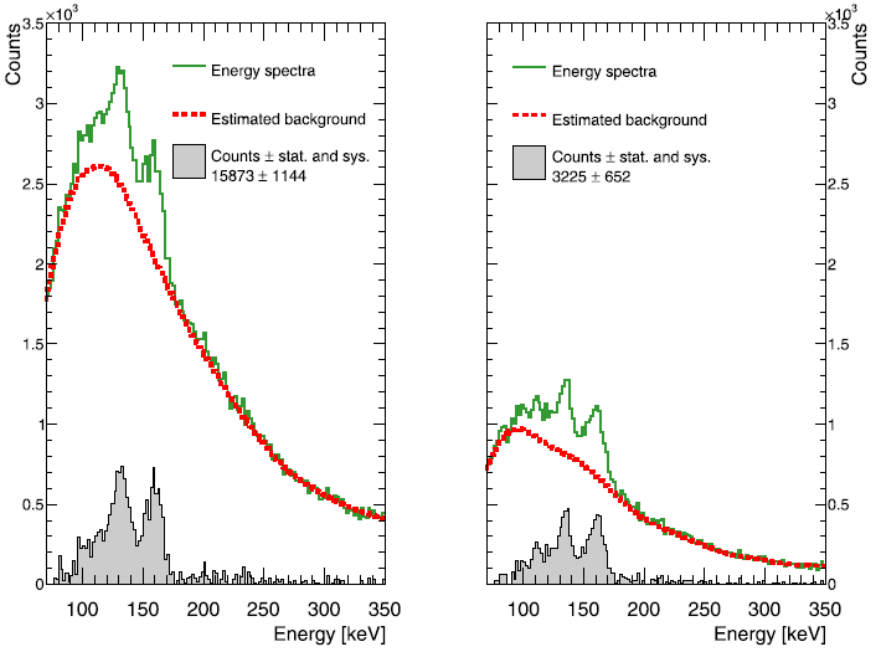

Figure 4.11: Energy spectra taken at 104 K for two different time bins [66]. The solid green lines represent the measured X-ray spectra, while the dotted red lines represent the estimated background. The signal obtained after background subtraction is shown in grey.

ray signals by fitting the detector waveforms. Waveforms with reduced $\chi^2 < 100$ produced non-convergent fits or poorly reconstructed events and were thus rejected. Furthermore, the required distance between events had to be more than 30 ns: simulations in fact showed that such condition guarantees a software reconstruction efficiency and accuracy better than 99.9% [65]. A more detailed discussion on the selection procedure and on the reconstruction efficiency may be found in [66].

Figure 4.11 shows two energy spectra measured at 104 K, each corresponding to a different time bin. The background signal estimation was carried out by filling the target with H_2 only and by taking data in the same experimental conditions employed for the H_2+O_2 gas mixture. The gaussian spectra were smoothed with a gaussian kernel algorithm [66, 79] due to the presence of high fluctuations in the background. The tails present at lower energies were caused by energy leakages from the detectors' LaBr crystals.

It can be seen that the X-ray obtained after background subtraction had an energy that spanned from 100 to 200 keV. The total number of X-rays went from a few hundreds to about ten thousands depending on the target temperature and time bin. The systematic errors caused by the background normalization were estimated using a statistical approach based on the number of background and signal events in the normalization interval. Further systematic errors were estimated by comparing the background signal taken from a H_2 filled target with the ones obtained from other gas mixtures, like H_2+C_2 and H_2+Ar.

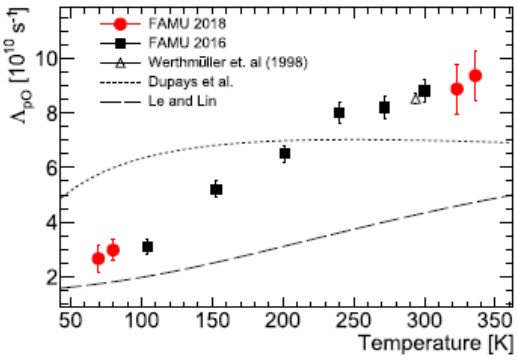

Figure 4.12: Hydrogen to oxygen muon transfer rate Λ_{pO} as a function of temperature [73]. The data reported are related to experimental measurements (Werthmüller *et al.* [89], Mocchiutti *et al.* [65] and Pizzolotto *et al.* [73]) and theoretical results (Dupays *et al.* [45] and Le and Lin [61]).

The total systematic error of each signal spectrum was quadratically summed to the statistical error.

The measured hydrogen to oxygen muon transfer rates, extrapolated from the X-ray energy spectra, are reported in Figure 4.12, together with the results from the experiment of 2018 [73].

Pizzolotto *et al.* used the same apparatus employed in 2016 to perform new measurements of the hydrogen to oxygen muon transfer rate at the same six temperatures, which were 104, 153, 201, 240, 272 and 300 K. In order to expand the temperature range where Λ_{pO} is known, they also performed new measurements at 70, 80, 323 and 336 K [73]. The data were taken in two different sessions, one in March 2018 and the other in December 2018.

An important difference with the experimental methodology employed in [65] was the determination of the oxygen concentration value: this in fact wasn't measured directly, but extracted from the data. More precisely, they determined c_O by comparing and normalizing the data taken in 2016 [65] and 2018 [73] at the same temperatures.

The first step of this procedure consisted into fitting the data taken by Mocchiutti *et al.* to the lowest order polynomial that described well enough the data. This was deemed to be a 2^{nd} degree polynomial, with a constant coefficient denoted by k_{2016} and two higher order terms denoted by k_1 and k_2.

Then, an initial value of c_O was selected. This was done in order to perform a first estimation of the transfer rate Λ_{pO} at the normalization temperatures of 104, 153, 201, 240, 272 and 300 K.

Lastly, the data taken in 2018 were fitted for the same 2^{nd} degree polynomial by fixing k_1 and k_2 and leaving the last coefficient k_{2018} as the only free parameter. The fit was performed separately for the March and December data measurements.

The final value of c_O was determined through the minimization of χ^2 defined as [73]

$$\chi^2(c_O) = \frac{\left[k_{2018}(c_O) - k_{2016}\right]^2}{\sigma_{2018}^2 + \sigma_{2016}^2} \tag{4.13}$$

where σ represents the error on the respective k parameter.

The oxygen weight concentration at minimum χ^2 were $c_O = 1.61 \pm 0.11\%$ in March 2018 and $c_O = 0.51 \pm 0.06\%$ in December 2018.

As can be seen in Figure 4.12, the experimental values of the muon transfer rate are in agreement with each other [65,73,89] but incompatible with the theoretical results [45,61]. For this reason new theoretical models for the hydrogen to oxygen muon transfer rate are still being developed.

Chapter 5

The FAMU apparatus

The main processes involved in the FAMU experiment are the formation of muonic hydrogen and the transfer of the muon from hydrogen to oxygen. These processes impose strict requirements not only on the apparatus itself, but also on the muon beam employed in the experiment.

Since the number of produced μp atoms should be in fact as high as possible in order to guarantee a sufficiently high muon transfer probability, a negative muon beam with high intensity is necessary.

This condition alone however is not enough to guarantee the success of the experiment: due to the gaseous nature of the hydrogen inside the target the muons of the beam must have low energy, otherwise they will simply cross the target without interacting with the gas.

Furthermore, the high precision measurements that the FAMU experiment requires can only be achieved by using a pulsed muon beam instead of a continuous one. A pulsed muon beam in fact allows to increase the signal to noise ratio by synchronizing the observation time window with the muon pulse [63].

Lastly, the generated muonic hydrogen atoms need to have enough time to completely thermalize and depolarize, which implies that the pulses of the beam must be interspersed by a sufficiently long time.

There are several facilities able to produce a negative muon beam, but only few of them satisfy the requirements of the FAMU experiment. The RIKEN-RAL facility was chosen among them since it best fits the FAMU necessities.

The first sections of this chapter will focus on the facility and on its muon beam, while the other sections will describe in detail the other components built for the sake of the experiment. The full apparatus is shown in Figure 5.1.

A portion of the experimental apparatus, namely the main crown of $LaBr_3$ detectors, will be described separately in the next chapter.

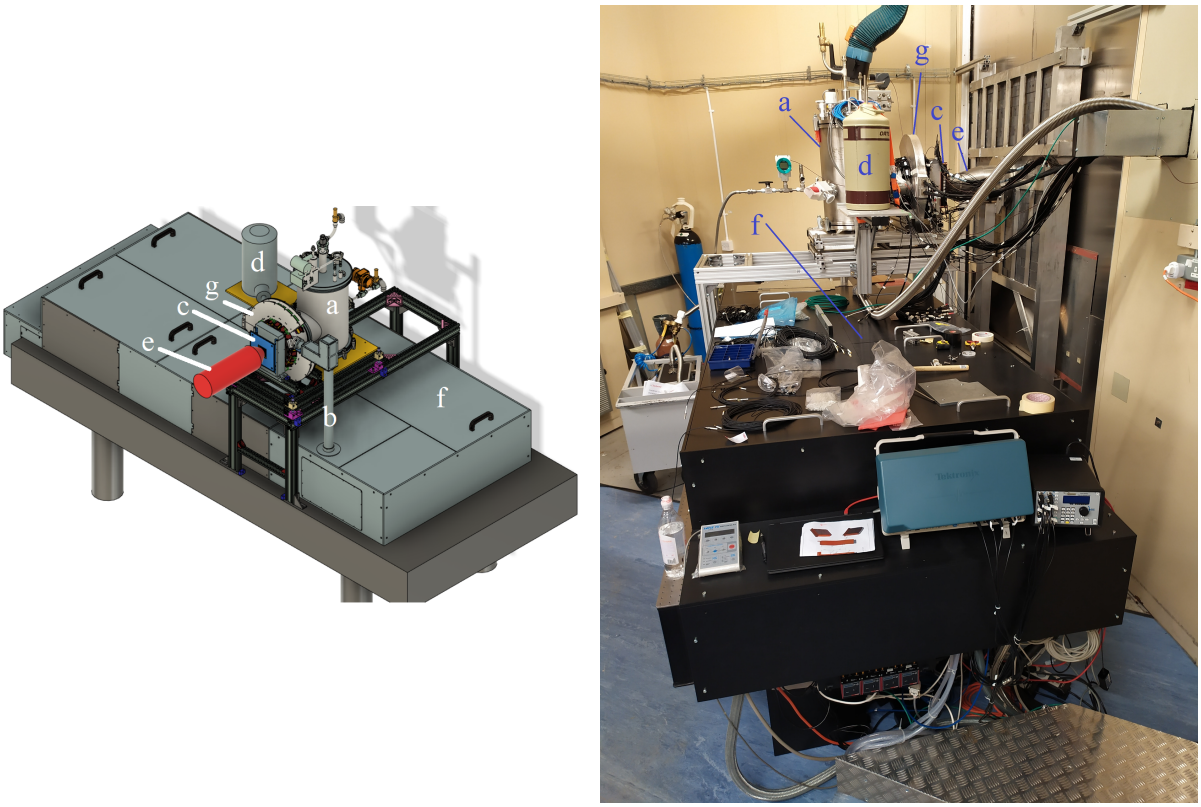

Figure 5.1: Experimental apparatus employed in the FAMU experiment, reported through a CAD representation on the left [72] and through a photo on the right. The elements denoted by letters are: a) the cryostat, b) the laser's optical path, c) the hodoscope, d) the nitrogen container for the HPGe detector, e) the beam entrance, f) the shielding containing the laser and g) the main and auxiliary detector crowns. When the photo was taken the laser was under maintenance, so the laser's optical path was missing.

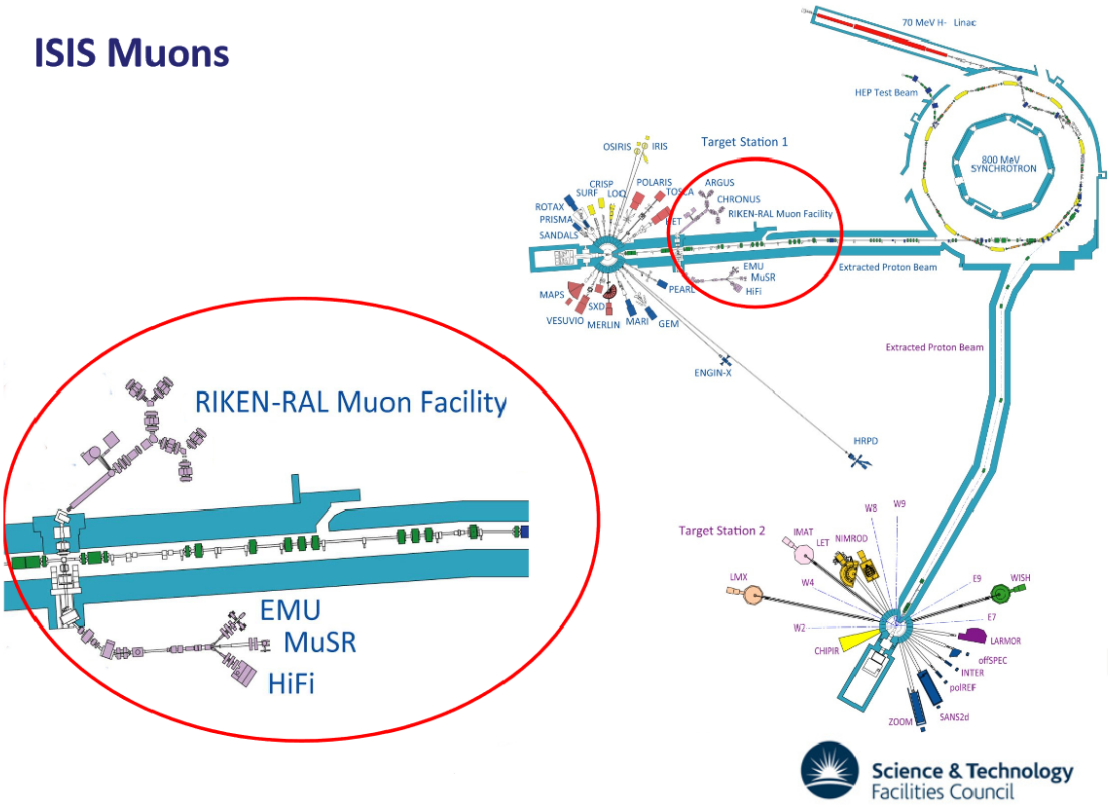

Figure 5.2: Layout of the ISIS Neutron and Muon Source research institute [76]. The circle contains a zoom on the seven experimental ports for muon experiments.

5.1 The RIKEN-RAL facility

The RIKEN-RAL pulsed muon facility was built after an international agreement in 1990 between the japanese institution RIKEN and the british Rutherford Appleton Laboratory, or RAL for short [63, 71]. It is part of the ISIS Neutron and Muon Source research institute, which is managed by the Science and Technology Facilities Council [10]. The layout of the ISIS facility is shown in Figure 5.2.

The ISIS facility contains two different targets for neutron production that are located at Target Station 1 and 2, and a single target for muon production placed 20 m upstream of the Target Station 1. The muon production target can be chosen between three graphite plates with thicknesses equal to 5, 7 and 10 mm respectively [46, 63]. The μ^- and μ^+ produced by said target feed then seven experimental ports, shown in the red circle in Figure 5.2. Four of these seven experimental ports belong to the RIKEN-RAL facility, and are reported in greater detail in Figure 5.3. The FAMU experiment will be held at Port 1.

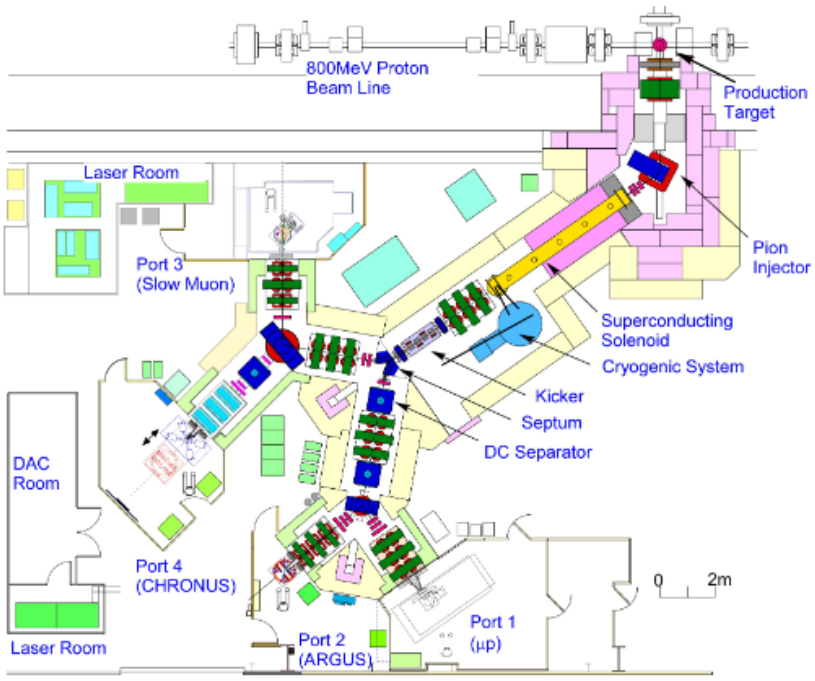

Figure 5.3: Layout of the four experimental ports of the RIKEN-RAL facility [9].

5.2 The muon beam

The ISIS facility contains a rapid cycle synchrotron that produces a high intensity double pulsed proton beam with energy, average current and repetition rate equal to 800 MeV, 200 μA and 50 Hz respectively [49, 63].

The beam crosses the graphite target and gives rise to nuclear reactions that generate pions. These pions are collected and momentum-analyzed by the pion injection system, composed by two quadrupole magnets and a single dipole magnet. Three Cherenkov detectors are installed after the pion injection system to provide the triggering signal for the experiments.

The produced pions reach then a superconducting solenoid magnet which acts as the decay section of the muon beamline. Here, the pion generate muons through $\pi - \mu$ decay, which are collected by the muon extraction system and delivered to each port [63]. Several DC separators are positioned along the beamline in order to remove positron/electron contamination.

The muon beam thus produced is divided into two beams composed respectively by negative and positive decay muons with a momentum that ranges from 20 to 120 MeV/c. Each pulse of the beam has a FWHM of 70 ns and two successive pulses of the same bunch are separated by 320 ns. The repetition rate of the muon beams mirrors that of the original proton beam, that is, it's equal to 50 Hz [12]. The beams' momentum

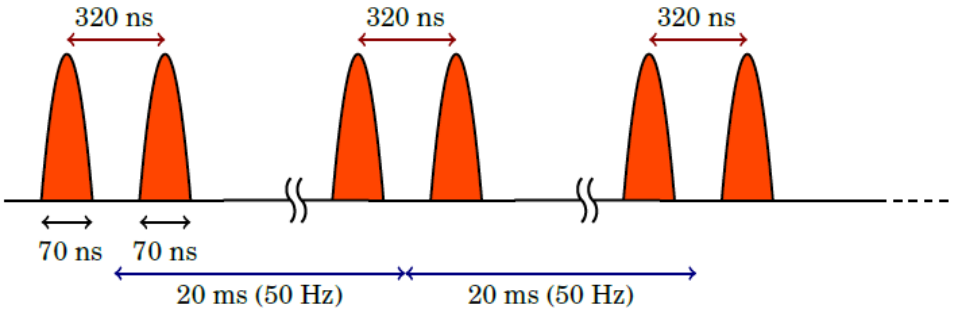

Figure 5.4: Time structure of the RIKEN-RAL pulsed muon beam [52].

spread is $\sigma_p/p \approx 4\%$ and their transverse sections are $\sigma_x, \sigma_y = 1.5$ cm [12, 72]. Figure 5.5 contains a representation of the final muon beams. The negative muons are sent to the four RIKEN-RAL ports, while the positive muons are sent to remaining three ports.

For experiments that require muons with momentum up to 65 MeV/c, a kicker magnet and a septum magnet can be used to split the double pulsed negative muon beam into two single pulsed muon beams. These are then sent to two different ports, allowing the researchers to perform two experiments at the same time [63].

For momenta requirements that go from 65 to 120 MeV/c it's not possible to split the beam, which means that it's delivered to one experiment port only as it is.

In addition to the decay muon beams, another high quality beam composed by surface muons can be sent to each port, where the term "surface muons" refers to muons produced by $\pi - \mu$ decay at the surface of the graphite production target. These surface muons have a momentum that ranges from 20 to 30 MeV/c [63].

The predicted muon intensity as a function of momentum for both the surface beam and the two decay muon beams are shown in Figure 5.5, together with the corresponding measured values. The calculations were performed assuming a proton beam intensity of 200 μA, a target thickness of 10 mm and a focusing point of 4×4 cm^2 [63]. More informations on the calculations and on the programs used to perform them can be found in [37, 38, 53].

For the purposes of the FAMU experiment, the beam must be set to contain negative muons with momentum in the $40 - 80$ MeV/c range.

5.3 The hodoscopes

Since the FAMU experiment requires high precision, the beam's physical parameters must be periodically checked and kept under control. For this reason a set of four custom hodoscopes has been devised [33, 34, 72]: these hodoscopes are used to fine-tune the beam, to monitor the the intensity of the beam pulses and also to provide timing information to the DAQ readout. The models differ for the materials used, but their shape remains

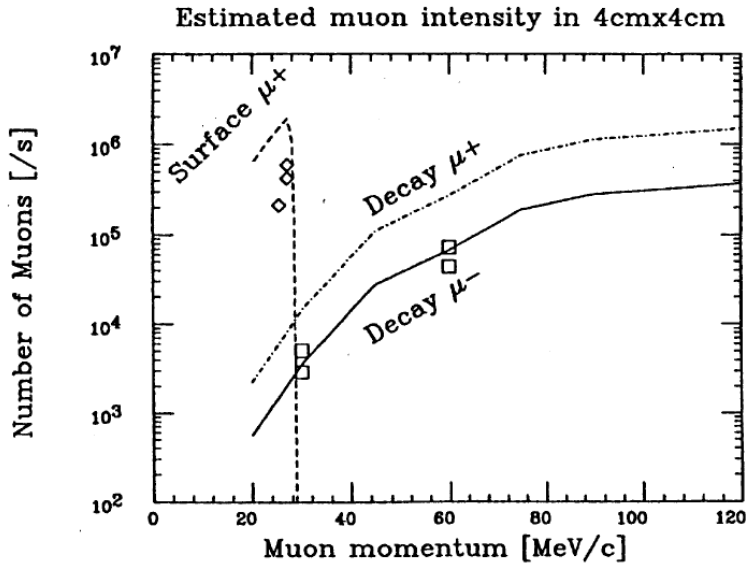

Figure 5.5: Calculated and measured values for the muon beam intensity [63]. The lines describe the calculated values, while the open squares denote the measured intensities.

quite similar. Figure 5.6 shows the third hodoscope during its construction, while Figure 5.7 shows instead the fourth hodoscope mounted on the FAMU experimental apparatus.

This section will cover first the common features of the different hodoscope models, and will then delve into their differences and uses.

All hodoscopes use $32 + 32$ square single-clad Bicron BCF-12 scintillating fibers arranged in two different crossing planes along the X/Y axis, defined here as the two orthogonal axis perpendicular to the beamline. The square shape of the fibers reduces the amount of dead space and makes the response of the detector independent from the position of the muon trajectory inside a fiber [34]. All fibers have been cut at CERN with a Fiberfin4 machine, which provides ready-to-use fibers with polished ends.

The Bicron BCF-12 fiber model, produced by the french industry Saint-Gobain, has a decay time of 3.2 ns and emits 435 nm blue light when hit by a crossing particle. The number of emitted photon per MeV, for minimum ionizing particle and corrected for PMT sensitivity, is ~ 8000 photons/MeV [78]. The scintillator fibers employed have a polystyrene-based core.

The scintillation light emitted by a muon passing through a fiber is read by silicon photomultipliers, or SiPMs for short. Since the SiPM package footprint is bigger than the fiber size, the fibers are read alternating left/right and up/down sides [33, 34]. The front end circuits consist of refurbished electronic boards from the INFN TPS project [36, 74] and provide power to the SiPMs up to 40V. The temperature gain drift of the SiPMs is controlled by CAEN DT5485 digital voltage supplies with built-in feedback on temperature,

Figure 5.6: Photos of the third hodoscope during its construction [34]. The hodoscope is shown without its cover in the left panel and with it on the right panel.

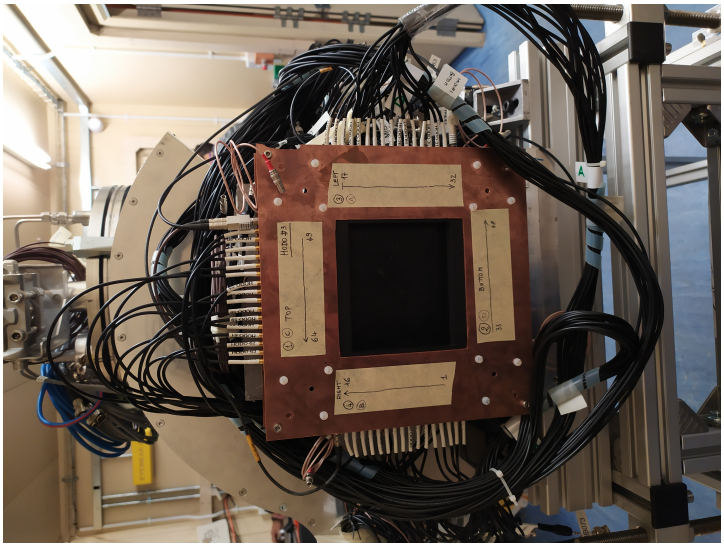

Figure 5.7: Photo of the fourth hodoscope taken from the beam entrance side.

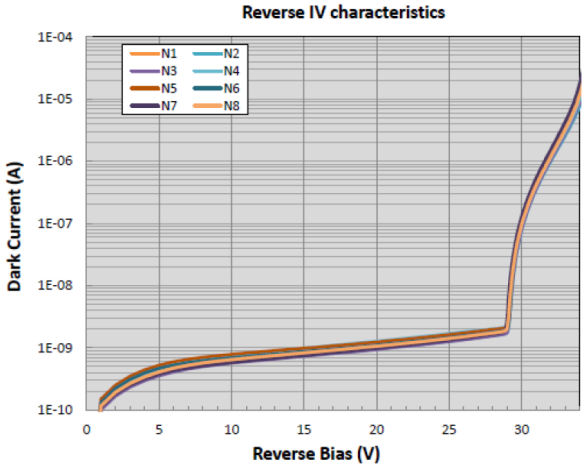

Figure 5.8: Reverse current-voltage characteristics for a sample of SiPMs for the first model of hodoscope [34]. The measurements were taken at 25 °C.

which are measured by Analog Devices TMP37 thermistors with ±2% precision [32, 72].

The output signals do not require amplification: typically in fact they have an amplitude of ~ 40 mV with $S/B \sim 10$ [33]. These output signals are digitized by a fast FADC operating at 1 Gs/s. The model is CAEN V1742 FAC with 5 Gs/s, 12 bit and 1 Vpp input dynamic range in VME standard. The FADC operates at a reduced sampling rate in order to increase the digitizing buffer time [33, 34].

The first two hodoscopes have an active area of 10×10 cm^2. The fibers employed in its construction have a thickness of 3×3 mm^2 and are connected to 3×3 cm^2 Advansid RGB SiPMs, with 40 μm cells. Each fiber is wrapped in an aluminium foil ~ 10 μm thick in order to avoid light crosstalk. The SiPM bias and signal output is conveyed through single RG174 cables, with MCX connectors on one side and LEMO00 on the other [34]. The SiPM were tested and the estimated breakdown voltage is 29.1 V. Figure 5.8 reports the current-voltage characteristics of a sample of SiPM.

The third hodoscope model has an active area of 3.2×3.2 cm^2 and is composed by 1 mm^2 fibers connected to 1×1 mm^2 Advansid RGB SiPMs with 40 μm cells. Instead of aluminium in this model the fibers are coated with an extra-mural absorber, or EMA for short, with a thickness of ~ 15 μm composed by PMMA (polymethylmethacrylate $C_5H_8O_2$) [34, 52].

There are several factors that lead to the choice of Advansid RGB SiPM as photodetectors in this and in the previous models: they have a short pulse duration, high photon efficiency, a peak emission that is well matched to that of the BCF-12 fibers (photon detection efficiency $\sim 22\%$ at ~ 440 nm, with 4 V overvoltage) , low operating voltage (breakdown voltage $V_{brk} \sim 29$ V), small breakdown voltage dependence from temperature (~ 27 mV/C) and low dark noise [34].

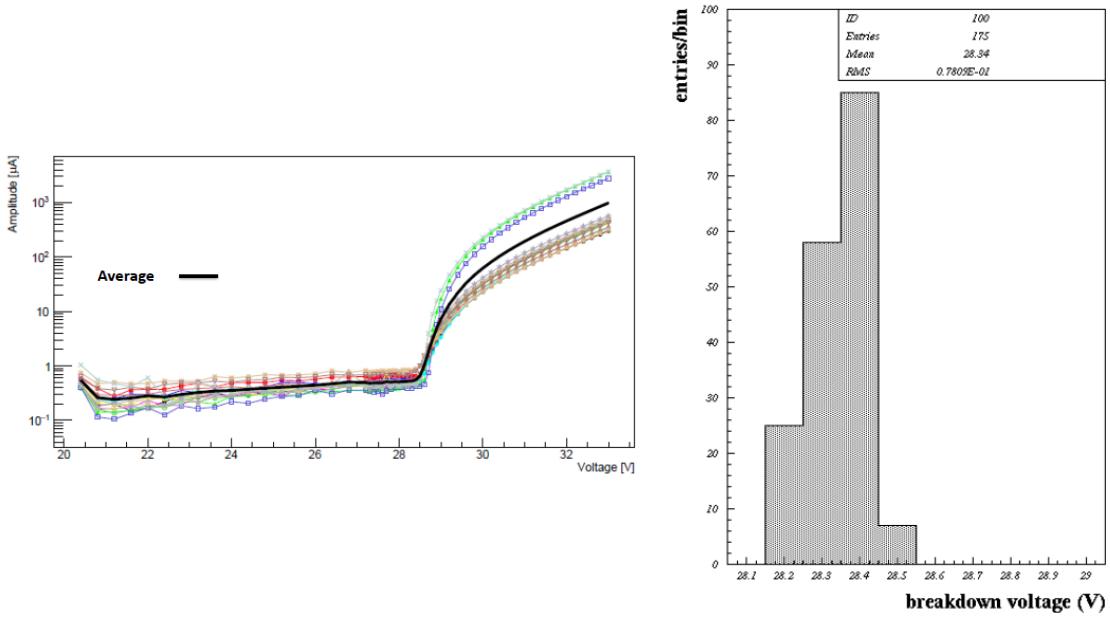

Figure 5.9: Results of the tests performed on the SiPMs employed in the third hodoscope model [34]. The reverse current-voltage characteristic is reported in the left panel, the distribution of the breakdown voltage is shown in the right panel.

For this hodoscope model, the breakdown voltages of all available SiPMs were tested individually through their current-voltage characteristic. This was done in order to select SiPMs with similar V_{brk} and therefore to employ a common voltage for their biasing. The results are shown in Figure 5.9.

The second and third hodoscope models have been texted at port 1 of the RAL facility during two different runs. The X/Y profiles measured during the runs are reported in Figure 5.10.

The fourth and last hodoscope model is composed by 0.5×0.5 mm^2 scintillating fibers read by 1×1 mm^2 Hamamatsu S12751 $-$ 050P SiPM and has an active area of 7.2×7.2 cm^2 [32, 72].

The two 3 mm pitch hodoscopes have been used during preliminary measurements performed with the FAMU apparatus [34, 39] and are nowadays employed only during special runs where a complete beam characterization is needed [33]. The 1 mm pitch hodoscope has been used during normal runs, and is now being substituted by the 0.5 mm pitch hodoscope.

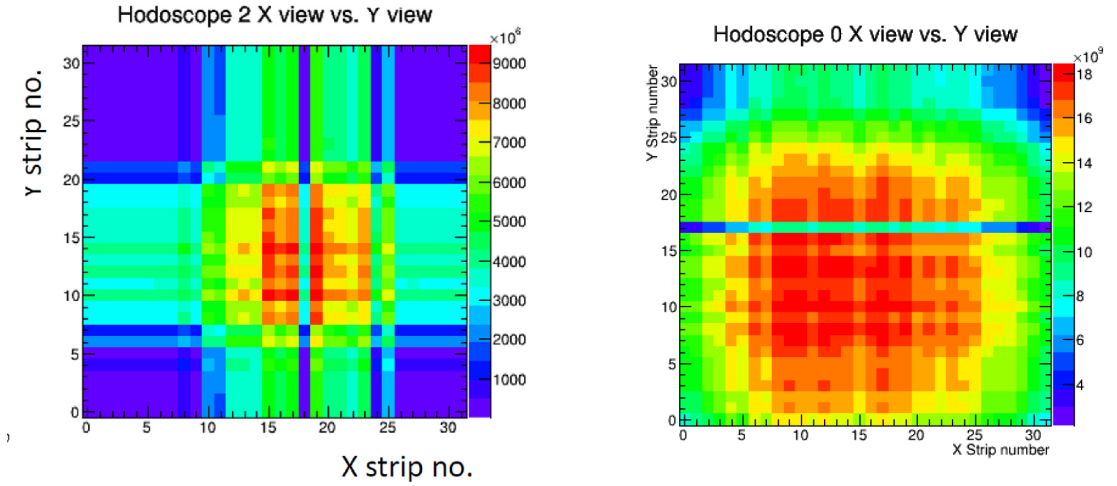

Figure 5.10: X/Y beam profiles measured at port 1 of RIKEN-RAL facility for the second hodoscope model (left) and the third one (right) [12, 33]. The profile on the left has been measured during a 60 MeV/c run, while the one on the right has been measured during a 57 MeV/c run.

Wavelength range	6800 ± 50 nm	≈ 44 THz
Energy output	> 1 mJ	Progressively up to > 4 mJ
Linewidth	< 0.07 nm	450 MHz
Tunability steps	0.03 nm	200 MHz
Pulses duration	10 ns	
Repetition rate	25 Hz	

Table 5.1: Requirements for the FAMU laser system [72].

5.4 The laser

A custom pulsed tunable narrow-band laser system is under development for the purposes of the FAMU experiment. Due to the requirements of the experiment itself the laser system must satisfy a set of strict requirements, which are listed in Table 5.1.

The laser system design is based on direct difference frequency generation, or DFG for short, in non-oxide crystals like lithium thioindate ($LiInS_2$) and lithium selenoindate ($LiInSe_2$). The difference frequency generation is a nonlinear process in which two photons with different energy and frequency are used to produce a third photon with frequency equal to the difference between the frequencies of the two initial photons.

In this particular instance, a single longitudinal mode Nd:YAG laser (1.064 μm) is mixed with a tunable Cr:forsterite laser (1.262 μm) which is pumped by a second Nd:YAG laser synchronized to the first one [72, 80]. A block scheme of this setup is shown in Figure 5.11.

In order to produce and energy output higher than 1 mJ at ~ 6.8 μm, the Nd:YGA

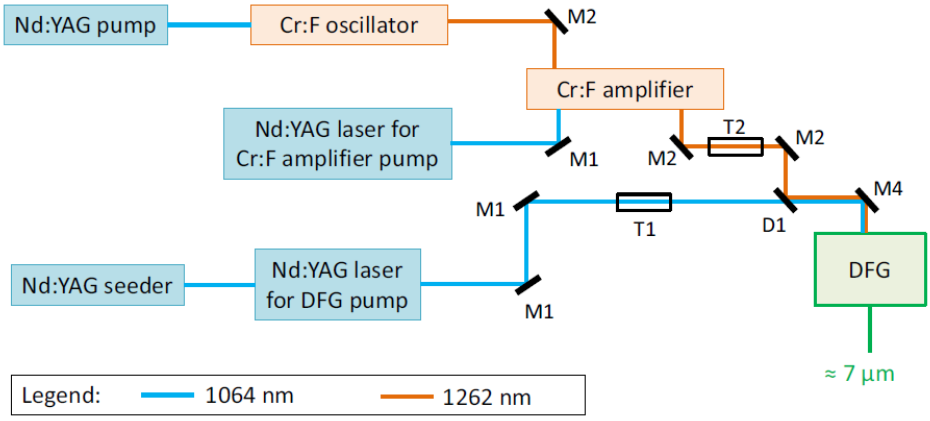

Figure 5.11: Block scheme of the laser system under development for the FAMU experiment [72]. The letters M, T and D stand for mirror, telescope and dichroic mirror respectively.

laser must have an energy ≈ 70 mJ while the Cr:forsterite laser must have energy ≈ 35 mJ. At present, a multipass multi-stage amplifying system has been built in order to have finely tunable wavelength and narrow bandwidth at 1.262 μm and energy up to 24 mJ [80].

The central wavelengths of the pump lasers are stabilized with an active temperature stabilization system.

Currently, the measurements of the wavelengths of the 6.8 μm DFG emission is performed by a wavelength meter based on solid state Fizeau interferometers [72]. This instrument is able to measure the central wavelength with an absolute accuracy of 200 MHz and the linewidth with an absolute accuracy of 400 MHz in the spectral range $2-11$ μm. The wavelength meter measures the wavelength of each single pulse so that if the emission of one of the lasers, and therefore of the DFG emission, were to change, it would still be possible to control the exact wavelength produced by DFG.

For the absolute calibration of the laser system, a C_2H_4 cell has been chosen. This particular cell in fact has several accurate absorption lines near 6.8 μm, which make it well suited for the task [72]. The absorption spectrum in the range of interest is reported in Figure 5.12. The accuracy ranges from ± 10 to ± 140 MHz, with the stronger lines being more accurate.

5.5 The cryogenic system

The cooling system employed at FAMU is based on liquid nitrogen LN_2. This choice was made due to the fact that the laser's optical path is sensitive to vibrations. A liquid nitrogen system optimizes the mechanical stability of the apparatus and eliminates the vibrations that would be instead produced by cryogenic pumps.

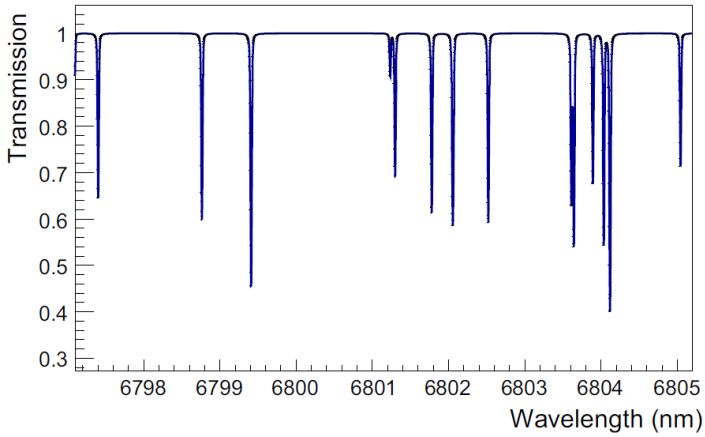

Figure 5.12: Absorption spectra of C_2H_4 near 6.8 μm [72]. The temperature was set at 296 K, the concentration at 100%, the pressure at 5 mbar and the absorption length at 10 cm.

The current model, shown in Figure 5.13, was shaped according to the needs of the optical cavity that it hosts. It includes a 5 liters tank which, assuming a load of $\sim$ 1.7 W, guarantees a 5 days duty cycle at the operating temperature of 80 K [72].

The feeding and purging pipes connecting the cooling system to the LN_2 refilling system are always in place and transfer liquid nitrogen from a 100/500 liter dewar.

The system can be checked and remotely tuned through two temperature sensors, a resistance heater and a digital pressure sensor. The fuel tank contains also a LN_2 level sensor.

The muons enter the cryogenic system through an aluminated mylar window with a thickness of 0.2 mm.

5.6 The target system

The design of the pressurized target system is the result of the balancing of two different factors: these are the maximization of the number of muons stopped by the gas in the optical cavity, and the minimization of the noise coming from the muons stopped elsewhere [72]. The trade-off between these quantities is what lead to the current shape of the vessel, which is reported in Figure 5.14. Figure 5.15 shows instead the placement of the target inside the apparatus.

The target vessel consists of an aluminium box with rounded corners on the front and a removable cap on the rear. In order to capture the muons that manage to reach the target walls, the inner walls of the pressurized target cylinder are coated with gold and nickel.

The vessel is gas tight and permits both an efficient cleaning and an efficient refilling of the gas.

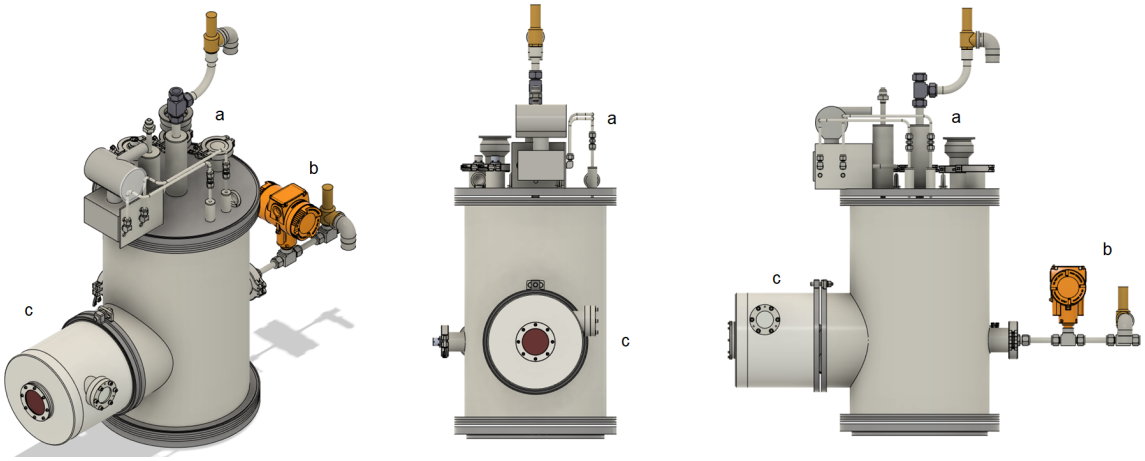

Figure 5.13: CAD representation of the cryogenic system. The letters indicate different parts: **a)** liquid nitrogen feeding and purging pipes, **b)** gas entrance, **c)** beam entrance window. The optical cavity, not shown, is inside the beam entrance window.

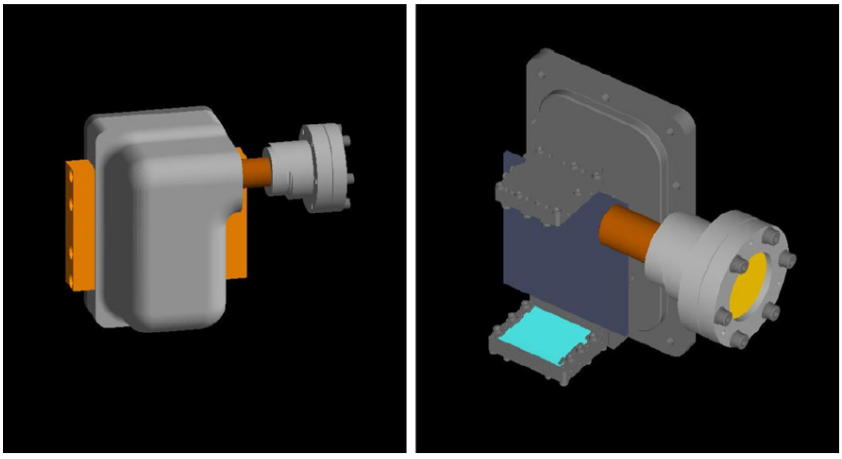

Figure 5.14: GEANT4 simulation of the gas target [72]. The left panel shows the gas target front view when this is closed, together with the laser entrance flange and the pipe connecting it to the target. The right panel instead shows the inside of the target, with the mirror of the optical cavity coloured in cyan. The thin dark grey slab represents the lead absorber.

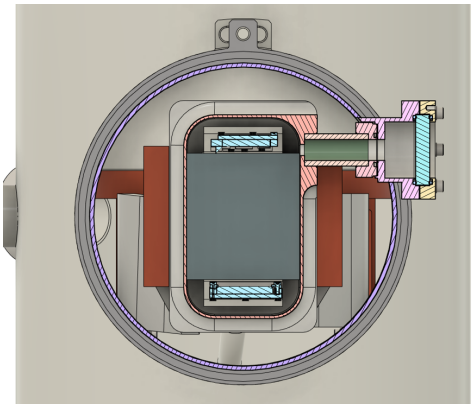

Figure 5.15: CAD representation of the gas target placement inside the beam entrance window.

A thin ~ 0.6 mm layer of silver has been placed inside the pressurized vessel just in front of the cavity in order to slow down the muons entering the illuminated region, thus increasing the number of muons stopped inside the gas. Furthermore, this layer of silver reduces the noise coming from the aluminium vessel itself.

A lead circle 3 mm thick covers the rear of the vessel and absorbs the majority of the muons that aren't stopped by the gas mixture inside the target. The rear cap is screwed to the vessel body and it's sealed with the use of a malleable indium O-ring. The gas enters the target through the rear.

5.7 The optical cavity

The laser alone is not capable of producing an adequate number of spin-flip transitions in μp atoms. For this reason, an optical cavity has been devised and placed inside the gas target.

A multipass optical cavity suitable for muonic experiments had already been devised at the Paul Scherrer Institute [85], but the requirements of the FAMU experiment are much stricter and a new design was needed.

Before describing the technical details of the FAMU optical cavity, a brief theoretical description of the principles behind this component will be given.

The optical cavity is an instrument used to contain light waves in order to increase the exposure time of the target placed in it. In the specific case of the FAMU experiment, a higher exposure time means a higher number of muonic atoms excited by the laser, which implies a higher probability that a spin-flip event will happen. This enhancing effect is described by the amplification factor $A(t)$ defined as follows [26].

In first approximation, let the density of muonic atoms be uniform inside the volume V, which is assumed to coincide with the volume of the whole cavity. Let the cavity be composed by two parallel mirrors with reflectance R at distance d. Let the amplitude of

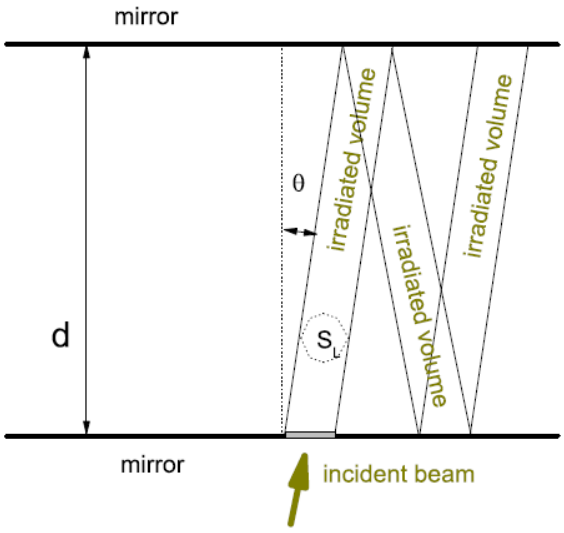

Figure 5.16: Schematic representation of the propagation of the laser beam inside the multipass optical cavity [26].

the magnetic field carried by the laser plane wave at the position $\boldsymbol{r}$ of the μp atom be $\boldsymbol{B}(\boldsymbol{r})$, with average at wavelength scale equal to $\overline{|\boldsymbol{B}(\boldsymbol{r})|^2}$, and let the laser cross section be s_L.

The irradiated volume is modeled as a series of cylindrical segments with a base area equal to s_L and height equal to $d\cos\alpha$, which can be approximated to d for incidence angles $\alpha \ll \pi/2$. The time required for the laser light to travel through a segment is $\tau_d = d/c$. In this first approximation it's assumed that the gas target is perfectly transparent for the laser light, so that the value of $\overline{|\boldsymbol{B}(\boldsymbol{r})|^2}$ doesn't change along a segment. The overlapping of two segments is not included in this approximation. At each reflection, the value of the average magnetic field $\overline{|\boldsymbol{B}(\boldsymbol{r})|^2}$ is suppressed by the factor R.

Let the laser pulse duration be τ_L, measured with respect to the time $t_0 = 0$ at which the laser light enters the cavity. The average magnetic field carried by the laser at the entrance is $\overline{|\boldsymbol{B}(\boldsymbol{r})|^2} = \boldsymbol{B}_0^2$. At each τ_D another segment inside the gas target is illuminated. A schematic representation of this model is shown in Figure 5.16.

The number of laser stimulated spin-flip events inside the volume V in a time range $[t_0, t]$, for $t \leq \tau_L$, can be expressed as [26]

$$N\left(t_0, t, V\right) \propto s_L \boldsymbol{B}_0^2 \left(\frac{c}{1-R} t - d \frac{R\left(1 - R^{\frac{tc}{d}}\right)}{(1-R)^2} \right), \quad 0 \leq t \leq \tau_L \tag{5.1}$$

where the proportionality constant depends on the temperature inside the cavity volume.

After the laser pulse stops the irradiated spot continues to propagate inside the cavity

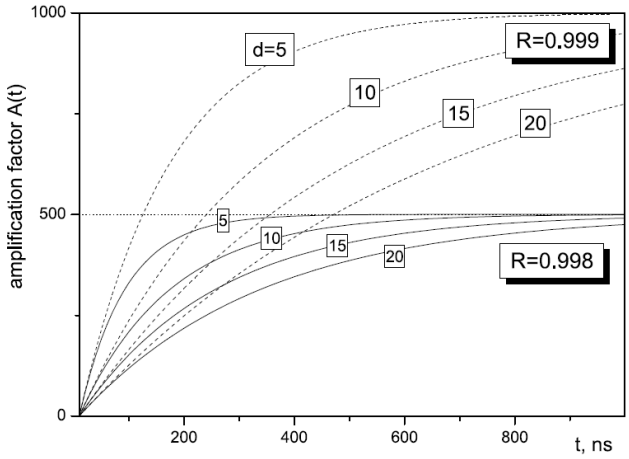

Figure 5.17: Plots of the amplification factor as a function of time for typical values of the reflectance R and of the distance between mirrors d [26]. The laser pulse duration was set to $\tau_L = 20$ ns. The calculations were performed using Equation 5.3.

while being suppressed at each new reflection by the factor R. In other words, the laser continues to induce spin-flip events for a limited time even after its pulse ends. The number of these last events can be determined through the equation

$$N\left(\tau_L, t, V\right) \propto s_L \boldsymbol{B}_0^2 \frac{d}{\left(1-R\right)^2}\left(1-R^{\frac{c\tau_L}{d}}\right)\left(1-R^{\frac{c(t-\tau_L)}{d}}\right), \quad t \geq \tau_L \tag{5.2}$$

The total number of events caused by the containment of the laser inside the cavity is simply $N(0,t,V) = N(0,\tau_L,V) + N(\tau_L,t,V)$. The amplification factor of the multipass cavity can then be defined as [26]

$$A\left(t\right) = \frac{N\left(0,t,V\right)}{N_0} = \frac{1}{1-R}\left(1+\frac{\tau_d}{\tau_L}\left(1-R^{\frac{\tau_L}{\tau_d}}\right)\left(1-\frac{1}{1-R}R^{\frac{t-\tau_L}{\tau_d}}\right)\right), \quad t \geq \tau_L \tag{5.3}$$

which depends only on the parameters R, d, τ_L and t.

Figure 5.17 contains a series of plots of the amplification factor in this first approximation as a function of time for different reflectances and distances between mirrors. The plots show that the time needed to reach the maximal amplification value increases rapidly with the distance between mirrors and with the mirrors' reflectivity. Supposing a laser pulse time of $\tau_L = 20$ ns and an acquisition time of 1000 ns, and imposing the parameters of the FAMU optical cavity, ie $R = 0.9998$ and $d = 10$ cm [72], Equation 5.3 gives $A(t) = 2239$.

This is of course a rough approximation, and represents the upper limit of the effective amplification factor. Just by taking into account the finite decay rate of the muons, which

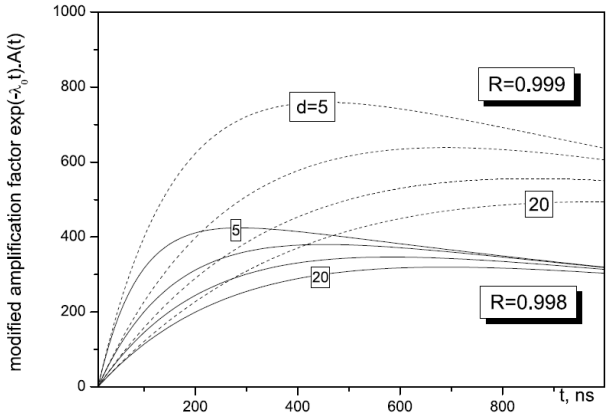

Figure 5.18: Plot of the values of $\exp(-\lambda_0 t)A(t)$ as a function of time for typical values of the reflectance R and of the distance between mirrors d [26]. The laser pulse duration was set to $\tau_L = 20$ ns.

means multiplying $A(t)$ for the factor $\exp(-\lambda_0 t)$, the effective value of $A(t)$ is significantly modified. This can be seen more clearly in Figure 5.18.

Numerous MATLAB simulations were used in order to bring the amplification value as close as possible to the aforementioned upper limit value. The design produced by these simulations is the following [72].

The optical cavity has an illuminated volume equal to $2 \times 2 \times 10$ cm^3. The distance between mirrors was chosen to be 10 cm since this precise distance allows to contain the light inside the cavity without the use of lateral mirrors, thus reducing even more the material placed inside the target.

The main steel support plate sustains a C-shaped structure made of steel, which in turn supports the two mirrors. The laser light enters the cavity through a single ZnS optical window placed outside the pipe that sustains the vessel target. The two fused silica mirrors are coated with a multilayer of ZnS/Ge which provides a reflectivity value greater than 0.9998 for radiation with wavelength equal to 6.78 μm.

The top mirror has cylindrical ends with curvature radius of 54 cm and 17 cm, while the cylindrical ends of the bottom mirror have curvature radius equal to 15 cm and 42 cm. These ends are joined to the central plane piece by a system that consists of a pair of screws and a thin sheet of invar. This sheet both pushes the cylindrical mirror ends on the flat part and minimizes the thermal expansion. The expected gap between the flat part and the cylindrical ends is ~ 15 μm.

Under this configuration the laser light is reflected by the mirror about 1000 times, which results in a cavity photon life of 304 ns and in an equivalent interaction path of 91 m. The estimated size of the surface illuminated by the laser and its reflections is about 2.7×2.2 cm^2.

The light is injected in the multipass optical cavity with a couple of parabolic mirrors. The parabolic mirror system allows to adjust the beam waist at the entrance of the cavity,

and guarantees a stable alignment of the laser with the multipass cavity itself.

5.8 The HPGe detectors

High purity germanium detectors, or HPGe for short, are solid state radiation detectors that are widely employed in X-ray and γ-ray spectroscopy due to their properties. They are composed essentially of a p-n junction, a type of junction which usually can't be used in spectroscopy due to their insufficient maximum depletion depth or active volume.

Silicon and germanium detectors of normal purity, for example, can't reach depletion depths beyond $2 - 3$ mm despite applying bias voltages very close to the breakdown level [58]. The depths required in spectroscopy are instead of the order of 1 cm and more.

The thickness of the depletion region is expressed as

$$d = \left(\frac{2\epsilon V}{eN}\right)^{\frac{1}{2}} \tag{5.4}$$

where V is the reverse bias voltage, N is the net impurity concentration in the bulk semiconductor material, ϵ is the dielectric constant and e is the electronic charge. It can be immediately seen that with the same reverse bias voltage a greater thickness may only be achieved with a lower net impurity concentration.

Techniques have been developed to reduce the value of N in germanium, but not in silicon. There are several reasons for this: one of the most relevant is the difference in the melting point of silicon, 1410 °C against the 959 °C of germanium, which makes the exclusion of impurities in the refining process rather difficult. Nonetheless, the techniques devised for germanium are effective, and reduce the impurity concentration up to 10×10^{10} atoms/cm^3, which corresponds to 1 part in 10^{12} [58]. Detectors built with this technology and with these levels of impurity are called high purity germanium detectors.

In the scope of the FAMU experiment, a system of four HPGe detectors has been developed to support the $LaBr_3$ detectors. These HPGe detectors cover only a small portion of the solid angle and are used for high precision calibration of the detection system and to identify contaminations in the gas mixture, while the actual data acquisition is left to the $LaBr_3$ detection system. The reason behind this choice is the fact that, although the HPGe detectors have better energy resolution compared to the one of the $LaBr_3$ detectors, they are not fast enough to obtain a significant measurement of the number of spin-flip transitions stimulated by the laser in the gas target. Furthermore, in order to work they require liquid nitrogen temperatures.

The HPGe detector system is composed by two Ortec GEM-S [8], one Ortec GLP [4] and one Ortec GMX [5]. The GEM-S detectors are p-type detectors with a semi-planar geometry and a carbon window 0.9 mm thick. Its diameter $\times$ length is 30 mm $\times$ 20 mm. The GLP detector is an n-type detector with planar geometry. It has 16 mm $\times$ 10 mm diameter $\times$ length and a 0.127 mm beryllium window. The Ortec GMX detector is a

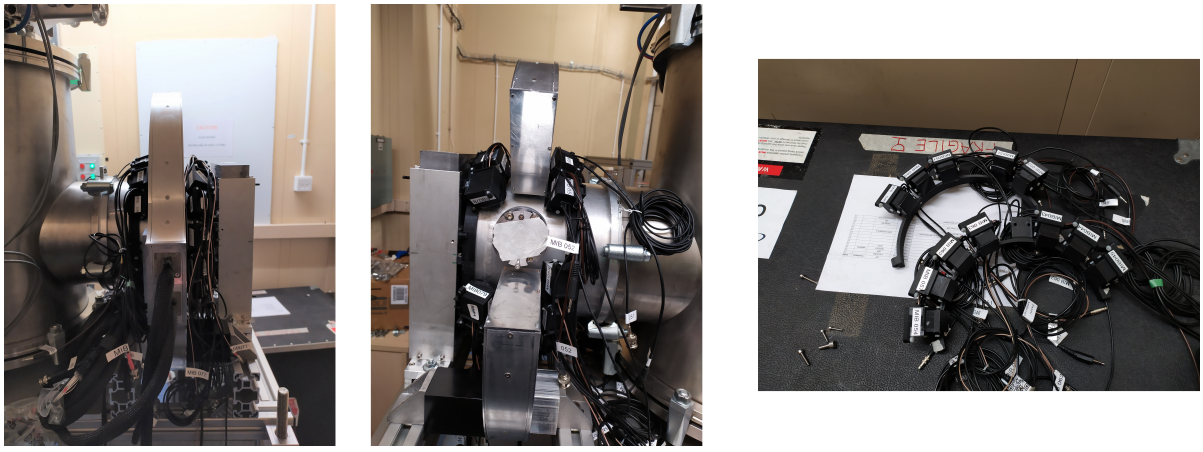

Figure 5.19: Photos of the two auxiliary crowns employed in the FAMU experiment. The image on the left and in the middle show the two crowns mounted around the main crown as seen from the left and from the right side of the beam entrance window. The image on the right shows in more detail the two halves of the crown composed by 12 crystals.

coaxial n-type detector with a 0.127 mm thick beryllium window. It has diameter $\times$ length equal to 54.8 mm $\times$ 49.8 mm [12].

The signals from the HPGe detectors are shaped with a preamplifier and a shaper, and are then sent with a splitter to a CAEN V1724 100 MHz FADC and a Ortec MCB Multichannel Analyzer. The Ortec multichannel analyzer performs a fast online analysis with the Ortec MAESTRO software [7].

5.9 The auxiliary crowns

Two auxiliary crowns, which can be seen in Figure 5.19, have been developed by the Milano Bicocca Division of INFN in order to increase the coverage around the target. These crowns are composed respectively by 10 and 12 $LaBr_3$:Ce^{3+} crystals of size 1/2", which are read by a 4×4 array of 3×3 mm^2 SiPM [12, 35].

With respect to PMTs, SiPMs have a worse rise time (20 ns compared to 10 ns), but the use of smaller crystals and of an array of SiPM compensates for this. The output of each pixel from the 4×4 array of SiPM is summed by a custom PCB. The operating voltages for each detector were set according to the manufacturer's specifications.

Since the crystals are hygroscopic, each of them has been encapsulated in a detector holder realized with a 3D printer.

Chapter 6

The main detector crown

The main detector crown has been designed and built by the Bologna Division of INFN and by the Physics Department of the University of Bologna. This crown is composed by a set of 17 $LaBr_3$ crystals coupled with PMTs.

Usually the most important role in high precision spectroscopy is given to HPGe detectors, but in the scope of the FAMU experiment these are not ideal due to their cost and slow performance. Lanthanum bromide ($LaBr_3$:Ce) represents a good alternative: this type of detector in fact has high effective Z, high density, and fast decay time.

This chapter will cover the characteristics of the $LaBr_3$ detectors and their PMTs, as well as the electrical details of the main detector crown.

6.1 $LaBr_3$ scintillators

In recent years lanthanum bromide detectors have garnered increasing attention in spectroscopy experiments. Their high density ($\rho \sim 5.29$ g/cm^3) and effective atomic number ($\rho Z_{eff}^4 = 25.6 \times 10^6$) make them in fact a valid alternative to more traditional scintillators like sodium iodide NaI(Tl) [84]. Furthermore, their fast decay time of ~ 25 ns and their high energy resolution, equal to 2.8% at 662 keV [17, 84], makes them the ideal choice for experiments were both good resolution and fast luminescence decay are required.

The most common dopant for LaBr crystals is cerium Ce^{3+}. The concentration of this dopant inside the scintillator is a fundamental factor in the choice of the scintillator itself since it affects the spectrum that will be recorded. An example of this characteristic is reported in Figure 6.1.

Although $LaBr_3$:Ce scintillators have several noteworthy qualities, they have also several drawbacks. First of all they are hygroscopic, so much that they're very sensitive to moistening even under vacuum conditions. Secondly, in the $20 - 100$ keV energy range their response isn't proportional to the amount of ionization energy deposited in the

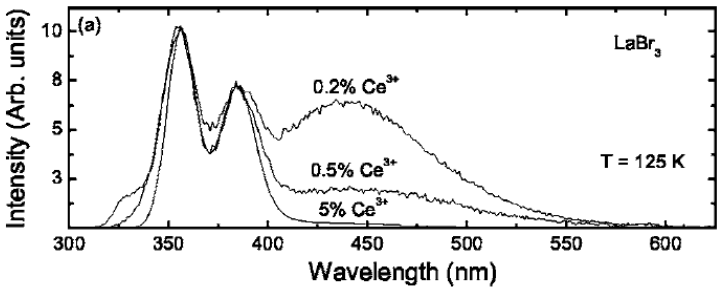

Figure 6.1: X-ray excited emission spectra recorded at 125 K for $LaBr_3$:0.2%Ce^{3+}, $LaBr_3$:0.5%Ce^{3+} and $LaBr_3$:5%Ce^{3+} [30].

scintillator and is affected by temperature [17]. Lastly, they are inherently radioactive and their background may affect the measurements.

The following subsections will describe the main factors that affect the resolution of lanthanum bromide crystals and will give a brief explanation of the aforementioned drawbacks. As for the characteristics of the crystals employed for the crown, they are reported in Table 6.1

Parameters	Value
Height	31.5 mm
Diameter	32.4 mm
Density	5.2 g/cm^3
Wavelength (max emission)	380 nm
Wavelength range	$325 - 450$ nm
Decay times	25 ns
Light yield	$\sim$ 63 photons/keV

Table 6.1: Characteristics of the $LaBr_3$:Ce crystals employed in the main crown.

6.1.1 Energy resolution of $LaBr_3$

The energy resolution of a scintillator coupled with a PMT is defined as the Full Width at Half Maximum ΔE, or FWHM for short, over the energy E of the full absorption peak in a pulse height spectrum. Another possible definition relies on the main factors that affect the resolution itself. These two definitions can be summarized as [17, 57]

$$\left(\frac{\Delta E}{E}\right)^2 = R^2 = R_M^2 + R_{nPR}^2 + R_{inh}^2 + R_{tr}^2 \tag{6.1}$$

In this equation, R_M describes the contribution from the PMT gain and the Poisson statistic behind the number of detected photons. This factor is equal to

$$R_M = 2.35\sqrt{\frac{1 + \text{var}\,(M)}{N_{phe}^{PMT}}} \tag{6.2}$$

where var(M) is the fractional variance in the PMT gain and N_{phe}^{PMT} is the number of photoelectrons produced in the PMT by the scintillation photons generated by the crystal. The so-called fundamental limit of Equation 6.2 is obtained when var(M)= 0, and corresponds to $R_{ndp} = 2.35/\sqrt{N_{phe}^{PMT}}$ [17].

The other terms in Equation 6.1 from left to right refers in order to the contribution from the non-proportional response of the scintillator, from the inhomogeneities of the crystal and from the transfer of the scintillation photons from the crystal to the PMT.

Alekhin *et al.* [17] performed a measure of the resolution terms in Equation 6.1 using a PMT with fractional variance of 0.27. They measured a Poisson contribution $R_M = 1.7\%$ and a crystal and PMT contribution of $\sqrt{R_{nPR}^2 + R_{inh}^2 + R_{tr}^2} = 1.8$ at 662 keV, with a total resolution of $R = 2.5\%$.

Figure 6.2 shows the energy resolution R at 662 keV measured for $LaBr_3$:Ce detectors in another experiment by Alekhin *et al.* [17] and the resolution of more traditional scintillators. It can be seen that the resolution of $\sim 2.7\%$ of lanthanum bromide at 662 keV that was measured in this second experiment is significantly lower than that of other crystals, thus making $LaBr_3$ an ideal choice when both fast decay time and high precision are needed.

6.1.2 Non-proportionality issues

A scintillator is affected by non-proportionality when its total light output is not proportional to the energy of the absorbed photon. The non-proportional response in lanthanum bromide crystals originates from the stochastic nature of the ionization track inside the crystal itself.

An incident photon interacting with a scintillator generates either a hole and a high-energy electron due to the photoelectric effect, or multiple holes and high-energy electrons due to a series of Compton scattering events. These primary electrons pass through the scintillator leaving behind ionization tracks. Secondary high-energy electrons freed during the collisions can also generate their own ionization tracks. These electrons are then captured inside the scintillator, they recombine with the holes and generate photons that are read by the PMT.

In an ideal case, the total energy that arrives at the PMT is exactly the same of the original incident photon. In the real case however there are several electron-hole recombination losses during the scintillation process described above, which means that

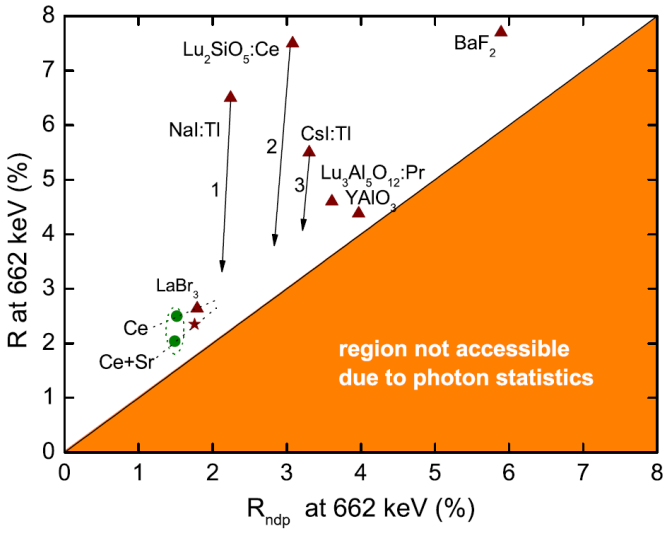

Figure 6.2: Energy resolution of traditional scintillators and of $LaBr_3$ at 662 keV energy with ordinary bialkali PMT readout against the fundamental limit R_{ndp} [17]. The encircled data points refer to resolutions obtained with a Hamamatsu super bialkali R6231 – 100 PMT. The arrows denote potential improvements.

the total energy read by the PMT is not the same as that of the original photon. This issue is the cause of non-proportionality [17, 56].

The reason behind the electron-hole recombination losses is still unknown, but it is currently believed that the losses occur in the part of the ionization tracks where the ionization density is particularly high [56].

Figure 6.3 shows the different non-proportional response of a $LaBr_3$:Ce scintillator kept at three different temperatures, which are 80 K, 295 K and 450 K. The tracks indicate that the non-proportionality of lanthanum bromide, ie the electron-hole recombination losses, have a strong dependence on the temperature of the crystal itself. Furthermore they show that the non-proportionality represents an issue in the $20 - 100$ keV energy range.

6.1.3 The intrinsic radiation of $Labr_3:Ce^{3+}$ crystals

The intrinsic radiation of the $LaBr_3$ crystals is caused by the decay of lanthanum and actinium. Lanthanum in fact has a radioactive isotope, ^{138}La, which is naturally occuring with an abundance of 0.09% and a half-life of 1.05×10^{11}. This isotope affects the spectrum for energies below 1.5 MeV.

As shown in Figure 6.4, ^{138}La decays in two parallel processes [40, 64]. In the first one, about 34.4% of the isotope undergoes β^- decay with energies up to 263 keV and produces ^{138}Ce in its first excited state. This state de-excite to the ground state through

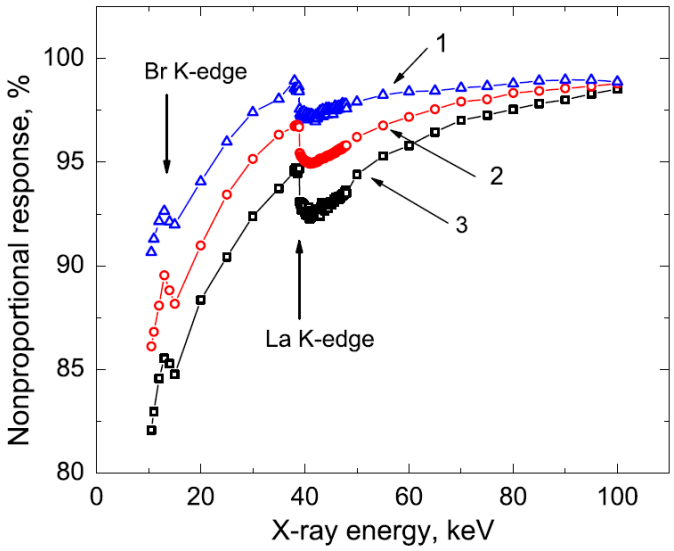

Figure 6.3: Non-proportional response of a $LaBr_3$:Ce crystal as a function of X-ray energy for the three scintillator temperatures 80 K, 295 K and 450 K [56].

the emission of a 788.742 keV γ-ray. The remaining 65.6% of the lanthanum radioactive isotope disintegrates by electronic capture and produces stable ^{138}Ba. This event is associated with the emission of a γ-ray with energy equal to 1435.795 keV and with the emission of characteristic X-rays of Ba with energies between 31 and 38 keV.

^{227}Ac is part of the ^{235}U decay chain. Due to its chemical similarity to lanthanum, actinium is present as a contaminating element inside $LaBr_3$ crystals with a half life of 21.77 years [40]. The first commercially available lanthanum bromide crystals had a contamination level of 1.3×10^{-13} ^{227}Ac atoms/La atoms, but nowadays this factor has been reduced by over two orders of magnitude [64].

The decay chain of ^{227}Ac down to the stable ^{207}Pb is reported in Figure 6.5. It can be seen that the decay chain includes six α emitters, namely ^{227}Ac, ^{227}Th, ^{223}Ra, ^{219}Rn, ^{215}Po and ^{211}Bi, and four β emitters, which are ^{227}Ac, ^{211}Pb, ^{211}Bi and ^{207}Tl. The actinium decay chain contributes to the β continuum up to $\sim$ 1400 keV due to the β decay of ^{211}Pb and ^{207}Tl. The α particles produced by the α emitters affect instead the region of the energy spectrum that goes from 1800 to 2500 keV.

The natural spectrum produced by the intrinsic radiation of a $LaBr_3$ scintillator is shown in Figure 6.6.

The first low-energy peak, centered at $\sim$ 35.5 keV, is given by the sum of 95.6% of the 31.83 keV K_α X-rays, which are emitted during the electron capture decay of ^{138}La, with 90% of the 5.6 keV Auger electrons generated in the same process. Its energy is actually shifted due to the nonproportionality of the lanthanum bromide crystals.

The first peak is followed by the β continuum with an end point of 263 keV. The β

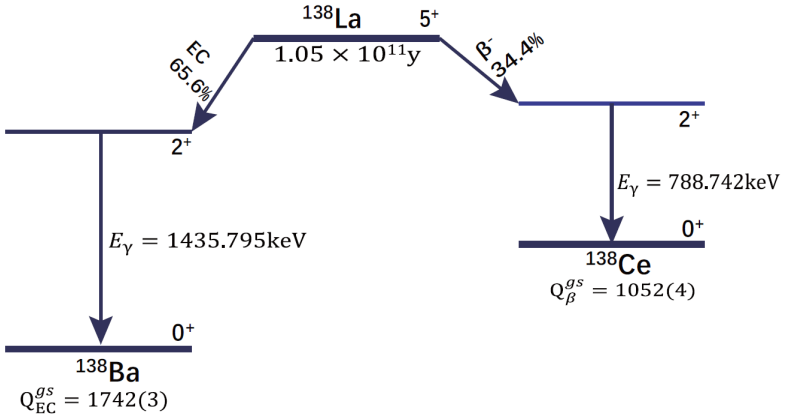

Figure 6.4: Decay scheme of ^{138}La [40].

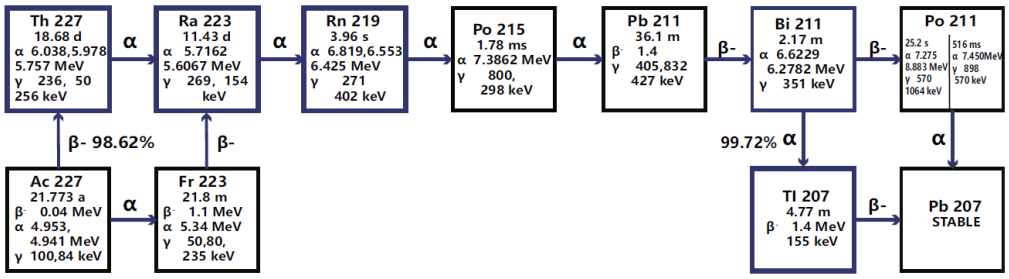

Figure 6.5: Decay scheme of ^{227}Ac [40]. Each nuclide has its own list that includes its half life, the energies of its emitted α particles, its characteristic high intensity γ-rays, and its β decay end point.

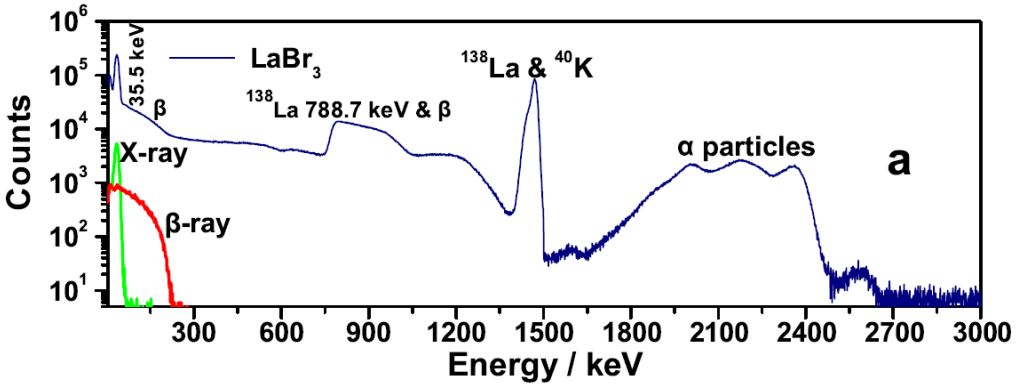

Figure 6.6: Intrinsic radiation of a $LaBr_3$:Ce crystal measured in 37.187 seconds [40]. The β continuum is shown in red, while the first low-energy X-ray spectrum is shown in green. More details about these two components can be found in the text.

continuum is actually mixed with the Compton continuum, which comes mainly from the 788.7 and 1435.8 keV γ-rays from ^{138}La and the 1460.8 keV of ^{40}K.

The 788.7 keV peak of ^{138}La extends up to 1 MeV due to the coincidence of this γ-rays with the β continuum.

The double peak present in the center of the spectrum is caused by the 1435.8 γ-rays of the ^{138}La electron capture decay and by the 1460.8 keV γ-rays of ^{40}K. The double peak is slightly shifted towards 1461 keV due to the fact that these events coincided with a portion of the 32 keV X-rays of ^{138}Ba during acquisition.

The spectrum above 1.5 MeV reveals the presence of the α emitter contaminants through the presence of the triple peak generated by the α particles of the ^{227}Ac decay chain. Although the α energies from the ^{227}Ac decay chain should be in the range $5.0 \sim 7.4$ MeV, as reported in Figure 6.5, the energies of the spectrum shown in Figure 6.6 have been calibrated with γ-rays to be in the range $1.5 \sim 2.5$ MeV due to the light quenching effect [40].

Since the majority of these intrinsic γ-rays and X-rays exceeds the energy range of interest for the FAMU experiment for which the detectors and the PMTs are calibrated, the detection of one of them oftentimes results in a saturation of the acquisition system.

6.2 The electronics of the detector crown

The main detector crown is composed by seventeen $LaBr_3$ crystals coupled with a set of HAMAMATSU R11265U-200 PMTs [6], as can be seen in Figure 6.7. The parameters describing the PMT are recorded in Table 6.2, while the block scheme of the electronics that manages the detector crown is shown in Figure 6.8. It can be seen that the block scheme can be divided into three sections: from upper to lower, they describe the high voltage feedback system, the data handling circuitry and the detectors' management system.

Parameters	Value
Spectral range	$300 - 650$ nm
Peak wavelength	400 nm
Supply voltage between anode and cathode	1000 V
Quantum efficiency	43%

Table 6.2: Characteristics of the HAMAMATSU R11265U-200 PMTs [6]

The components of the detector crown needs several different voltages in order to work. The first group of voltages will be collectively referred to as low voltages, and it includes +2.5 V, ±5 V and ±15 V. Other voltages required are the middle voltage (MV) and the high voltage (HV). The former ranges from −200 V to −350 V, the latter from

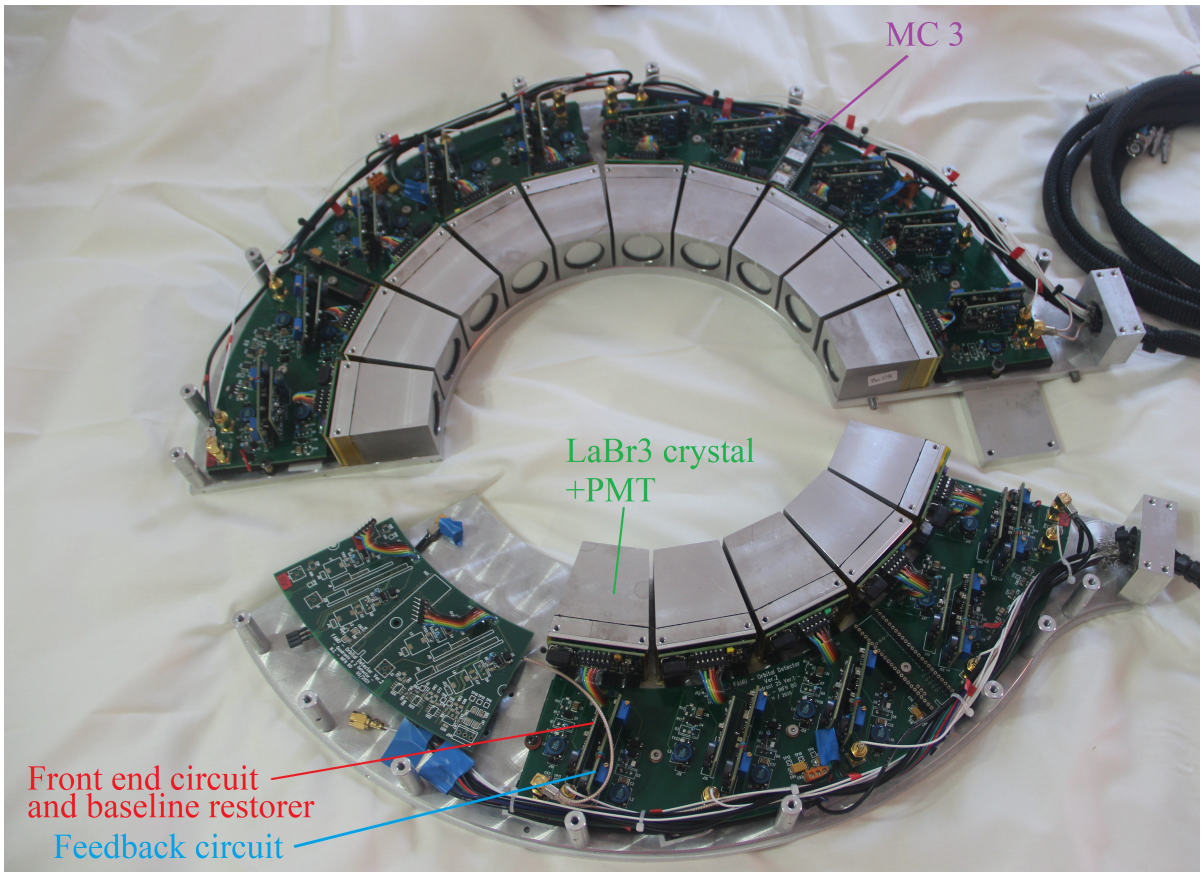

Figure 6.7: Photo of the main detector crown taken during assembly. Due to technical problems, when the photo was taken two detectors were missing. It's possible to see the microcontroller #3 (MC 3), as well as the main components of the electronics employed for each detector: the $LaBr_3$ crystal and PMT (green), the feedback circuit (blue) and the front end circuit with the baseline restorer (red). More details in text.

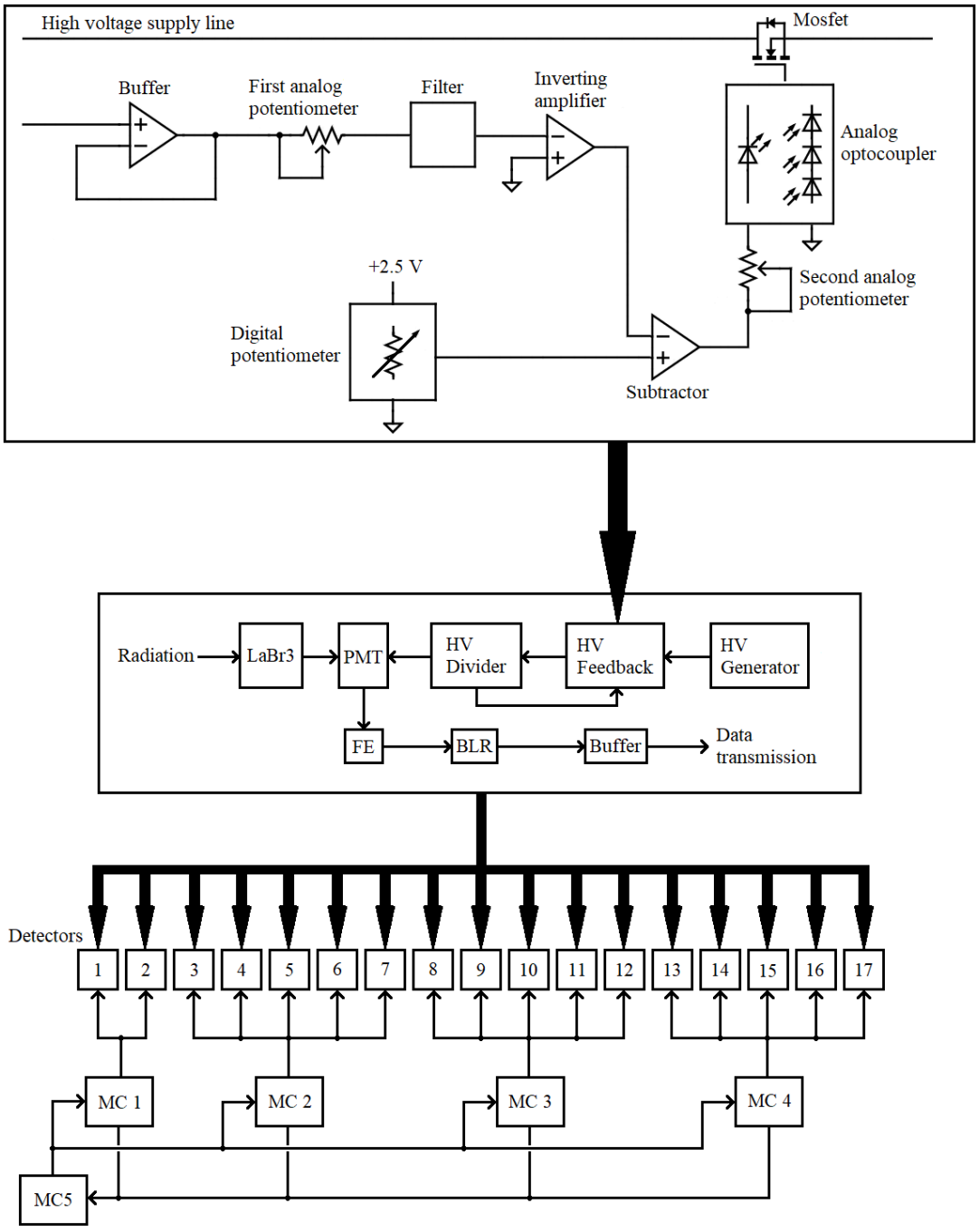

Figure 6.8: Block scheme of the electronics behind the detector crown. The upper block shows the components of the high voltage feedback system, the middle block describes how the signal from each PMT is handled, and the lower section shows the microcontrollers and the detectors that they manage. More details in text.

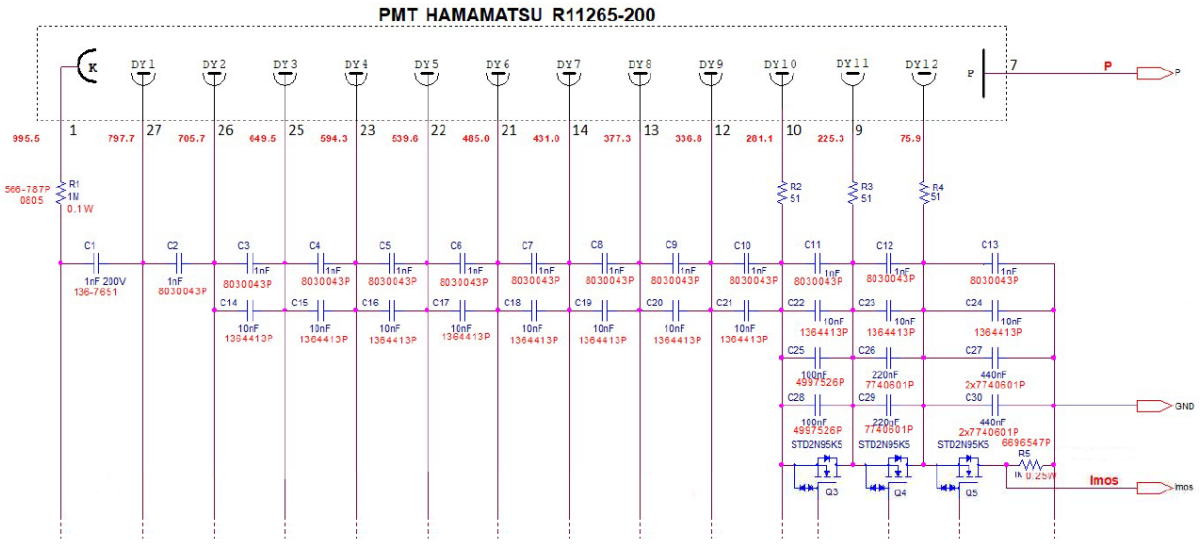

Figure 6.9: Capacitors and MOSFETs employed in the HV divider in order to keep the PMT powered during the whole acquisition. More details in text.

−760 V to −950 V. A specific high voltage generator is employed to produce and supply the machine with the required HV.

6.2.1 High voltage divider and PMT signal transmission

The role of the detector crown is to detect and convert into electrical signal the X-rays emitted by muonic oxygen during de-excitation. Consider a single scintillator crystal and its PMT. When an X-ray photon enters the $LaBr_3$ crystal, it causes the production of scintillation light which is then detected by the PMT glued to the crystal. The PMT then generates electrons through photoelectric effect which multiply in number with each dynode of the PMT itself.

These dynodes are powered by the HV and kept at constant voltage by a custom made voltage divider, denoted by HV Divider in Figure 6.8, which was built specifically to handle a high rate of events. This voltage divider is coupled with four rows of capacitors and a row of MOSFETs, which are reported in Figure 6.9.

The first row is composed by very fast ceramic capacitors. While the electrons cross the PMT and multiply, these capacitors act as local reservoirs of charge: they in fact supply the PMT dynodes when needed in order to keep their voltage constant. These components, although very fast, have also a rather small capacitance which means that they can hold only a limited charge.

In case of high event rate these capacitors alone cannot handle the role of reservoirs. For this reason, three more rows of capacitors have been added. The second row contains

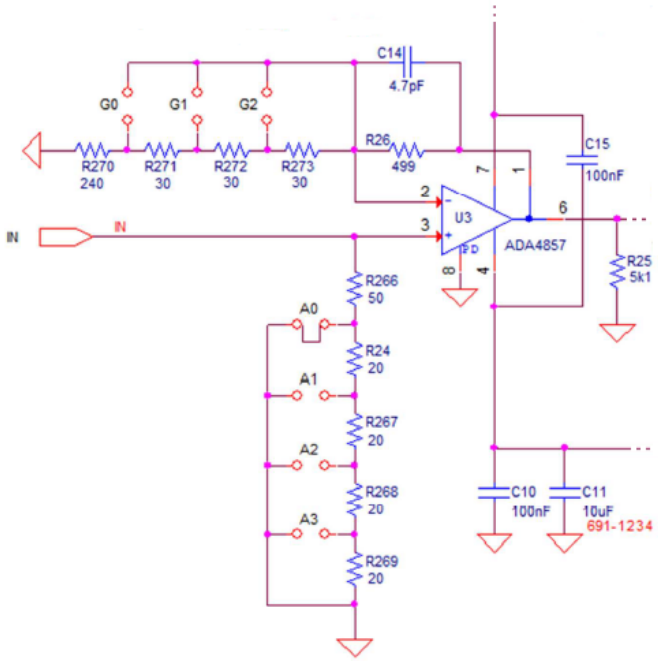

Figure 6.10: Wiring diagram of the front end circuit employed in the detector crown. More details in text.

capacitors with intermediate capacitance and speed, while the third and fourth ones are composed by slow but high capacitance components.

Since the estimated number of events is 3×10^6 events per second, with possible spikes of 5×10^6 events per second, a final row of MOSFETs has been included as a security measure. These MOSFETts, which are powered by the MV, have a fast response time of 4 ns which allows them to take immediate action in case the whole chain of capacitors can't handle the strain.

This supply chain ensures that each PMT is able to successfully and continuously produce an electrical signal dependent on the energy of the detected photons. The signal generated by the PMT is sent to the front end circuit (FE), shown in Figure 6.10, which consists in a current-voltage converter. The FE is built around an high quality operational amplifier with a bandwidth of 750 MHz capable of handling the huge number of expected events.

This component is followed by a baseline restorer (BLR), whose role is to cut the latter part of the decay curve of the PMT signals. The high event rate in fact guarantees the presence of pile-up events. These events not only may lead to wrong energy measurement, but may also increase the time required for the decay curve to reach the baseline. By cutting the last negligible part of the signal's decay curve it's possible to avoid the change in the baseline value and therefore in the impulse measured energy. The BLR is composed

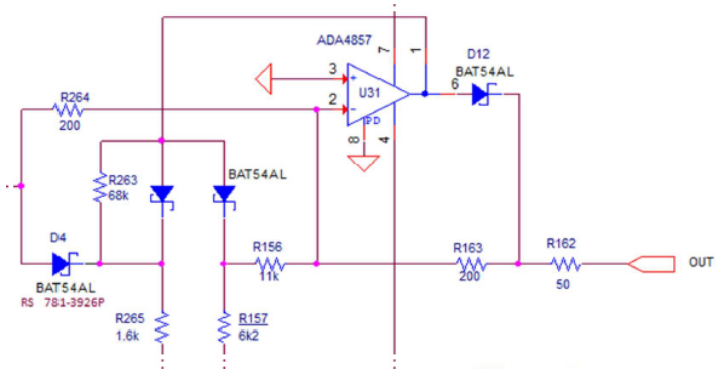

Figure 6.11: Wiring diagram of the baseline restorer and of the buffer connected to it. More details in text.

by four fast Schottky diodes with a gap of ~ 0.3 V.

These diodes are also connected to an operational amplifier acting as a buffer that preserves the signal's amplitude. The cable that connects the crown to the rack containing the digitizers is in fact 4 m long and without the buffer the signal would not reach its destination. The BLR and the buffer are shown in Figure 6.11.

6.2.2 High voltage feedback circuit

A fluctuation in the value of the HV would mean a fluctuation in the gain of the PMT and therefore a broadening of the X-ray peak in the spectrum. To avoid this, the HV is constantly kept in check using a feedback system (HV feedback) able to readjust its value in real time.

More precisely, at all times the current that passes through the HV divider is sent to a high impedance buffer, which guarantees that the voltage divider isn't affected by the presence of the feedback circuit.

An inverting amplifier, whose gain is determined by a first analog potentiometer, inverts the voltage read from the buffer and makes it positive. Two capacitors get rid of the high frequency noise that originates from the voltage divider by filtering frequencies higher than 15 kHz. The first potentiometer, the capacitors and the inverting amplifier can be seen in Figure 6.12.

The output signal of the inverting amplifier, which is proportional to the current flowing in the voltage divider and therefore to the HV that supplies it, is sent to the inverting pin of a subtractor.

The non-inverting pin of the subtractor is connected to a digital amplifier with an output that ranges from 0 to +2.5 V. This amplifier is managed directly and in real time through a LabVIEW software.

Given the output of the digital amplifier in the non-inverting pin, and the output

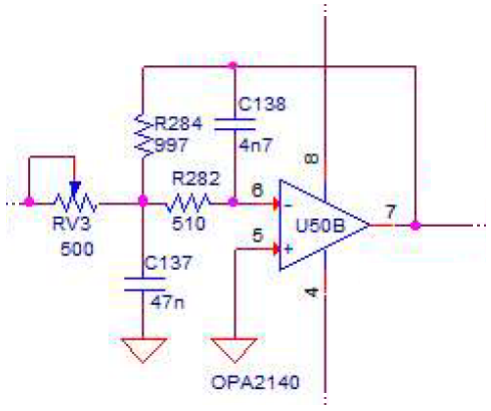

Figure 6.12: Wiring diagram of the first analog potentiometer and of the inverting amplifier that is driven by it. The two filtering capacitors are also shown. More details in text.

of the inverting amplifier at the positive pin, the subtractor sends their difference to a second analog potentiometer which is followed by an analog optocoupler.

The optocoupler has been built specifically for MOS gate drive applications [2] and contains a LED and an array of photodiodes connected in series. The higher the voltage received by the LED, the more light it produces and the higher the voltage generated by the photodiodes.

The output voltage of the analog optocoupler supplies the gate of a MOSFET placed along the supply line of the voltage divider. This MOSFET can directly alter the HV depending on the voltage arriving at its gate.

Figure 6.13 shows this latter part of the feedback circuit.

For the sake of clarity, consider the case in which the high voltage value is temporarily increased due to a current fluctuation. An increased value of the high voltage implies a higher voltage arriving at the inverting pin of the subtractor. Since the output of the digital potentiometer is to be kept constant during the experiment, this increase means that the subtractor produces a lower output. This output is sent to the optocoupler, whose LED, receiving a lower voltage, generates a reduced amount of light. As a consequence, the photodiode array produces a lower voltage, which directly affects the MOSFET by forcing it to promptly decrease the high voltage supply by an amount proportional to the initial fluctuation. The case for a fluctuation that reduces the high voltage value is specular.

The presence of the analog optocoupler is fundamental since it allows to fine tune the HV value in real time. Furthermore, it acts as a galvanic separation unit between the HV feedback circuit and the HV supply line.

As for the three potentiometers, they are used to manage the feedback itself: the first analog potentiometer, located after the initial buffer in the feedback circuit, sets the gain of the inverting amplifier, that is it determines the proportionality constant between the

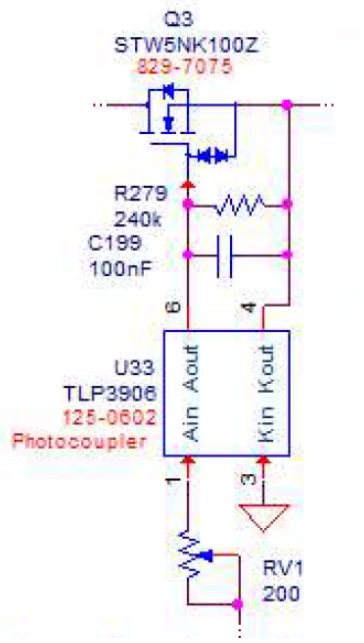

Figure 6.13: Wiring diagram of the second analog potentiometer, of the analog optocoupler, and of the MOSFET placed along the HV supply line. More details in text.

HV value and the voltage effectively arriving at the inverting pin of the subtractor. The second analog potentiometer is what determines the exact value of the HV.

The digital potentiometer that feeds the non-inverting pin of the subtractor is employed for finer corrections: once the two analog potentiometers have been set and the detector crown has been closed, this component can be driven by computer to change the HV value in small steps right before the experiments.

It's important to notice that the HV feedback is significantly slower than other smaller feedback systems in the electronics so that they won't interfere with each other.

6.2.3 Microcontrollers and detectors management

The components described in the two previous subsections are implemented for each of the 17 detectors that compose the main crown. In other words, each crystal has its own PMT, its own HV divider and feedback and its own front end and baseline restorer.

As a consequence, although the HV generator provides the same voltage to all detectors, the actual voltage received by each detector is up to its own feedback system.

A set of Teensyduino 3.5 [11], programmed with the Arduino IDE plus the Teensyduino add-on, is employed to manage each detector. In this setup they act as microcontroller (MC) of the electronics. More precisely, they manage the sending of signals to and from the detectors, and allow the user to modify the value of the digital potentiometer using

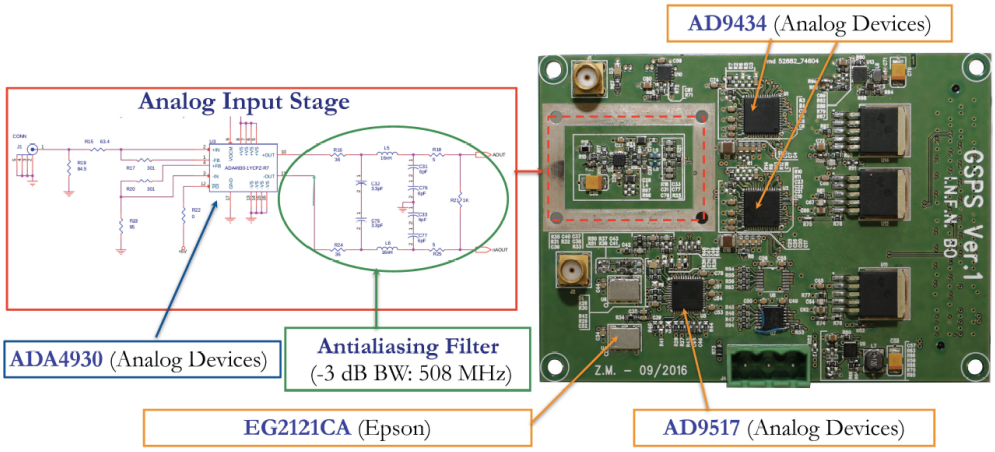

Figure 6.14: Wiring diagram and picture of the first version of the GSPS [83].

the LabVIEW software.

The detectors are divided into four groups according to the microcontroller that drives them. As shown in Figure 6.8, all groups have five detectors except the first one, which has a smaller size due to the physical constraints of the experimental apparatus.

These four microcontrollers measure the effective high voltage value that powers each detector and send it to a fifth microcontroller, whose task is to relay information from the crown to the user.

6.2.4 GSPS

A custom fast continuous sampling digitizer has been designed to withstand the high event rate of the $LaBr_3$ crystal. The digitizer, named GSPS, is under construction under the Bologna Division of INFN and the Physics Department of the University of Bologna. Although the board and its components are still under development, a fully functioning prototype has been completed.

The first version of the GSPS digitizer, reported in Figure 6.14 was composed by two Analog Devices AD9434 ADCs [1] running at 500 MS/s with opposite clock phase connected in a timing interleaved architecture [83]. Time interleaving is a technique that allows the use of multiple identical ADCs to process data at a faster rate than the operating sample rate of each individual ADC. With this technique the two ADCs were able to manage continuous data sampling up to 1 GS/s, and thus allowed to perform on-line data processing.

This version of the GSPS was hosted by a 6- layers PCB, FMC-form mezzanine card. Its ADC had a 12-bit resolution, with a typical input range of 1.5 V_{pp} and an effective number of bits, or ENOB for short, of 10.5. Its SNR was equal to 65 dBFS.

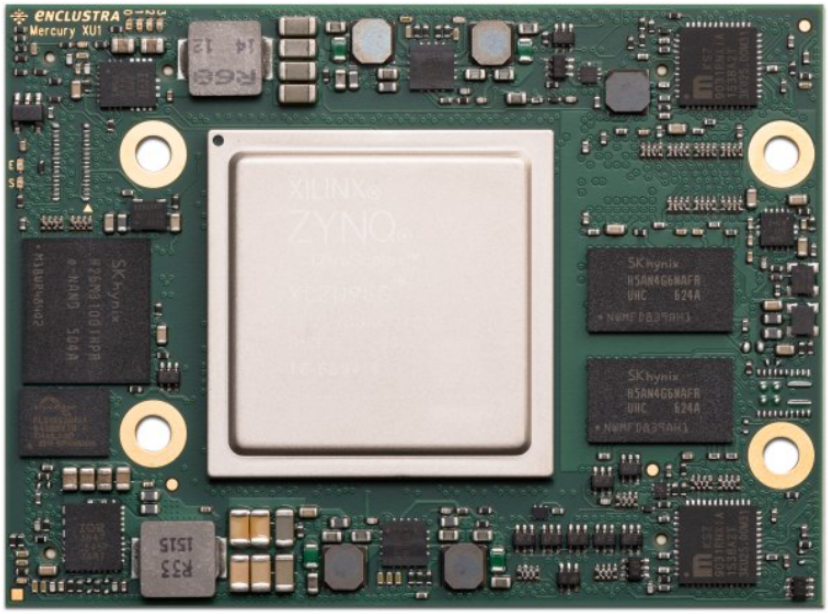

Figure 6.15: SOM employed for the GSPS digitizer [3].

The second and current version of the GSPS shows great improvement compared to the first one. First of all, the digitizer is not implemented on a FMC mezzanine card anymore, but on a motherboard hosting a FPGA, four ADCs, the powering and the clock of the board [27].

The FPGA is placed on a System-On-Module, or SOM, shown in Figure 6.15. The chosen SOM is the Mercury+ XU1 system-on-chip module from Enclustra, which has several peripherals already built in, like ethernet PHY, USB PHY, DDR memory and non volatile memories. Since the FPGA that the SOM contains may overheat, a fan has been glued on top of it.

The model of the FPGA implemented on this SOM is the Xilinx Ultrascale+ Zynq FPGA (MPSoC) which allows both to implement heavy digital signal processing and to manage high bandwidth external connections.

Each ADC implemented on the GSPS is a 14-bit Analog Device AD9684 with two input channels, each sampling at a rate of 500 MS/s. The effective rate at which the four ADCs acquire depends on separate cards called Analog Mezzanines: these are cards which host the majority of the analog components. According to the Analog Mezzanine configuration, the ADCs may acquire data from 8 input channels sampled at 500 MS/s with no interleaving to a maximum of 1 channel sampled at 4 GS/s [27].

For the scope of the FAMU experiment the GSPS uses 4 Analog Mezzanines that acquire 4 input channels with a 1 GS/s sampling rate in interleaved mode. Each channel has its own amplifier and anti-aliasing filter. The output of the mezzanines is doubled and routed to two inputs of the motherboard connected to the ADCs. Since the ADC

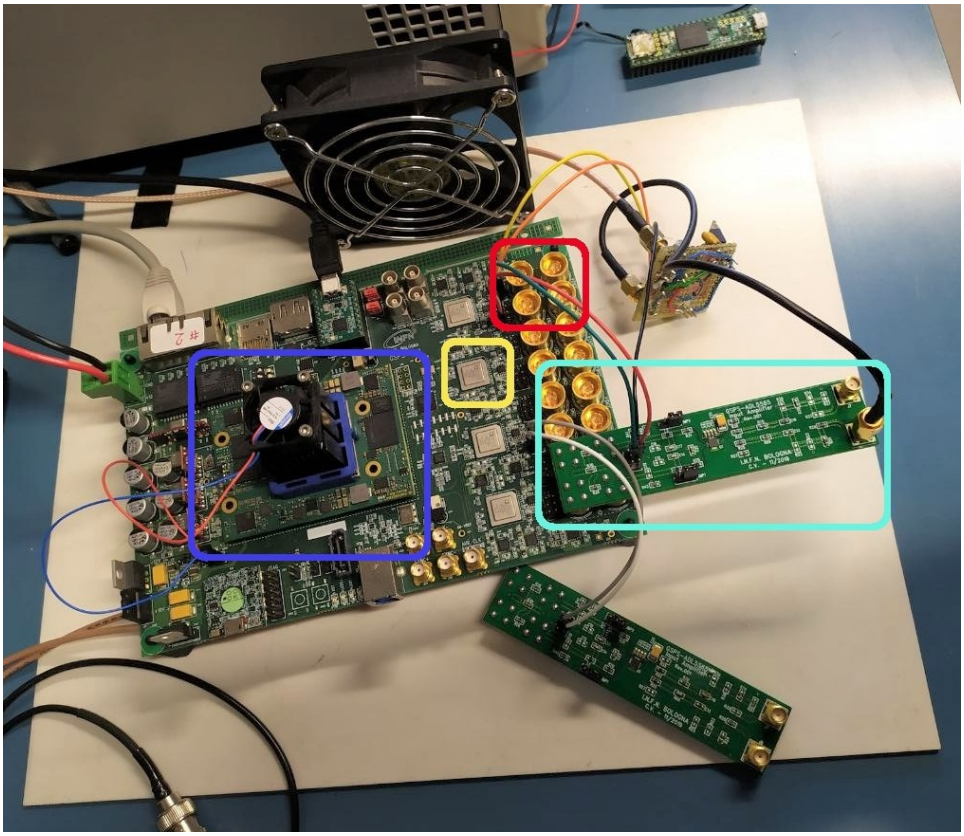

Figure 6.16: Photo of the second and current version of the GSPS digitizer. The blue box contains the SOM and the FPGA, which are not directly visible due to the fan glued on top. The yellow box shows one of the four ADCs, while the red one shows two of the eight input channels available to the board. The last box, the light blue one, contains one of the two ready Analog Mezzanines.

may also overheat, a fan has been placed in front of them. In this configuration the ENOB of the board is 12, a significant improvement compared to the 10.5 of the previous version. The second version of the GSPS is shown in Figure 6.16.

Since each motherboard uses four channels in the configuration employed in the FAMU experiment, it follows that one board can cover only four detectors, and that each detector requires its own Analog Mezzanine. Currently only two Analog Mezzanines and one GSPS board are available.

The software used to interact with the GSPS has been built on Linux using C++. Through this program its possible to set the parameter of each acquisition, which are: the channel from which the data will be acquired, the trigger value, the delay time of the acquisition, the number of events to record and the samples per event. Each event of the acquisition is saved in $.md5$ format.

Since the computer that manages the detectors and the GSPS has a Windows operating system, in order for this software to work it must be accessed through Cygwin, a collection

of GNU and Open Source tools which allows to have functionalities similar to those provided by Linux on Windows.

6.3 Calibration and testing of the crown

Each detector of the crown has been calibrated to guarantee an optimal overlap of their X-ray peak. By maximizing the overlap of the peaks it's in fact possible to reach a signal to noise ratio higher than that of the single peaks.

The calibration has been performed by placing each detector directly in front of a ^{137}Cs source and by measuring the spectrum produced by the apparatus. A small lead shielding was placed next to the radioactive source in order to decrease as much as possible the researchers' absorbed dose. The middle voltage was set to -303 V, the high voltage to -950 V.

For each detector tested, the acquisition time window spanned 30 minutes. Furthermore, since temperature is an issue of $LaBr_3$, the apparatus was left active for more than 40 minutes before the acquisition started in order to let it reach a stable working temperature. The crown was left open during the full acquisition.

The detectors were calibrated by tuning the value of the three potentiometers in the feedback circuit so that the amplitudes of the waveforms produced by each detector were the same. These amplitudes were observed on an oscilloscope, as shown in Figure 6.17, and their value was kept a little below 1 V in order to avoid saturation. It was observed in fact that for signals equal or higher than 1.2 V the GSPS saturates.

The actual overlap of the photopeaks was checked using the spectra produced by the GSPS, which were also used to measure the resolution of each detector.

More precisely, the data in *.md5* format generated by the GSPS were analyzed and used to compute the spectra of the radiation detected by the equipment with a MATLAB software. The spectra were then fitted using a gaussian distribution and the parameter of the fits were used to calculate the FWHM and the position of the photopeaks.

It's important to notice that MATLAB does not directly give the standard deviation of the gaussian distribution. The parameterization employed by the MATLAB software used was in fact

$$f(x) = \frac{1}{\sqrt{2\pi\sigma^2}} \exp\left(-\frac{(x-\mu)^2}{2\sigma^2}\right) = a \exp\left(-\frac{(x-b)^2}{c^2}\right) \tag{6.3}$$

which implies that $b = \mu$ and $c = \sqrt{2}\sigma$. The FWHM was therefore calculated as

$$FWHM = 2\sqrt{2\ln 2}\sigma = 2\sqrt{\ln 2}c \tag{6.4}$$

and the resolution as

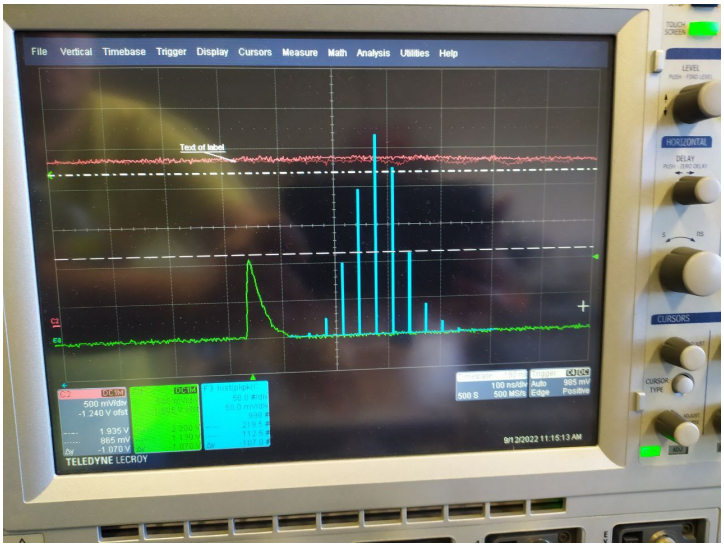

Figure 6.17: Waveform generated by the oscilloscope during acquisition. The blue histogram shows the energy spread of the detected events. The red line represents the HV value arriving at the voltage divider described in Subsection 6.2.1. The white dashed line has been placed at 1.2 V and represents the voltage that the waveforms must not reach.

$$R = \frac{FWHM}{\mu} \cdot 100 \tag{6.5}$$

6.4 Results

The results obtained from detector 3 to 13 are reported in Table 6.3, while the spectra measured by these detectors be seen in Figure 6.18 and Figure 6.19. The total spectrum, given by the sum of all spectra in Figure 6.18 and 6.19, is reported in Figure 6.20.

In all measured spectra it's possible to identify the photopeak of the 662 keV γ-ray produced by ^{137}Cs. The three peaks in the Compton continuum are, from left to right, the peak given by the low energy X-rays emitted by lanthanum decay, the backscatter peak and the Compton edge.

The resolutions reported in Table 6.3 show that the detector crown has still room for improvement: all of them in fact are rather different from the $\sim 2.5\%$ found in literature.

This discrepancy originated from a shifting in the signals' amplitude: a detailed analysis of the data in fact showed a slow decrease in the amplitudes as the acquisition went on.

Some detectors, like detector 10, 11 and 12, were able to maintain a good hold on the amplitude values. As can be seen in Figure 6.19b, 6.19c and 6.19d, in fact, their spectra show a unique and pronounced photopeak with a FWHM narrower than that of the other

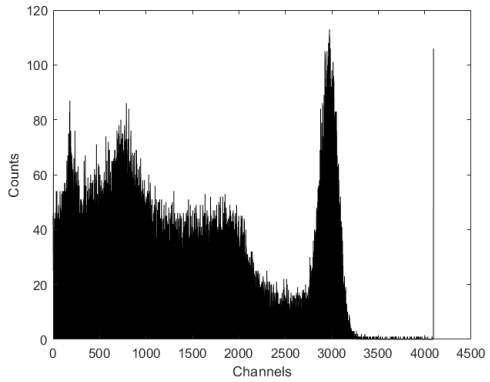

(a) Spectrum of detector 3.

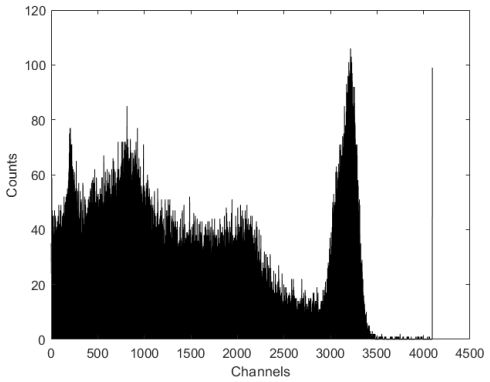

(b) Spectrum of detector 4.

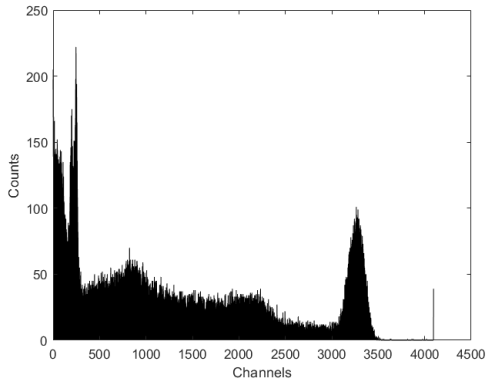

(c) Spectrum of detector 5.

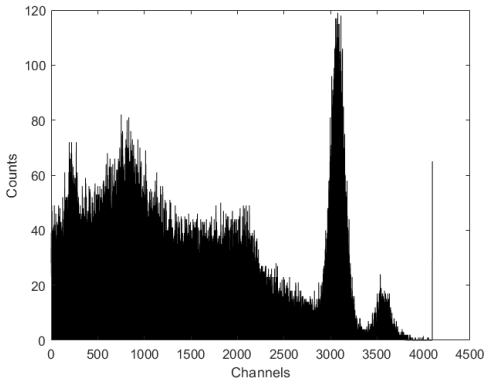

(d) Spectrum of detector 6.

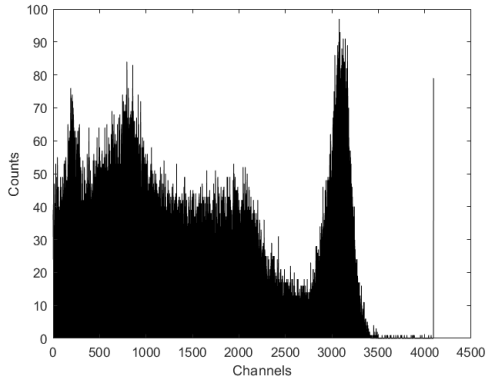

(e) Spectrum of detector 7.

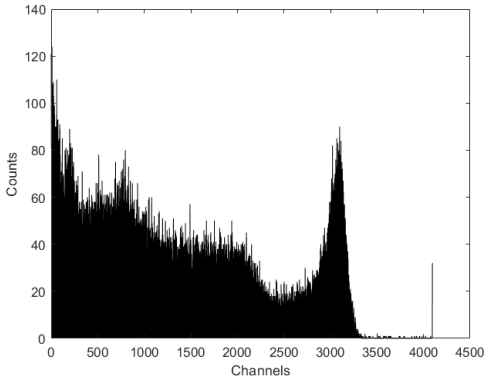

(f) Spectrum of detector 8.

Figure 6.18: Spectra acquired during testing.

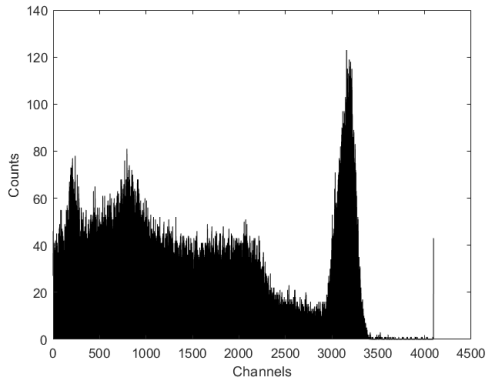

(a) Spectrum of detector 9.

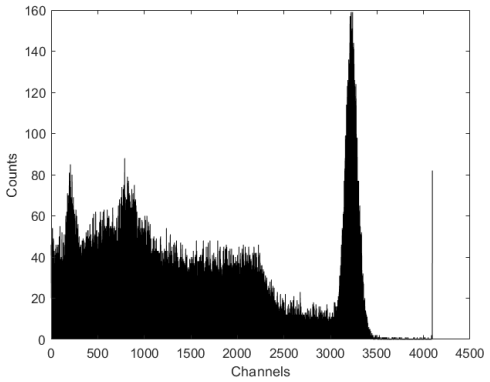

(b) Spectrum of detector 10.

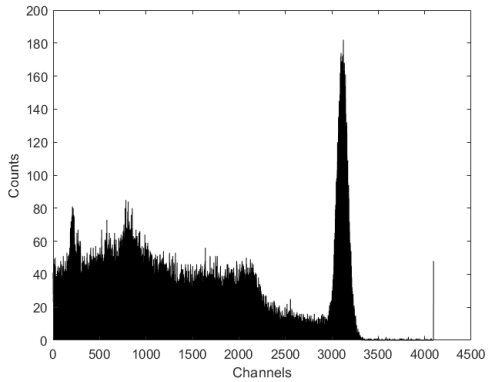

(c) Spectrum of detector 11.

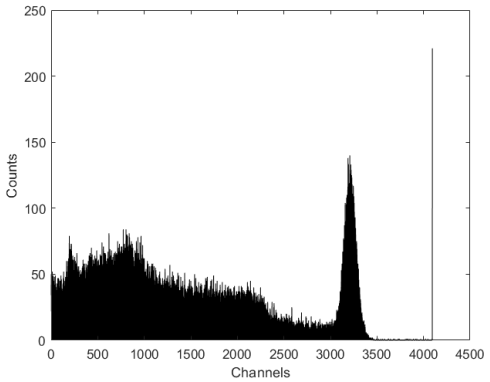

(d) Spectrum of detector 12.

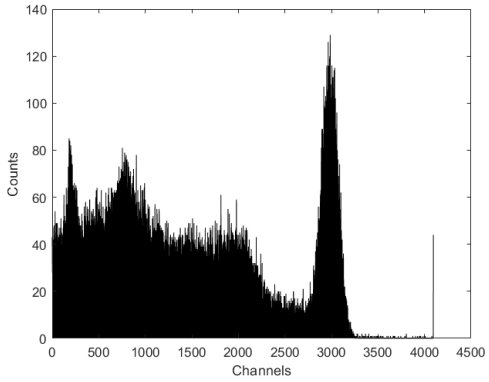

(e) Spectrum of detector 13.

Figure 6.19: Spectra acquired during testing.

#Detector	μ (ch)	c (ch)	σ (ch)	FWHM (ch)	Resolution (%)
3	2966 ± 2	141.8 ± 3.0	100.27 ± 2.12	236.11 ± 5.00	7.96 ± 0.17
4	3182 ± 3	156.1 ± 3.7	110.38 ± 2.62	259.92 ± 6.16	8.17 ± 0.20
5	3264 ± 2	123.3 ± 3.1	87.19 ± 2.19	205.31 ± 5.16	6.29 ± 0.16
6	3076 ± 2	111.2 ± 2.5	78.63 ± 1.77	185.16 ± 4.16	6.02 ± 0.14
7	3083 ± 3	175.0 ± 4.2	123.74 ± 2.97	291.39 ± 6.99	9.45 ± 0.24
8	3053 ± 4	160.9 ± 5.7	113.77 ± 4.03	267.92 ± 9.49	8.78 ± 0.32
9	3157 ± 3	138.0 ± 3.4	97.58 ± 2.40	229.79 ± 5.66	7.28 ± 0.19
10	3225 ± 2	94.1 ± 2.1	66.54 ± 1.48	156.69 ± 3.50	4.86 ± 0.11
11	3114 ± 1	82.5 ± 1.7	58.34 ± 1.20	137.37 ± 2.83	4.41 ± 0.09
12	3211 ± 2	93.4 ± 2.1	66.04 ± 1.48	155.52 ± 3.50	4.84 ± 0.11
13	2981 ± 2	129.0 ± 2.8	91.22 ± 1.98	214.80 ± 4.66	7.21 ± 0.16
Sum	3112 ± 3	208.8 ± 4.4	147.64 ± 3.11	347.67 ± 7.33	11.17 ± 0.25

Table 6.3: This table reports the results of the gaussian fit performed on the data acquired by detectors 3 to 13 and the resolutions extrapolated from them. The last row refers to the results acquired from the sum of all spectra.

detectors.

Figure 6.18d shows instead the opposite case: for detector 6 the change in the amplitude of the signals was more sudden and intense, so much that it resulted in the complete shifting of the photopeak and not just in its broadening.

The other spectra show an intermediate situation, where the amplitude decrease produced a significant spread of the photopeak without generating additional peaks.

Detector 5 represents an exception since a sudden shutdown of the system caused the acquisition of only noise, and thus the formation of a new peak centered at the beginning of the spectrum.

Since each detector has been affected with different severity by this problem and since each photopeak has widened, the total spectrum reported in Figure 6.20 shows a much larger FWHM than that of the individual detectors.

The cause of these alterations in the amplitudes is given by the temperature of the apparatus and of the environment. It was noted in fact that this decrease was more relevant at the beginning of the acquisition when the apparatus hadn't reached yet its working temperature.

Moreover, since the laboratory where the testing was performed was not a temperature controlled environment, as the day went on and the temperature of the room increased, so did the change in value of the amplitudes. Cooling the apparatus with a fan and using air conditioning improved the stability of the system and eliminated almost completely the decrease.

Since the RAL laboratory is a temperature controlled environment, this problem should subside or at least become less relevant during the actual experiment.

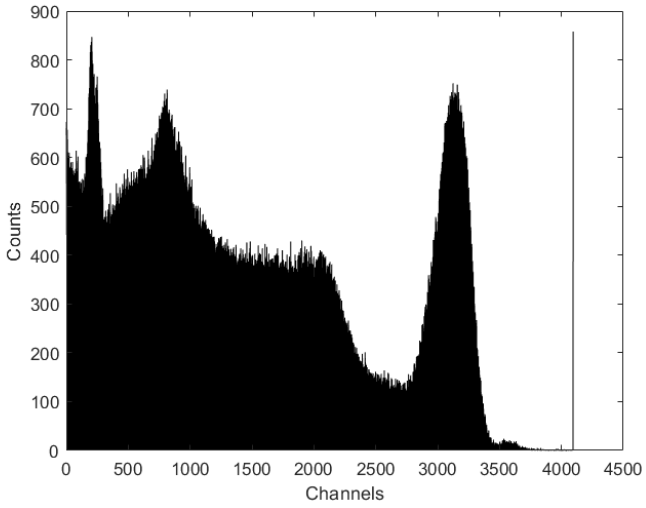

Figure 6.20: Sum of all spectra obtained during testing.

6.5 Present situation and future improvements

At present time the detector crown is almost complete. Of the seventeen $LaBr_3$ crystals originally planned for the crown, only the two crystals controlled by MC 1 and their electronics await implementation.

Due to a sudden anticipation in the FAMU experiment schedule, the crown was recently sent to the RAL laboratory, where it will remain until the completion of the experiment.

The missing detectors and electronics will be sent at a later date, together with the completed and upgraded GSPS digitizer.

Regarding the future improvement in the detector crown, currently a new front end circuit is under development in order to further improve the quality of the acquired signal. This new circuit will be built as to optimize the performance of the GSPS: it will shape the signal by improving its rising edge while also leaving its tail intact, so that the GSPS data processing will be faster and more accurate. Furthermore, a current mirror system will prevent the data acquisition system from reaching saturation.

Chapter 7

Conclusions

The incompatibility between the proton radius values measured in recent years has no explanation yet, and the aim of the FAMU experiment is to investigate the true nature of this discrepancy.

The proposal carried out by the experiment consists into obtaining a more accurate value of the Zemach radius of the proton: if the value will be compatible with those previously measured all over the world, then at the basis of the proton radius puzzle there are procedural errors or neglected but still relevant corrections. Otherwise, the new value will indicate the presence of a new phenomenon never studied before.

Whether the cause lies in neglected errors or in new and unknown physics, a high precision spectroscopy experimental apparatus is needed in order to solve the proton radius puzzle completely.

Furthermore, the new procedure on which the experiment is based requires also an in-depth knowledge of the temperature dependence of the muon transfer rate from hydrogen to oxygen. For this reason from 2014 until now multiple preliminar researches have been carried on in order to obtain a clearer understanding of this quantity.

In the meantime, the experimental apparatus has been assembled at the RIKEN-RAL laboratory, one of the few locations able to provide a pulsed muon beam capable of satisfying the strict requirements dictated by the FAMU experiment.

One of the main components required for the experiment, the detector crown, has been recently sent. This detector crown was devised and built by the Bologna Division of INFN and by the Physics Department of the University of Bologna and contains an array of innovative detectors. It is in fact composed by seventeen lanthanum bromide scintillator crystals with PMT and is coupled to a GSPS digitizer.

The crown has been calibrated and tested, and although there is still room for improvement regarding its dependence on temperature, it's possible to see that it works as intended. The detector array is currently missing two detectors that will be implemented in the coming months, together with the GSPS digitizer.

At present the RAL laboratory is on standby due to the regular maintenance required

to keep the muon beam functioning. Once this maintenance period ends, a final calibration and test of the entire apparatus will be performed. After the test, it will be the turn of the actual data acquisition, which is scheduled for early March. This new measure of the Zemach radius might once and for all solve the proton radius puzzle, and even lead the way towards yet unknown phenomena.

Chapter 8

Bibliography

[1] AD9434 ADC datasheet. URL: https://www.analog.com/en/products/ad9434.html#product-overview.

[2] Analogic optocoupler datasheet. URL: https://www.mouser.it/ProductDetail/Toshiba/TLP3906TPLE?qs=rsevcuukUAxu2A8ErKzvbw%3D%3D.

[3] Enclustra website. URL: https://www.enclustra.com/en/products/system-on-chip-modules/mercury-xu1.

[4] GLP series planar HPGe low-energy detector product configuration guide. URL: https://www.ortec-online.com/products/radiation-detectors/germanium-hpge-radiation-detectors/hpge-radiation-detector-types-how-choose/glp-series-planar-hpge-low-energy-radiation-detectors.

[5] GMX series GAMMA-X HPGe (high-purity germanium) coaxial photon detector system. URL: https://www.ortec-online.com/products/radiation-detectors/germanium-hpge-radiation-detectors/hpge-radiation-detector-types-how-choose/gmx-n-type-coaxial-hpge-radiation-detectors.

[6] HAMAMATSU R11265-200 PMT datasheet. URL: https://www.hamamatsu.com/us/en/product/optical-sensors/pmt/pmt_tube-alone/metal-package-type/R11265U-200.html.

[7] MAESTRO MCA emulator for microsoft windows xp professional sp3 and windows 7 x32 and x64. URL: https://www.ortec-online.com/products/application-software/maestro-mca.

[8] Profile "S" and "C" series detectors brochure. URL: https://www.ortec-online.com/products/radiation-detectors/germanium-hpge-radiation-detectors/hpge-radiation-detector-types-how-choose/profile-gem-p-type-coaxial-and-semi-planar-hpge-radiation-detectors.

[9] RIKEN-RAL muon group web page. URL: https://www.isis.stfc.ac.uk/Pages/RIKENRAL-Muon-Group.aspx.

[10] Science and technology facilites council web page. URL: https://www.ukri.org/councils/stfc/.

[11] Teensyduino 3.5 website. URL: https://www.pjrc.com/store/teensy35.html.

[12] A. Adamczak, G. Baccolo, S. Banfi, D. Bakalov, G. Baldazzi, R. Benocci, R. Bertoni, M. Bonesini, V. Bonvicini, and F. Chignoli et al. The FAMU experiment at RIKEN-RAL to study the muon transfer rate from hydrogen to other gases. *Journal of Instrumentation*, 13(12):P12033, dec 2018. URL: https://dx.doi.org/10.1088/1748-0221/13/12/P12033, doi:10.1088/1748-0221/13/12/P12033.

[13] A. Adamczak, M.P. Faifman, L.I. Ponomarev, V.I. Korobov, V.S. Melezhik, R.T. Siegel, and J. Woźniak. Atlas of cross sections for scattering of muonic hydrogen atoms on hydrogen isotope molecules. *Atomic Data and Nuclear Data Tables*, 62(2):255–344, 1996. URL: https://www.sciencedirect.com/science/article/pii/S0092640X96900066, doi:https://doi.org/10.1006/adnd.1996.0006.

[14] Andrzej Adamczak. Differential cross sections for muonic atom scattering from hydrogenic molecules. *Physical Review A*, 74(4), oct 2006. URL: https://doi.org/10.1103%2Fphysreva.74.042718, doi:10.1103/physreva.74.042718.

[15] Andrzej Adamczak, Dimitar Bakalov, Lyubomir Stoychev, and Andrea Vacchi. Hyperfine spectroscopy of muonic hydrogen and the PSI Lamb shift experiment. *Nuclear Instruments and Methods in Physics Research Section B: Beam Interactions with Materials and Atoms*, 281:72–76, 2012. URL: https://www.sciencedirect.com/science/article/pii/S0168583X12002091, doi:https://doi.org/10.1016/j.nimb.2012.04.001.

[16] Bakalov D. Bakalova-K. et al. Adamczak, A. On the use of a H2–O2 gas target in muonic hydrogen atom hyperfine splitting experiments. *Hyperfine Interactions*, 136:1–7, 2001. doi:https://doi.org/10.1023/A:1015576825454.

[17] M. S. Alekhin, J. T. M. de Haas, I. V. Khodyuk, K. W. Krämer, P. R. Menge, V. Ouspenski, and P. Dorenbos. Improvement of γ-ray energy resolution of $LaBr_3$:Ce^{3+} scintillation detectors by Sr^{2+} and Ca^{2+} co-doping. *Applied Physics Letters*, 102(16):161915, 2013. doi:10.1063/1.4803440.

[18] V. A. Andreev, T. I. Banks, R. M. Carey, T. A. Case, and S. M. Clayton et al. Measurement of the formation rate of muonic hydrogen molecules. *Physical Review C*, 91(5), may 2015. URL: https://doi.org/10.1103%2Fphysrevc.91.055502, doi:10.1103/physrevc.91.055502.

[19] Aldo Antognini. The Lamb shift experiment in muonic hydrogen, December 2005. URL: http://nbn-resolving.de/urn:nbn:de:bvb:19-50441.

[20] Aldo Antognini, Franz Kottmann, François Biraben, Paul Indelicato, François Nez, and Randolf Pohl. Theory of the 2S–2P Lamb shift and 2S hyperfine splitting in muonic hydrogen. *Annals of Physics*, 331:127–145, apr 2013.

[21] Aldo Antognini, François Nez, and Randolf Pohl et al. Proton structure from the measurement of 2S-2P transition frequencies of muonic hydrogen. *Science*, 339(6118):417–420, 2013. URL: https://www.science.org/doi/abs/10.1126/science.1230016, arXiv:https://www.science.org/doi/pdf/10.1126/science.1230016, doi:10.1126/science.1230016.

[22] Bruno Lepetit Carlo Rizzo Dimitar Bakalov Arnaud Dupays, Alberto Beswick. Proton zemach radius from measurements of the hyperfine splitting of hydrogen and muonic hydrogen. *Physical Review A*, 68(5), nov 2003. URL: https://doi.org/10.1103%2Fphysreva.68.052503, doi:10.1103/physreva.68.052503.

[23] John Arrington and Ingo Sick. Evaluation of the proton charge radius from electron–proton scattering. *Journal of Physical and Chemical Reference Data*, 44(3):031204, 2015. URL: https://doi.org/10.1063/1.4921430, arXiv:https://doi.org/10.1063/1.4921430, doi:https://doi.org/10.1063/1.4921430.

[24] D. Bakalov, E. Milotti, C. Rizzo, A. Vacchi, and E. Zavattini. Experimental method to measure the hyperfine splitting of muomic hydrogen (μp)1s. *Physics Letters A*, 172(4):277–280, 1993. URL: https://www.sciencedirect.com/science/article/pii/037596019391021V, doi:https://doi.org/10.1016/0375-9601(93)91021-V.

[25] Dimitar Bakalov, Andrzej Adamczak, Mihail Stoilov, and Andrea Vacchi. Theoretical and computational study of the energy dependence of the muon transfer rate from hydrogen to higher-Z gases. *Physics Letters A*, 379(3):151–156, 2015. URL: https://www.sciencedirect.com/science/article/pii/S0375960114011530, doi:https://doi.org/10.1016/j.physleta.2014.11.025.

[26] Bakalov, Dimitar and Stoilov, Mihail. Toward the measurement of the hyperfine structure of muonic hydrogen in the FAMU experiment: Multi-pass cavity optimization for experiments with pulsed sources. *EPJ Web of Conferences*, 181:01033, 2018. doi:10.1051/epjconf/201818101033.

[27] Giuseppe Baldazzi, Ignazio D'Antone, Stefano Meneghini, Luigi Rignanese, Riccardo Travaglini, Carlo Veri, and Mirco Zuffa. GSPS v2 board: design, implementation and firmware description. 2019.

[28] J. C. Bernauer, P. Achenbach, C. Ayerbe Gayoso, R. Böhm, and D. et al. Bosnar. High-precision determination of the electric and magnetic form factors of the proton. *Phys. Rev. Lett.*, 105:242001, Dec 2010. URL: https://link.aps.org/doi/10.1103/PhysRevLett.105.242001, doi:10.1103/PhysRevLett.105.242001.

[29] Jan C Bernauer. Measurement of the elastic electron-proton cross section and separation of the electric and magnetic form factor in the Q^2 range from 0.004 to 1 $(GeV/c)^2$. *Physical review*, 70, 2010. doi:https://doi.org/10.1103/PhysRevC.70.015206.

[30] G. Bizarri and P. Dorenbos. Charge carrier and exciton dynamics in $LaBr_3$:Ce^{3+} scintillators: Experiment and model. *Phys. Rev. B*, 75:184302, May 2007. URL: https://link.aps.org/doi/10.1103/PhysRevB.75.184302, doi:10.1103/PhysRevB.75.184302.

[31] S Boffi, C Giusti, and FD Pacati. Structure functions in nucleon emission by polarized electrons. *Nuclear Physics A*, 435(3-4):697–707, 1985. doi:https://doi.org/10.1016/0375-9474(85)90182-4.

[32] M. Bonesini. The FAMU experiment at RIKEN RAL for a precise measure of the proton radius. 2020. URL: https://arxiv.org/abs/2010.01398, doi:https://doi.org/10.48550/arxiv.2010.01398.

[33] M. Bonesini, R. Benocci, R. Bertoni, R. Mazza, A. deBari, A. Menegolli, M.C. Prata, M. Rossella, L. Tortora, E. Mocchiutti, A. Vacchi, and E. Vallazza. The upgraded beam monitor system of the FAMU experiment at RIKEN–RAL. *Nuclear Instruments and Methods in Physics Research Section A: Accelerators, Spectrometers, Detectors and Associated Equipment*, 936:592–594, 2019. Frontier Detectors for Frontier Physics: 14th Pisa Meeting on Advanced Detectors. URL: https://www.sciencedirect.com/science/article/pii/S0168900218310507, doi:https://doi.org/10.1016/j.nima.2018.08.092.

[34] M. Bonesini, R. Bertoni, F. Chignoli, R. Mazza, T. Cervi, A. de Bari, and A. Menegolli et al. The construction of the Fiber-SiPM beam monitor system of the R484 and R582 experiments at the RIKEN-RAL muon facility. *Journal of Instrumentation*, 12(03):C03035, mar 2017. URL: https://dx.doi.org/10.1088/1748-0221/12/03/C03035, doi:10.1088/1748-0221/12/03/C03035.

[35] Maurizio Bonesini, R. Bertoni, T. Cervi, M. Clemenza, A de Bari, R. Mazza, A. Menegolli, M. C Prata, and M. Rossella. Systematic study of innovative hygroscopic and non-hygroscopic crystals with SiPM array readout. *PoS*, EPS-HEP2017:777, 2017. doi:10.22323/1.314.0777.

[36] P. Branchini, A. Budano, A. Balla, M. Beretta, P. Ciambrone, and E. De Lucia. An FGPA based general purpose DAQ module for the KLOE-2 experiment. *IEEE Transactions on Nuclear Science*, 58(4):1544–1546, 2011. doi:10.1109/TNS.2011.2158609.

[37] K L Brown and S K Howry. TRANSPORT/360: A computer program for designing charged particle beam transport systems. jan 1970.

[38] K. L. Brown and F. C. Iselin. Decay TURTLE (trace unlimited rays through lumped elements): A computer program for simulating charged particle beam transport systems, including decay calculations. feb 1974. doi:10.5170/CERN-1974-002.

[39] R. Carbone, M. Bonesini, R. Bertoni, R. Mazza, M. Rossella, L. Tortora, A. Vacchi, E. Vallazza, and G. Zampa. The fiber-SiPMT beam monitor of the R484 experiment at the RIKEN-RAL muon facility. *Journal of Instrumentation*, 10(03):C03007, mar 2015. URL: https://dx.doi.org/10.1088/1748-0221/10/03/C03007, doi:10.1088/1748-0221/10/03/C03007.

[40] Hao Cheng, Bao-Hua Sun, Li-Hua Zhu, Tian-Xiao Li, Guang-Shuai Li, Cong-Bo Li, Xiao-Guang Wu, and Yun Zheng. Intrinsic background radiation of LaBr3(ce) detector via coincidence measurements and simulations. *Nuclear Science and Techniques*.

[41] Cesare Chiccoli, Y Melezhik, Paolo Pasini, L Ponomarey, Wozniakd, and Vladimir Korobov. The atlas of the cross-sections of mesic atomic processes. part iii: The processes $p\mu + (d, t)$, $d\mu + (p, t)$, $t\mu + (p, d)$. *Muon Catalized Fusion*, 7:87–153, 08 1992.

[42] T de Forest Jr and John Dirk Walecka. Electron scattering and nuclear structure. *Advances in Physics*, 15(57):1–109, 1966. doi:https://doi.org/10.1146/annurev.ns.37.120187.001025.

[43] Rosie de Laune and Sara Fletcher et al. ISIS neutron and muon source: Annual review 2022. 2022. URL: https://www.isis.stfc.ac.uk/Pages/ISIS-2022-Annual-Review-Out-Now.aspx.

[44] D Drechsel and MM Giannini. Electron scattering off nuclei. *Reports on Progress in Physics*, 52(9):1083–1164, 1989. doi:https://doi.org/10.1088/0034-4885/52/9/002.

[45] Arnaud Dupays, Bruno Lepetit, J. Alberto Beswick, Carlo Rizzo, and Dimitar Bakalov. Nonzero total-angular-momentum three-body dynamics using hyperspherical elliptic coordinates: Application to muon transfer from muonic hydrogen to atomic oxygen and neon. *Phys. Rev. A*, 69:062501, Jun 2004. URL: https://link.aps.org/doi/10.1103/PhysRevA.69.062501, doi:10.1103/PhysRevA.69.062501.

[46] G.H. Eaton, A. Carne, S.F.J. Cox, J.D. Davies, R. de Renzi, O. Hartmann, A. Kratzer, C. Ristori, C.A. Scott, G.C. Stirling, and T. Sundqvist. Commissioning of the rutherford appleton laboratory pulsed muon facility. *Nuclear Instruments and Methods in Physics Research Section A: Accelerators, Spectrometers, Detectors and Associated Equipment*, 269(3):483–491, 1988. URL: https://www.sciencedirect.com/science/article/pii/0168900288901246, doi:https://doi.org/10.1016/0168-9002(88)90124-6.

[47] M.I. Eides et al. Theory of light hydrogenlike atoms. *Physics Reports*, 342(2):63–261, 2001. URL: https://www.sciencedirect.com/science/article/pii/S0370157300000776, doi:https://doi.org/10.1016/S0370-1573(00)00077-6.

[48] DL Fancher, DO Caldwell, John P Cumalat, AM Eisner, TP McPharlin, RJ Morrison, FV Murphy, and SJ Yellin. Precision comparison of inelastic electron and positron scattering from hydrogen. *Physical Review Letters*, 37(20):1323–1326, 1976. doi:https://doi.org/10.1103/PhysRevLett.37.1323.

[49] D. J. S. Findlay. ISIS - pulsed neutron and muon source. In *2007 IEEE Particle Accelerator Conference (PAC)*, pages 695–699, 2007. doi:10.1109/PAC.2007.4441104.

[50] C. Fiorini, A. Gola, M. Zanchi, A. Longoni, P. Lechner, H. Soltau, and L. Struder. Gamma-ray spectroscopy with $LaBr_3$:Ce scintillator readout by a silicon drift detector. In *IEEE Nuclear Science Symposium Conference Record, 2005*, volume 1, pages 230–234, 2005. doi:10.1109/NSSMIC.2005.1596243.

[51] David J Griffiths. *Introduction to quantum mechanics*. 1994.

[52] Daniele Guffanti. The FAMU experiment: measurement of muonic atoms spectra. URL: https://web.infn.it/FAMU/wp-content/uploads/2019/09/9842-Guffanti-magistrale.pdf.

[53] K. Ishida, K. Nagamine, T. Matsuzaki, I. Watanabe, and G.H. Eaton. RIKEN accelerator progress report. 28:175, 1995.

[54] R. Jacot-Guillarmod, F. Mulhauser, C. Piller, L. A. Schaller, L. Schellenberg, H. Schneuwly, Y.-A. Thalmann, S. Tresch, A. Werthmüller, and A. Adamczak. Muon transfer from thermalized muonic hydrogen isotopes to argon. *Phys. Rev. A*, 55:3447–3452, May 1997. URL: https://link.aps.org/doi/10.1103/PhysRevA.55.3447, doi:10.1103/PhysRevA.55.3447.

[55] R. Jacot-Guillarmod, F. Mulhauser, C. Piller, and H. Schneuwly. Charge transfer from muonic hydrogen to neon. *Phys. Rev. Lett.*, 65:709–712, Aug 1990. URL: https://link.aps.org/doi/10.1103/PhysRevLett.65.709, doi:10.1103/PhysRevLett.65.709.

[56] Ivan V. Khodyuk, Mikhail S. Alekhin, Johan T.M. de Haas, and Pieter Dorenbos. Improved scintillation proportionality and energy resolution of $LaBr_3$:Ce at 80k. *Nuclear Instruments and Methods in Physics Research Section A: Accelerators, Spectrometers, Detectors and Associated Equipment*, 642(1):75–77, 2011. URL: https://www.sciencedirect.com/science/article/pii/S0168900211007145, doi:https://doi.org/10.1016/j.nima.2011.04.006.

[57] Ivan V Khodyuk and Pieter Dorenbos. Nonproportional response of $LaBr_3$:Ce and $LaCl_3$:Ce scintillators to synchrotron x-ray irradiation. *Journal of Physics: Condensed Matter*, 22(48):485402, nov 2010. URL: https://dx.doi.org/10.1088/0953-8984/22/48/485402, doi:10.1088/0953-8984/22/48/485402.

[58] Glenn F. Knoll. *Radiation detection and measurement*. John Wiley and Sons, 2000.

[59] Ludhova L. The muonic hydrogen Lamb shift experiment: Lifetime and population of the μp(2S) state, 2005. URL: https://folia.unifr.ch/unifr/documents/300097.

[60] Willis E. Lamb and Robert C. Retherford. Fine structure of the hydrogen atom by a microwave method. *Phys. Rev.*, 72:241–243, Aug 1947. URL: https://link.aps.org/doi/10.1103/PhysRev.72.241, doi:10.1103/PhysRev.72.241.

[61] Anh-Thu Le and C. D. Lin. Muon transfer from muonic hydrogen to atomic oxygen and nitrogen. *Phys. Rev. A*, 71:022507, Feb 2005. URL: https://link.aps.org/doi/10.1103/PhysRevA.71.022507, doi:10.1103/PhysRevA.71.022507.

[62] L. Ludhova, F.D. Amaro, A. Antognini, and F. Biraben et al. Planar LAAPDs: temperature dependence, performance, and application in low-energy x-ray spectroscopy. *Nuclear Instruments and Methods in Physics Research Section A: Accelerators, Spectrometers, Detectors and Associated Equipment*, 540(1):169–179, 2005. URL: https://www.sciencedirect.com/science/article/pii/S0168900204024143, doi:https://doi.org/10.1016/j.nima.2004.11.017.

[63] T. Matsuzaki, K. Ishida, K. Nagamine, I. Watanabe, G.H. Eaton, and W.G. Williams. The RIKEN-RAL pulsed muon facility. *Nuclear Instruments and Methods in Physics Research Section A: Accelerators, Spectrometers, Detectors and Associated Equipment*, 465(2):365–383, 2001. URL: https://www.sciencedirect.com/science/article/pii/S0168900201006945, doi:https://doi.org/10.1016/S0168-9002(01)00694-5.

[64] B.D. Milbrath, B.J. Choate, J.E. Fast, R.T. Kouzes, and J.E. Schweppe. Comparison of $LaBr_3$:Ce and NaI(Tl) scintillators for radio-isotope identification devices. In *IEEE Nuclear Science Symposium Conference Record, 2005*, volume 1, pages 283–287, 2005. doi:10.1109/NSSMIC.2005.1596254.

[65] E. Mocchiutti, A. Adamczak, D. Bakalov, G. Baldazzi, and R. Benocci et al. First measurement of the temperature dependence of muon transfer rate from muonic hydrogen atoms to oxygen. *Physics Letters A*, 384(26):126667, 2020. URL: https://www.sciencedirect.com/science/article/pii/S037596012030534X, doi:https://doi.org/10.1016/j.physleta.2020.126667.

[66] E Mocchiutti, V Bonvicini, M Danailov, E Furlanetto, K S Gadedjisso-Tossou, D Guffaanti, and C Pizzolotto et al. FAMU: study of the energy dependent transfer rate $\lambda_{\mu p \to \mu o}$. *Journal of Physics: Conference Series*, 1138:012017, nov 2018. doi:10.1088/1742-6596/1138/1/012017.

[67] Peter J. Mohr, David B. Newell, and Barry N. Taylor. CODATA recommended values of the fundamental physical constants: 2014. *Rev. Mod. Phys.*, 88:035009, Sep 2016. URL: https://link.aps.org/doi/10.1103/RevModPhys.88.035009, doi:10.1103/RevModPhys.88.035009.

[68] Peter J. Mohr, Barry N. Taylor, and David B. Newell. CODATA recommended values of the fundamental physical constants: 2006. *Rev. Mod. Phys.*, 80:633–730, Jun 2008. URL: https://link.aps.org/doi/10.1103/RevModPhys.80.633, doi:10.1103/RevModPhys.80.633.

[69] Peter J Mohr, Barry N Taylor, David B Newell, et al. CODATA recommended values of the fundamental physical constants: 2010. *Reviews of Modern Physics*, 84:1527–1605, 2012. doi:https://doi.org/10.1103/RevModPhys.84.1527.

[70] Schneuwly H. Mulhauser, F. Systematic study of muon transfer to sulphur dioxide. *Hyperfine Interactions*, 82:507–512, 1993. doi:https://doi.org/10.1007/BF01027985.

[71] K. Nagamine, T. Matsuzaki, and K. et al. Ishida. Construction of riken-ral muon facility at ISIS and advanced *mu*SR. *Hyperfine Interact.*, 87:1091–1098. URL: https://doi-org.ezproxy.unibo.it/10.1007/BF02068509.

[72] Adamczak A. Bakalov D. et al. Pizzolotto, C. The FAMU experiment: muonic hydrogen high precision spectroscopy studies. *Eur. Phys. J. A*, 56.

[73] C. Pizzolotto, A. Sbrizzi, A. Adamczak, and D. Bakalov et al. Measurement of the muon transfer rate from muonic hydrogen to oxygen in the range 70-336 k. *Physics Letters A*, 403:127401, 2021. URL: https://www.sciencedirect.com/science/article/pii/S0375960121002656, doi:https://doi.org/10.1016/j.physleta.2021.127401.

[74] R. Pleskac, Z. Abou-Haidar, C. Agodi, M.A.G. Alvarez, T. Aumann, and G. Battistoni et al. The FIRST experiment at GSI. *Nuclear Instruments and Methods in Physics Research Section A: Accelerators, Spectrometers, Detectors and Associated*

Equipment, 678:130–138, 2012. URL: https://www.sciencedirect.com/science/article/pii/S0168900212001830, doi:https://doi.org/10.1016/j.nima.2012.02.020.

[75] Randolf Pohl, Aldo Antognini, François Nez, Fernando D Amaro, François Biraben, Joao MR Cardoso, Daniel S Covita, Andreas Dax, Satish Dhawan, Luis MP Fernandes, et al. The size of the proton. *Nature*, 466(7303):213–216, 2010. doi:https://doi.org/10.1038/nature09250.

[76] Luigi Pio Rignanese. *The FAMU experiment: Towards the measurement of the hyperfine splitting of the muonic hydrogen*. PhD thesis, alma, 2019. URL: http://amsdottorato.unibo.it/8895/.

[77] LS Rochester, WB Atwood, ED Bloom, RLA Cottrell, DH Coward, H DeStaebler, M Mestayer, CY Prescott, S Stein, Richard E Taylor, et al. Comparison of the yields of inelastic electron and positron scattering from hydrogen and deuterium at 15 $(GeV/c)^2$. *Physical Review Letters*, 36(22):1284–1287, 1976. doi:https://doi.org/10.1103/PhysRevLett.36.1284.

[78] Saint-Gobain. Saint-gobain plastic scintillating fiber datasheet. URL: https://www.crystals.saint-gobain.com/radiation-detection-scintillators/fibers.

[79] L.G. Shapiro and G.C. Stockman. *Computer vision*. Prentice Hall, 2001.

[80] L I Stoychev, H Cabrera, K S Gadedjisso-Tossou, I P Nikolov, P Sigalotti, A A Demidovich, J J Suárez-Vargas, E Mocchiutti, J Niemela, M Baruzzo, N Vasiliev, Y Zaporozhchenko, M B Danailov, and Andrea Vacchi. Pulse amplification in a cr4+:forsterite single longitudinal mode (SLM) multi-pass amplifier. *Laser Physics*, 29(6):065801, apr 2019. URL: https://dx.doi.org/10.1088/1555-6611/ab17cf, doi:10.1088/1555-6611/ab17cf.

[81] T. Suzuki, D. F. Measday, and J. P. Roalsvig. Total nuclear capture rates for negative muons. *Phys. Rev. C*, 35:2212–2224, Jun 1987. URL: https://link.aps.org/doi/10.1103/PhysRevC.35.2212, doi:10.1103/PhysRevC.35.2212.

[82] Eite Tiesinga, Peter J. Mohr, David B. Newell, and Barry N. Taylor. CODATA recommended values of the fundamental physical constants: 2018. *Rev. Mod. Phys.*, 93:025010, Jun 2021. URL: https://link.aps.org/doi/10.1103/RevModPhys.93.025010, doi:10.1103/RevModPhys.93.025010.

[83] Riccardo Travaglini, Giuseppe Baldazzi, Ignazio D'Antone, Stefano Meneghini, Luigi Pio Rignanese, and Mirco Zuffa. A 1 GS/s sampling digitizer designed with interleaved architecture (GSPS) for the LaBr3 detectors of the FAMU experiment. *PoS*, TWEPP2018:022, 2019. doi:10.22323/1.343.0022.

[84] E. V. D. van Loef, P. Dorenbos, C. W. E. van Eijk, K. Krämer, and H. U. Güdel. High-energy-resolution scintillator: Ce^{3+} activated $LaBr_3$. *Applied Physics Letters*, 79(10):1573–1575, 2001. doi:10.1063/1.1385342.

[85] Jan Vogelsang, Marc Diepold, Aldo Antognini, Andreas Dax, Johannes Götzfried, Theodor W. Hänsch, Franz Kottmann, Julian J. Krauth, Yi-Wei Liu, Tobias Nebel, Francois Nez, Karsten Schuhmann, David Taqqu, and Randolf Pohl. Multipass laser cavity for efficient transverse illumination of an elongated volume. *Opt. Express*, 22(11):13050–13062, Jun 2014. URL: https://opg.optica.org/oe/abstract.cfm?URI=oe-22-11-13050, doi:10.1364/OE.22.013050.

[86] Shabaev V. Plunien G. et al. Volotka, A. Zemach and magnetic radius of the proton from the hyperfine splitting in hydrogen. *Eur. Phys. J. D*, 33:23–27, 2005. doi:https://doi.org/10.1140/epjd/e2005-00025-9.

[87] Chen K W. *High energy physics : proceedings of the EPS international conference, Palermo (Italy), 23-28 June, 1975 / Antonino Zichichi editor*. Editrice compositori, Bologna, 1976.

[88] Adamczak A. Jacot-Guillarmod R. et al. Werthmüller, A. Transfer of negative muons from hydrogen to oxygen. *Hyperfine Interactions*, 103:147–155, 1996. doi:https://doi.org/10.1007/BF02317350.

[89] Adamczak A. Jacot-Guillarmod-R. et al. Werthmüller, A. Energy dependence of the charge exchange reaction from muonic hydrogen to oxygen. *Hyperfine Interactions*, 116:1–16, 1998. doi:https://doi.org/10.1023/A:1012618721239.